

# Conditional Extremes with Graphical Models

Aiden Farrell<sup>1,\*</sup>, Emma F. Eastoe<sup>1,†</sup>, and Clement Lee<sup>2,‡</sup>

<sup>1</sup>*School of Mathematical Sciences, Fylde College, Lancaster University, UK*

<sup>2</sup>*School of Mathematics, Statistics and Physics, Herschel Building,  
Newcastle University, UK*

## Abstract

Multivariate extreme value analysis quantifies the probability and magnitude of joint extreme events. River discharges from the upper Danube River basin provide a challenging dataset for such analysis because the data, which is measured on a spatial network, exhibits both asymptotic dependence and asymptotic independence. To account for both features, we extend the conditional multivariate extreme value model (CMEVM) with a new approach for the residual distribution. This allows sparse (graphical) dependence structures and fully parametric prediction. Our approach fills a current gap in statistical methodology by extending graphical extremes models to asymptotically independent random variables. Further, the model can be used to learn the graphical dependence structure when it is unknown *a priori*. To support inference in high dimensions, we propose a stepwise inference procedure that is computationally efficient and loses no information or predictive power. We show our method is flexible and accurately captures the extremal dependence for the upper Danube River basin discharges.

Keywords: Extremal dependence, graphical extremes, conditional multivariate extremes, sparsity, river networks

## 1 Introduction

The development of statistical models to describe and predict multivariate extreme events is a crucial part of natural hazard risk assessment, especially for data arising from spatial,

---

\*a.farrell1@lancaster.ac.uk

†e.eastoe@lancaster.ac.uk

‡clement.lee@newcastle.ac.uk

temporal, and spatio-temporal processes. For example, multivariate extreme value models have been adopted to predict risk from extreme snowfall (Blanchet and Davison, 2011), sea surface temperature (Simpson and Wadsworth, 2021), droughts (Oesting and Stein, 2018), river flows (Asadi et al., 2015; Keef et al., 2013), forest fires (Stephenson et al., 2015), precipitation (Westra and Sisson, 2011), wind-speed (Engelke et al., 2015), and ocean storms (Shooter et al., 2019), all of which exhibit complex behaviour, which can only be effectively captured by a flexible, multi-parameter model.

Central to multivariate extreme value modelling is the concept of extremal dependence. Let  $V = \{1, \dots, d\}$  and consider the  $d$ -dimensional random vector  $X = \{X_j : j \in V\}$  with joint and marginal distributions  $F_X(x) = \mathbb{P}[X \leq x]$  and  $F_j(x_j) = \mathbb{P}[X_j \leq x_j]$ , respectively. If the measure  $\chi_A := \lim_{u \rightarrow 1} \mathbb{P}[F_i(X_i) > u : i \in A] / (1 - u)$  for  $A \subseteq V$  and  $|A| \geq 2$  is strictly positive then the components in  $A$  experience their extremes simultaneously and are said to belong to the extremal dependence class of asymptotic dependence (AD) (Simpson et al., 2020). If  $\chi_A = 0$ , then the variables in  $A$  cannot be simultaneously extreme. Furthermore, if  $\chi_A = 0$  and  $|A| = 2$ , then the two variables belong to the extremal dependence class of asymptotic independence (AI) (Ledford and Tawn, 1996). Full AD occurs when  $\chi_A > 0$  for all subsets  $A \subseteq V$ , and full AI occurs when  $\chi_A = 0$  for all two-dimensional subsets of  $V$ . While independence implies AI, the converse is not true.

The strength of association between components with AI can be quantified using the coefficient of tail dependence  $\eta$  (Ledford and Tawn, 1996). The coefficient arises by approximating the joint survivor function of  $(X_i, X_j)$ . Specifically, for  $i, j \in A$ ,  $i \neq j$ , and large  $x$ ,

$$\mathbb{P}[F_F^{-1}(F_{X_i}(X_i)) > x, F_F^{-1}(F_{X_j}(X_j)) > x] \sim \mathcal{L}(x) \mathbb{P}[F_F^{-1}(F_{X_i}(X_i)) > x]^{-\frac{1}{\eta}} \quad (1.1)$$

where  $F_F^{-1}(\cdot)$  is the quantile function of the standard Fréchet distribution and  $\mathcal{L}(\cdot)$  is a slowly varying function. The association between  $X_i$  and  $X_j$  can be classed as exact independence ( $\eta = 0.5$ ) or negatively ( $0 < \eta < 0.5$ ) or positively ( $0.5 < \eta < 1$ ) associated. For pairs that exhibit AD,  $\eta = 1$  and  $\mathcal{L}(x) \rightarrow 0$  as  $x \rightarrow \infty$ . In practice, estimates of  $\eta$  are obtained over a range of finite thresholds and the limit behaviour of  $\eta(u)$ , where  $x$  in equation (1.1) corresponds to the  $u$ -th quantile of the standard Fréchet distribution, is used to determine the likely limit  $\eta$ .

We illustrate these concepts using river discharges from the upper Danube River basin. Daily discharge data at  $d = 31$  gauging stations for 1960-2009 is available from the Bavarian Environmental Agency (<http://www.gkd.bayern.de>). Figure 1 (left panel) shows the undirected tree implied by the flow connections of the river basin. We use the summer-

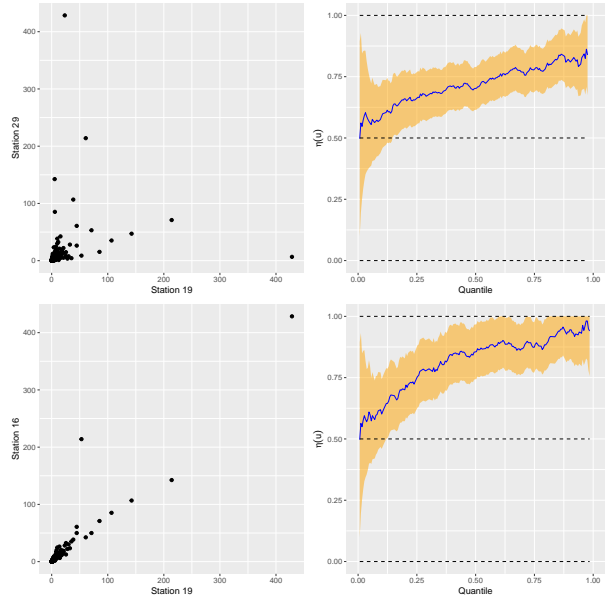
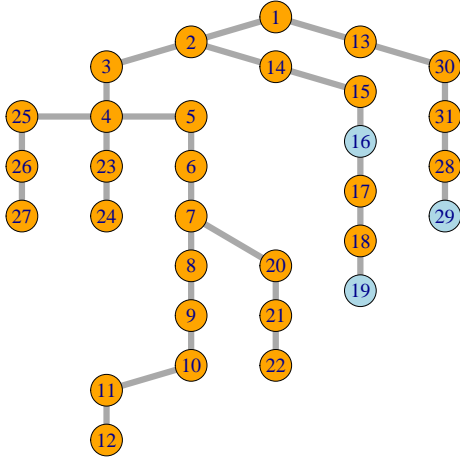


Figure 1: Undirected tree induced by the flow connections of the upper Danube River basin (left) with sites 16, 19 and 29 in blue. Scatter plots on standard Fréchet margins (centre) and empirical estimates of  $\eta(u)$  (right) for  $u \in (0, 1]$  for sites 19 and 29 (top) and 16 and 29 (right).

only, temporally declustered dataset (see Asadi et al. (2015) for details), available from the `graphicalExtremes` package (Engelke et al., 2024b) in R (R Core Team, 2024). The data have previously been analysed using a max-stable Brown Resnick process (Asadi et al., 2015) and a multivariate Pareto graphical model (Engelke and Hitz, 2020), both of which assume full AD. Figure 1 (right panel) shows scatter plots on standard Fréchet margins, and empirical estimates for the extremal dependence measure  $\eta(u)$  (Ledford and Tawn, 1996) for stations 19 and 29 (top), and 19 and 16 (bottom). Sites 19 and 29 lie on different tributaries and are flow-unconnected, while 19 and 16 both lie on the Isar tributary and are flow-connected. Stations 19 and 16 appear to exhibit AD: they experience extreme events simultaneously and  $\eta(u) \rightarrow 1$  as  $u \rightarrow 1$ . Conversely, the scatter plots for stations 19 and 29 suggest AI, which is supported by the fact that  $\eta(u) \not\rightarrow 1$  as  $u \rightarrow 1$ . Thus, while flow-connected stations often exhibit AD, some flow-unconnected stations do not and assuming AD for such stations would lead to overestimation of their joint tail behaviour.

There are many multivariate extreme value models for datasets with full AD. These are based on max-stable distributions and processes, including the multivariate Pareto distribution (Rootzén and Tajvidi, 2006; Rootzén et al., 2018), and the max-stable (Smith, 1990) and generalised  $r$ -Pareto (Ferreira and de Haan, 2014) processes. The process formulations form the basis of spatial (de Fondeville and Davison, 2018; Reich and Shaby, 2012; Ribatet, 2013),

temporal (Schlather, 2002; Smith et al., 1997), and spatio-temporal (Davis et al., 2013; Huser and Davison, 2014; Opitz et al., 2018) models for extremes, and the multivariate Pareto distribution forms the basis for the existing graphical modelling approach for extremes (Engelke et al., 2024a). Such models appeal due to their links to asymptotic limit theory; however, they are unsuitable for the many instances in which datasets shows AI.

Models for AI, such as the one proposed by Ledford and Tawn (1997), were initially limited to the bivariate case only. While Ramos and Ledford (2011) and Wadsworth and Tawn (2013) developed extensions of this model that allowed for inference away from the diagonal, the semi-parametric conditional multivariate extreme value model (CMEVM) was the first model to provide a credible approach to data exhibiting both AI and AD (Heffernan and Tawn, 2004). The CMEVM is not based on a multivariate distribution or process; rather, conditional on one variable being large, normalising functions are defined to control the rate of growth of all other variables such that, after normalisation, the joint distribution of these “residuals” is non-degenerate. The model has gained popularity due to the relative ease with which its parameters can be estimated and interpreted, even in high dimensions. Applications include flood risk mapping (Neal et al., 2013; Towe et al., 2019), and the prediction of extreme sea states (Gouldby et al., 2014, 2017; Ross et al., 2020), sea surface temperatures (Simpson and Wadsworth, 2021), heatwaves (Winter and Tawn, 2016), and precipitation (Debushe and Diriba, 2021; Richards et al., 2022).

As we will see in the next section, the predictive performance of the CMEVM declines with increasing dimensionality. The recent spatial CMEVM (Richards et al., 2022; Shooter et al., 2021; Wadsworth and Tawn, 2022) overcomes this by using a fully parametric spatial kernel for the residual distribution. By construction, this spatial model is appropriate for measurements on a continuous spatial surface but not for measurements on alternative topographies, such as road or river networks, which are represented by a graphical structure, such as that in Figure 1 (left panel). Meanwhile, Casey and Papastathopoulos (2023) have developed a theoretical framework for the CMEVM for processes observed on a chordal graph with singleton separator sets, but they have not developed this into a statistical model.

Our contribution fills these gaps. We present the multivariate asymmetric generalised Gaussian (MVAGG) to model the CMEVM residuals, to enable more accurate fully parametric prediction. Our model can also incorporate structure into the CMEVM residuals, thereby providing a framework for graphical structures that accommodates both extremal dependence classes. Our model generalises the temporal Markov model for extremes of Winter and Tawn (2017), but to the best of our knowledge, is the first model to incorporate a general graphical structure in the CMEVM. Finally, inference in high dimensions is achieved using stepwise

optimisation procedures that are computationally efficient, without any loss of information or predictive performance.

The remainder of this paper is structured as follows. Section 2 provides an overview of the CMEVM, introduces the MVAGG distribution, and describes the proposed structured CMEVM. Model inference, graphical selection, and model-based predictions are provided in Section 3. In Section 4, we illustrate the performance of our model and the graphical selection procedure, as well as the utility of the stepwise inference procedures. We then apply our model to river discharges in the upper Danube River basin (Asadi et al., 2015) in Section 5, and compare our model to the one proposed by Engelke and Hitz (2020). Finally, we outline directions for future research in Section 6.

## 2 Methodology

We review the CMEVM and introduce the MVAGG distribution before describing a new variant of the CMEVM that incorporates sparsity in the residual distribution. Throughout, we use the definitions  $V_{|i} := V \setminus \{i\}$  and  $X_{|i} := \{X_j : j \in V_{|i}\}$  to refer to the set  $V$  and vector  $X$  excluding their  $i$ th elements.

### 2.1 Conditional Multivariate Extreme Value Model

Multivariate extreme value models are typically defined on either max-stable or heavy-tailed univariate margins. While the original definition of the CMEVM was on standard Gumbel margins, Keef et al. (2013) popularised the use of standard Laplace margins due to the simplification that this brings to the parametrisation of the dependence structure. Use of specific margins is not restrictive since Sklar’s Theorem Sklar (1959) can be used to transform the univariate margins of a random vector without altering the dependence structure. In what follows,  $Y$  and  $Y_{|i}$  denote the random vectors  $X$  and  $X_{|i}$  following transformation to Laplace margins. The central assumption of the CMEVM is that there exist normalising functions  $\{a_{j|i} : \mathbb{R} \rightarrow \mathbb{R}, j \in V_{|i}\}$  and  $\{b_{j|i} : \mathbb{R} \rightarrow \mathbb{R}_+, j \in V_{|i}\}$ , such that for any  $i \in V$ ,

$$\left( \left\{ \frac{Y_j - a_{j|i}(Y_i)}{b_{j|i}(Y_i)} \right\}_{j \in V_{|i}}, Y_i - u_{Y_i} \right) \Big| Y_i > u_{Y_i} \xrightarrow{d} (\{Z_{j|i} : j \in V_{|i}\}, E), \quad (2.1)$$

with convergence as  $u_{Y_i} \rightarrow \infty$ . In the limit, the residual vector  $Z_{|i} = \{Z_{j|i} : j \in V_{|i}\}$  is independent of the conditioning component  $Y_i$  and has a non-degenerate distribution, while the limit variable  $E$  follows a standard exponential distribution Heffernan and Resnick

(2007). Consequently, inference can be undertaken separately on: (i)  $Y_i \mid Y_i > u_{Y_i}$ ; (ii) the normalising functions; and (iii) the residuals  $Z_{|i}$ . The first is trivial, since the tail of  $Y_i \mid Y_i > u_{Y_i}$  is standard exponential by limit (2.1). Parts (ii) and (iii) require greater consideration.

For (ii) the normalising functions, Heffernan and Tawn (2004) propose the form

$$a_{j|i}(y_i) = \alpha_{j|i}y_i, \quad b_{j|i}(y_i) = y_i^{\beta_{j|i}}$$

where, for Laplace margins,  $\alpha_{j|i} \in [-1, 1]$  and  $\beta_{j|i} \in (-\infty, 1]$ . These flexible functions capture AD ( $\alpha_{j|i} = 1$  and  $\beta_{j|i} = 0$ ), complete independence ( $\alpha_{j|i} = 0$ ), and AI (all other parameter combinations). While a class of models can be proposed for the normalising functions, there is no general class of distributions with which to model (iii) the residuals  $Z_{|i}$ . Heffernan and Tawn (2004) use the working assumption that  $Z_{|i}$  follows a  $(d-1)$ -dimensional multivariate Gaussian (MVG) distribution, denoted  $Z_{|i} \sim \text{MVG}_{d-1}(\boldsymbol{\mu}_{|i}, \Sigma_{|i}^*)$ , with mean vector  $\boldsymbol{\mu}_{|i} = \{\mu_{j|i} : j \in V_{|i}\} \in \mathbb{R}^{d-1}$  and covariance matrix  $\Sigma_{|i}^*$ . To further simplify, they take  $\Sigma_{|i}^*$  to be diagonal so that the components of  $Z_{|i}$  are independent.

With these assumptions inference for each component  $Y_i$  can be performed separately. Let  $\{y^1, \dots, y^n\}$  be  $n$  independent and identically distributed observations. Conditional on  $Y_i$  being large, the parameters of both the normalising functions and the residual distribution can be obtained by maximising the likelihood

$$L_{|i}(\boldsymbol{\theta}_{|i}) = \prod_{k: y_i^k > u_{Y_i}} \phi_{d-1} \left[ \left\{ \frac{y_j^k - \alpha_{j|i}y_i^k}{(y_i^k)^{\beta_{j|i}}} \right\}_{j \in V_{|i}} ; \boldsymbol{\mu}_{|i}, \Sigma_{|i}^* \right] \prod_{j \in V_{|i}} (y_i^k)^{-\beta_{j|i}}, \quad (2.2)$$

where  $\phi_{d-1}(\cdot; \boldsymbol{\mu}_{|i}, \Sigma_{|i}^*)$  is the density of the  $(d-1)$ -dimensional MVG distribution. The second term in the product is the Jacobian arising from the transformation of  $Y_{|i}$  to  $Z_{|i}$ . To predict from the model Heffernan and Tawn (2004) use the empirical distribution of the fitted residuals

$$\hat{z}_{|i} = \{\hat{z}_{j|i} := (y_{j|i} - \hat{\alpha}_{j|i}y_i)y_i^{-\hat{\beta}_{j|i}} : j \in V_{|i}\}. \quad (2.3)$$

Here, hat notation denotes maximum likelihood estimates of parameters. The rationale for this is that, while the assumptions of independence and a Gaussian distribution are useful for parameter estimation, it is unlikely that they are appropriate.

## 2.2 Multivariate Asymmetric Generalised Gaussian Distribution

The CMEVM is very flexible, and parameter estimation has a low computational cost, making it an attractive option. Unfortunately, prediction does not scale well with dimension. The curse of dimensionality associated with sampling from the empirical distribution is well-known in general Nagler and Czado (2016), but we illustrate it in the specific case of the CMEVM in the Supplementary Material (Farrell et al., 2024). To overcome this limitation, we utilise a fully parametric model. While this approach has been taken by others (Richards et al., 2022; Shooter et al., 2021; Wadsworth and Tawn, 2022), the distribution that we propose allows, for the first time, a model with asymmetry in the univariate marginal distributions of the residuals. The most commonly used parametric model for  $Z_{|i}$  is the multivariate Gaussian copula with generalised Gaussian margins (Wadsworth and Tawn, 2022). The generalised Gaussian distribution is attractive because it bridges the Gaussian and Laplace distributions, meaning that it is appropriate in cases where the pairwise dependence of the residuals is expected to vary from strong asymptotic dependence (for which the residual margins are expected to follow a Gaussian distribution) to complete independence (for which the residual margins are expected to follow a Laplace distribution). However, the generalised Gaussian distribution is symmetric, a property that we found is not always appropriate (see Supplementary Material (Farrell et al., 2024)). Therefore, we propose to model the marginal distribution of the residuals  $Z_{|i}$  using the asymmetric generalised Gaussian (AGG) distribution Nacereddine and Goumeidane (2019). This distribution has density

$$f_Z(z) = \frac{\delta}{(\kappa_1 + \kappa_2)\Gamma(1/\delta)} \begin{cases} \exp\left\{-[(\nu - z)/\kappa_1]^\delta\right\} & \text{for } z < \nu \\ \exp\left\{-[(z - \nu)/\kappa_2]^\delta\right\} & \text{for } z \geq \nu, \end{cases} \quad (2.4)$$

where  $z \in \mathbb{R}$ ,  $\Gamma(\cdot)$  denotes the standard gamma function, and  $\nu \in \mathbb{R}$ ,  $\kappa_1 > 0$ ,  $\kappa_2 > 0$ ,  $\delta > 0$  are the location, left-scale, right-scale, and shape parameters, respectively. We refer to this distribution as the  $\text{AGG}(\nu, \kappa_1, \kappa_2, \delta)$ . When  $\kappa_1 = \kappa_2$ , the AGG reduces to the generalised Gaussian (or delta-Laplace) distribution used by Wadsworth and Tawn (2022).

For inference, it is helpful to separate the marginal and dependence properties of the residual vector  $Z_{|i}$  by defining

$$W_{j|i} := \Phi^{-1}(F_{Z_{j|i}}(Z_{j|i})), \quad j \in V_{|i},$$

where  $\Phi$  and  $F_{Z_{j|i}}$  are the distribution functions of the standard Gaussian and  $\text{AGG}(\nu, \kappa_1, \kappa_2, \delta)$  distributions, respectively. We then assume that  $W_{|i} = \{W_{j|i} : j \in V_{|i}\} \sim \text{MVG}_{d-1}(\mathbf{0}, \Sigma_{|i})$  where  $\Sigma_{|i}$  is a  $(d-1)$ -dimensional *correlation* matrix. We refer to this combination of marginal

and joint distributions as the multivariate asymmetric generalised Gaussian (MVAGG) distribution and denote this by  $Z_{|i} \sim \text{MVAGG}_{d-1}(\Theta_{|i}, \Theta_{|i}^\Gamma)$ , where  $\Theta_{|i} := \left\{ (\nu_{j|i}, \kappa_{2j|i}, \kappa_{1j|i}, \delta_{j|i}) : j \in V_{|i} \right\}$  and  $\Theta_{|i}^\Gamma$  parameterises the (sparse) precision matrix  $\Gamma_{|i} := (\Sigma_{|i})^{-1}$ . The density for this distribution is

$$f_i(z_{|i}) = \phi_{d-1} \left[ \left\{ \Phi^{-1} \left( F_{Z_{j|i}}(z_{j|i}) \right) \right\}_{j \in V_{|i}} ; \mathbf{0}, \Sigma_{|i} \right] \prod_{j \in V_{|i}} \frac{f_{Z_{j|i}}(z_{j|i})}{\phi \left[ \Phi^{-1} \left( F_{Z_{j|i}}(z_{j|i}) \right) \right]} \quad (2.5)$$

where  $f_{Z_{j|i}}$  is defined in equation (2.4), and  $\phi$  is the standard univariate Gaussian density.

### 2.3 Structured Conditional Multivariate Extreme Value Model

While a parametric model for the residual component of the CMEVM overcomes the main limitation faced when using the empirical distribution, it has the drawback of vastly increasing the number of parameters to be estimated. For example, the correlation matrix  $\Sigma_{|i}$  that parameterises the MVAGG distribution described in the previous section, increases the number of parameters from order  $d^2$  (the original CMEVM) to order  $d^3$ . We now explain how conditional independence structures can be used to address this challenge by introducing sparsity into the precision matrix  $\Gamma_{|i}$  associated with  $\Sigma_{|i}$ .

First, we introduce the terminology required for the model set-up. The conditional independence structure of a random vector  $W \sim \text{MVG}_d(\mathbf{0}, \Sigma)$  can be formulated by associating  $W$  with a simple undirected graph  $\mathcal{G} = (V, E)$ . This graph consists of vertex  $V = \{1, \dots, d\}$  and edge  $E \subseteq \{\{j, k\} \mid j, k \in V, j \neq k\}$  sets, with  $\{j, k\} \in E$  if and only if  $\{k, j\} \in E$ . The components  $W_j$  and  $W_k$  are conditionally independent given the remaining components if  $\{j, k\} \notin E$ . Since  $W$  additionally follows a Gaussian distribution, conditional independence of  $W_j$  and  $W_k$  implies that their partial correlation is zero and hence that  $\Gamma_{j,k} = \Gamma_{k,j} = 0$  where  $\Gamma = (\Sigma)^{-1}$  is the precision matrix of  $W$  Speed and Kiiveri (1986). Thus, a sparse precision matrix (equivalently a sparse graph  $\mathcal{G}$ ) can greatly reduce the dimension of the parameter space. We can now construct the structured CMEVM (or SCMEVM) by modelling the CMEVM residuals using a multivariate Gaussian copula, such that the structure of the precision matrix is determined by a suitable graph.

By way of introduction, we consider the case of conditioning on only a single component  $Y_i$ . Given that  $Y_i > u_{Y_i}$ , we define a conditional independence graph  $\mathcal{G}_{|i} = \{E_{|i}, V_{|i}\}$  associated with the  $(d-1)$ -dimensional residual vector  $W_{|i}$ . This graph might be defined by the topology on which the process is being measured, e.g. a road or river network, or it might be estimated

empirically. Assuming that the residuals  $Z_{|i}$  follow a MVAGG distribution, density (2.5) can be used to define the likelihood function such that the elements of the precision matrix  $\Gamma_{|i}$  that correspond to edges not in the edge set  $E_{|i}$  are set to zero. All other elements in the matrix are treated as free parameters to be estimated.

The naive approach to fitting the full SCMEVM model would be to repeat the above process for each of the  $d$  components. However this is inefficient since it requires individual selection of the  $d$  graphs  $G_{|1}, \dots, G_{|d}$ . To increase computational efficiency and to guarantee that the sub-graphs are consistent, we instead select a single  $d$ -dimensional graph  $\mathcal{G}$  which is then used to derive  $\mathcal{G}_{|1}, \dots, \mathcal{G}_{|d}$ . This presents two challenges: selection of the  $d$ -dimensional graph and inference of the sub-graphs.

The first of these challenges is addressed in detail in the following section, and so we proceed on the basis that the graph  $\mathcal{G}$  is identified. Recall that each graph  $G_{|i}$  is associated with the conditional independence structure of the  $(d-1)$ -dimensional residual vector  $W_{|i}$  with the “missing” component being the residual associated with the conditioning site. The reason for removing this component is that the normalising functions degenerate with  $a(y_{i|i}) = y$ , and hence the residuals at the conditioning site are always zero. When modelling the residuals non-parametrically, there is no information to be gained by including this degenerate component in the residual vector. This is not the case for parametric models, see Wadsworth and Tawn (2022). For each conditioning site, we therefore augment  $W_{|i}$  to include  $W_{i|i} = 0$ , resulting in a vector of length  $d$ . Exploiting text-book properties of the conditional Gaussian distribution, each  $(d-1)$ -dimensional precision matrix  $\Gamma_{|i}$  can then be obtained by excluding the  $i$ th row and column from  $\Gamma$  associated with  $\mathcal{G}$ . Since  $W$  is assumed to follow a Gaussian distribution, the graph  $\mathcal{G}_{|i}$  associated with  $W_{|i}$  is equivalently formed by removing the  $i$ th node and its incident edges from  $\mathcal{G}$ .

### 3 Inference

In this section, we focus on inference for the MVAGG SCMEVM, that is, the structured CMEVM described in Section 2.3 for which the residuals have the MVAGG distribution described in Section 2.2. The methods described could be easily adapted to any other residual distribution based on a Gaussian copula. We first describe an efficient inference procedure for the MVAGG SCMEVM and then provide algorithms for graphical selection and model-based predictions.

### 3.1 Parameter estimation

Given  $n$  independent and identically distributed realisations  $\{x^1, \dots, x^n\}$  of the  $d$ -dimensional random vector  $X$ , the first step is transformation to standard Laplace margins. By double application of the PIT, for each  $i \in V$  and each  $k \in \{1, \dots, n\}$ ,

$$y_i^k = \begin{cases} -\log \left( 2 \left[ 1 - \tilde{F}_i(x_i^k) \right] \right) & \tilde{F}_i(x_i^k) > 0.5, \\ \log \left( 2\tilde{F}_i(x_i^k) \right) & \tilde{F}_i(x_i^k) \leq 0.5, \end{cases}$$

where  $\tilde{F}_i$  is an estimate of the marginal distribution  $F_i$  for  $X_i$ . We use a semi-parametric estimate for  $F_i$  consisting of the empirical distribution for  $x_i \leq v_{X_i}$  and a generalised Pareto distribution for  $x_i > v_{X_i}$  (Heffernan and Tawn, 2004). The threshold  $v_{X_i}$  is selected using the automated method of Murphy et al. (2024).

Inference for the MVAGG SCMEVM is performed for each component  $Y_i$  separately by maximising the likelihood

$$L_{|i}(\boldsymbol{\theta}_{|i}) = \prod_{k: y_i^k > u_{Y_i}} f_i \left( \left\{ \frac{y_j^k - \alpha_{j|i} y_i^k}{(y_i^k)^{\beta_{j|i}}} \right\}_{j \in V_{|i}} ; \boldsymbol{\Theta}_{|i}, \boldsymbol{\Theta}_{|i}^\Gamma \right) \prod_{j \in V_{|i}} (y_i^k)^{-\beta_{j|i}}, \quad (3.1)$$

where  $f_i$  is given by equation (2.5),  $u_{Y_i}$  is the dependence threshold and  $\boldsymbol{\theta}_{|i} := (\boldsymbol{\Theta}_{|i}^d, \boldsymbol{\Theta}_{|i}, \boldsymbol{\Theta}_{|i}^\Gamma)$  combines the CMEVM dependence  $\boldsymbol{\Theta}_{|i}^d := \{(\alpha_{j|i}, \beta_{j|i}) : j \in V_{|i}\}$ , MVAGG marginal  $\boldsymbol{\Theta}_{|i}$  and MVAGG correlation  $\boldsymbol{\Theta}_{|i}^\Gamma$  parameters. Of the parameter vectors, only  $\boldsymbol{\Theta}_{|i}^\Gamma$  is determined by the graph associated with  $W_{|i}$ . The edge cases are the independent model (a graph with no edges implying a diagonal precision matrix), and the saturated model (a full graph implying a saturated precision matrix). Any other combination will be referred to as a graphical model.

The naive approach is to jointly estimate the full parameter vector  $\boldsymbol{\theta}_{|i}$ . A “one-step” numerical maximisation procedure for this is given in Algorithm 3.1. The algorithm iterates between maximising the profile likelihood for  $\boldsymbol{\Theta}_{|i}^\Gamma$  and maximising the profile likelihood for  $(\boldsymbol{\Theta}_{|i}, \boldsymbol{\Theta}_{|i}^d)$ . Numerical optimisation of the profile likelihood for  $\boldsymbol{\Theta}_{|i}^\Gamma$  is only required for non-trivial graphical structures; analytical expressions for  $\hat{\Gamma}_{|i} = (\hat{\Sigma}_{|i})^{-1}$  are available if the residuals are either independent or have saturated covariance structure. For the general graphical model, we use the graphical lasso (Friedman et al., 2007, 2019) to penalise elements where edges do not exist in  $\mathcal{G}_{|i}$ , ensuring that the corresponding entries in  $\hat{\Gamma}_{|i}$  are exactly 0. The same approach is taken in step 5 of Algorithm 3.3 and in step 5 of Algorithm 3.4.

---

**Algorithm 3.1** One-step parameter estimation for the MVAGG SCMEVM

---

- 1: Initialise  $\Theta_{|i}^d$ ,  $\Theta_{|i}$ ,  $\mathcal{G}_{|i} = (V_{|i}, E_{|i})$ , and  $\mathbf{tol}$ ;
  - 2: The current values of  $\Theta_{|i}^d$  and  $\Theta_{|i}$  are  $\Theta_{|i}^{d*}$  and  $\Theta_{|i}^*$ , respectively;
  - 3: Obtain  $\hat{\Theta}_{|i}^\Gamma = \operatorname{argmax}_{\Theta_{|i}^\Gamma} L_{|i} \left( \Theta_{|i}^{d*}, \Theta_{|i}^*, \Theta_{|i}^\Gamma \right)$ , where  $L_{|i}$  is likelihood (3.1) using Algorithm 3.2;
  - 4: Obtain  $\left( \hat{\Theta}_{|i}^d, \hat{\Theta}_{|i} \right) = \operatorname{argmax}_{\Theta_{|i}^d, \Theta_{|i}} L_{|i} \left( \Theta_{|i}^d, \Theta_{|i}, \hat{\Theta}_{|i}^\Gamma \right)$ ;
  - 5: **if**  $\max(|\hat{\Theta}_{|i}^d - \Theta_{|i}^{d*}|, |\hat{\Theta}_{|i} - \Theta_{|i}^*|) > \mathbf{tol}$  **then**
  - 6:   Set  $\Theta_{|i}^d = \hat{\Theta}_{|i}^d$  and  $\Theta_{|i} = \hat{\Theta}_{|i}$ ;
  - 7:   Repeat steps 2 - 4;
  - 8: **else**
  - 9:   **return**  $\hat{\Theta}_{|i}^d$ ,  $\hat{\Theta}_{|i}$  and  $\hat{\Theta}_{|i}^\Gamma$
  - 10: **end if**
- 

This procedure has limitations. Firstly, the parameter space cannot be easily constrained to ensure that the first-order extremal dependence structure is captured by  $\Theta_{|i}^d$  and not the residual distribution. Secondly, even for a sparse precision matrix  $\Gamma_{|i}$ , the number of parameters to jointly maximise grows at least linearly in  $d$ , and finding suitable starting values for the optimisation becomes difficult for large  $d$ . We therefore prefer the two- and three-step procedures described in Algorithms 3.3 and 3.4, respectively. Both approaches combat the first limitation. However, the two-step approach still requires a high-dimensional, computationally expensive, numerical optimisation procedure of the MVAGG distribution described in Section 2.2. The three-step approach circumvents this and is therefore our preference. Lastly, we observe that there is no information gained by jointly fitting the  $d$  conditional models since the parameter values in the MVAGG may differ with each conditioning variable; this is in contrast to the spatial CMEVM (Richards et al., 2022; Wadsworth and Tawn, 2022) which has a stationary residual spatial process and hence the parameters do not change with the conditioning site.

### 3.2 Graph selection

The graphical structure may not be known *a priori*. Therefore, we require a method to determine the optimal graphical structure  $\mathcal{G}$ . Recall that  $\mathcal{G}$  is defined for the augmented vector  $W$ , not  $W_{|i}$ . Consequently, we could learn the graph for  $W$  using a composite likelihood. This would ensure consistency but would require multiple likelihood ratio tests and reduce the power of the test. Alternatively, we could iteratively add edges to  $\mathcal{G}$  that minimise the AIC (Engelke and Hitz, 2020). However, this is computationally expensive when  $d$  is large.

---

**Algorithm 3.2** Estimating  $\hat{\Theta}_{|i}^\Gamma$ 


---

- 1: Initialise  $\hat{\Theta}_{|i}^d$ ,  $\hat{\Theta}_{|i}$ , and  $\mathcal{G}_{|i} = (V_{|i}, E_{|i})$ ;
  - 2: Obtain  $\hat{z}_{|i}$  using equation (2.3) and  $\hat{\Theta}_{|i}^d$ ;
  - 3: Obtain  $\hat{w}_{|i}$  such that  $\hat{w}_{j|i} = \Phi^{-1}(F_{Z_{j|i}}(\hat{z}_{j|i}; \hat{\Theta}_{j|i}))$ ;
  - 4: **if**  $|E_{|i}| = 0$  **then** *Independence*
  - 5:      $\hat{\Theta}_{|i}^\Gamma = I_{d-1}$  (the  $(d-1)$ -dimensional identity matrix);
  - 6: **else if**  $|E_{|i}| = d(d-1)/2$  **then** *Saturated*
  - 7:      $\hat{\Theta}_{|i}^\Gamma = (\text{corr}(\hat{W}_{|i}))^{-1}$ ;
  - 8: **else** *Graphical*
  - 9:      $\hat{\Theta}_{|i}^\Gamma$  is estimated using a graphical lasso (Friedman et al., 2019) on  $\hat{W}_{|i}$ ;
  - 10: **return**  $\hat{\Theta}_{|i}^\Gamma$
- 

Our approach, detailed in Algorithm 3.5, uses the graphical lasso (Friedman et al., 2007) to learn the graphical structure of  $W_{|i}$ , for each  $i \in V$ . Since this need not result in consistent graphical structures, the  $d$  subgraphs are combined into a weighted graph  $\mathcal{G}^*$  and a majority rule is used to determine the best overall graph  $\hat{\mathcal{G}}$ . The approach has two tuning parameters: the CMEVM dependence threshold, and the graphical lasso penalisation parameter. The former can be checked with diagnostics discussed in Southworth et al. (2024). For the graphical lasso, we implement the procedure for several feasible values and select the final graph using another majority rule.

### 3.3 Prediction

By construction, the CMEVM does not have closed forms for either tail probabilities or quantiles. Heffernan and Tawn (2004) use a simulation-based prediction algorithm which samples from the empirical distribution of the fitted residuals  $\hat{Z}_{|i}$ . The model proposed in Section 2 allows for fully parametric predictions using a method that is very similar to that used by Wadsworth and Tawn (2022, Section 5.2.2) and Richards et al. (2022, Section 3.3).

We first note that the model describes

$$\left\{ F_{X_i}^{-1}(F_L(Y_i)) : i \in V \right\} \left| \left( \max_{i \in V} Y_i > u \right), \quad (3.2)$$

such that  $u > \max(u_{Y_i} : i \in V)$  where  $u_{Y_i}$  is the dependence threshold used to fit our model in Section 3.1, and  $F_L$  denotes the distribution function of the standard Laplace distribution. To create realisations of  $X$ , we draw samples from equation (3.2) using Algorithm 3.6 with

---

**Algorithm 3.3** Two-step parameter estimation for the MAVGG SCMEVM
 

---

- 1: Initialise  $\Theta_{|i}^d$ ,  $\Theta_{|i}$ ,  $\mathcal{G}_{|i} = (V_{|i}, E_{|i})$ , and  $\text{tol}$ ;
  - 2: Assuming independent Gaussian residuals, obtain  $\hat{\Theta}_{|i}^d$  by maximising likelihood (2.2);
  - 3: Using equation (2.3) and  $\hat{\Theta}_{|i}^d$ , obtain  $\hat{z}_{|i}$  and treat them as fixed;
  - 4: The current value of  $\Theta_{|i}$  is  $\Theta_{|i}^*$ ;
  - 5: Obtain  $\hat{\Theta}_{|i}^\Gamma = \underset{\Theta_{|i}^\Gamma}{\operatorname{argmax}} L_{|i} \left( \hat{\Theta}_{|i}^d, \Theta_{|i}^*, \Theta_{|i}^\Gamma \right)$ , where  $L_{|i}$  is likelihood (3.1) using Algorithm 3.2;
  - 6: Obtain  $\hat{\Theta}_{|i} = \underset{\Theta_{|i}}{\operatorname{argmax}} L_{|i} \left( \hat{\Theta}_{|i}^d, \Theta_{|i}, \hat{\Theta}_{|i}^\Gamma \right)$ ;
  - 7: **if**  $\max(|\hat{\Theta}_{|i} - \Theta_{|i}^*|) > \text{tol}$  **then**
  - 8: set  $\Theta_{|i} = \hat{\Theta}_{|i}$ ;
  - 9: repeat 4 - 6;
  - 10: **else**
  - 11: **return**  $\hat{\Theta}_{|i}$  and  $\hat{\Theta}_{|i}^\Gamma$ .
  - 12: **end if**
  - 13: **return**  $\hat{\Theta}_{|i}^d$ ,  $\hat{\Theta}_{|i}$  and  $\hat{\Theta}_{|i}^\Gamma$
- 

probability

$$\mathbb{P} \left( \max_{i \in V} Y_i > u \right) = \frac{1}{n} \sum_{k=1}^n \mathbb{1} \left\{ \max_{i \in V} y_i^k > u \right\}. \quad (3.3)$$

Otherwise, we draw realisations from the empirical distribution of  $X \mid \left( \max_{i \in V} Y_i < u \right)$ .

## 4 Simulation Study

In this section, we use simulation studies to assess the performance of the SCMEVM. The stepwise inference procedures are investigated in Section 4.1, and the graphical selection process is assessed in Section 4.2. Section 4.3 compares the SCMEVM to existing methods.

### 4.1 Stepwise inference procedures

Using data simulated from the SCMEVM with a graphical covariance structure, we compare parameter estimation for the one-(Algorithm 3.1), two-(Algorithm 3.3), and three-step (Algorithm 3.4) procedures with independent, graphical and saturated covariance structures (previous algorithms in conjunction with Algorithm 3.2). We use the graph  $\mathcal{G} = (V, E)$ ,  $V = \{1, \dots, 5\}$  and  $E = \{\{1, 2\}, \{1, 3\}, \{2, 3\}, \{3, 4\}, \{3, 5\}, \{4, 5\}\}$ . For each  $i \in V$ , we simulate the conditioning variable  $Y_i \mid Y_i > u_{Y_i}$  from a standard Laplace distribution with  $u_{Y_i} = -\log(0.4)$  (the 0.80-quantile of this distribution). We obtain  $Z_{|i}$  from a MVAGG dis-

---

**Algorithm 3.4** Three-step parameter estimation for the MAVGG SCMEVM
 

---

- 1: Initialise  $\Theta_{|i}^d$ ,  $\Theta_{|i}$ ,  $\mathcal{G}_{|i} = (V_{|i}, E_{|i})$ , and  $\text{tol}$ ;
  - 2: Assuming independent Gaussian residuals, obtain  $\hat{\Theta}_{|i}^d$  by maximising likelihood (2.2);
  - 3: Using equation (2.3) and  $\hat{\Theta}_{|i}^d$ , obtain  $\hat{z}_{|i}$  and treat them as fixed;
  - 4: Assuming that the components of  $\hat{Z}_{|i}$  are independent, obtain  $\hat{\Theta}_{|i} = \underset{\Theta_{|i}}{\operatorname{argmax}} f_i(\hat{z}_{|i}; \Theta_{|i}, I_{d-1})$  where  $f_i$  is given by equation (2.5), and  $I_{d-1}$  is a  $(d-1)$ -dimensional identity matrix;
  - 5: Obtain  $\hat{\Theta}_{|i}^\Gamma = \underset{\Theta_{|i}^\Gamma}{\operatorname{argmax}} L_{|i}(\hat{\Theta}_{|i}^d, \hat{\Theta}_{|i}, \Theta_{|i}^\Gamma)$ , where  $L_{|i}$  is likelihood (3.1) using Algorithm 3.2;
  - 6: **return**  $\hat{\Theta}_{|i}^d$ ,  $\hat{\Theta}_{|i}$  and  $\hat{\Theta}_{|i}^\Gamma$
- 

---

**Algorithm 3.5** Graphical selection using the MVAGG SCMEVM
 

---

- 1: Initialise  $\rho$ ;
  - 2: **for**  $i = 1, \dots, d$  **do**
  - 3: Assuming independent Gaussian residuals, obtain  $\hat{\Theta}_{|i}^d$  by maximising likelihood (2.2);
  - 4: Using equation (2.3) and  $\hat{\Theta}_{|i}^d$ , obtain  $\hat{z}_{|i}$  and treat them as fixed;
  - 5: Assuming that the components of  $\hat{Z}_{|i}$  are independent, obtain  $\hat{\Theta}_{|i} = \underset{\Theta_{|i}}{\operatorname{argmax}} f_i(\hat{z}_{|i}; \Theta_{|i}, I_{d-1})$  where  $f_i$  is given by equation (2.5) and  $I_{d-1}$  is a  $(d-1)$ -dimensional identity matrix;
  - 6: Set  $\Theta_{|i} = \hat{\Theta}_{|i}$  and treating as fixed marginally transform  $\hat{z}_{|i}$  onto standard Gaussian margins  $\hat{w}_{|i}$ ;
  - 7: Apply a graphical lasso with penalisation parameter  $\rho$  to  $\hat{W}_{|i}$  to infer the subgraph  $\mathcal{G}_{|i}$ ;
  - 8: **end for**
  - 9: Obtain a weighted graph  $\mathcal{G}^*$  by combining the subgraphs  $\mathcal{G}_{|i}$ ;
  - 10: Create  $\hat{\mathcal{G}}$  by pruning the edges of  $\mathcal{G}^*$  that do not occur at least 50% of the time;
  - 11: **return**  $\hat{\mathcal{G}}$
- 

tribution by (i) simulating  $W_{|i}$  from a MVG distribution with standard Gaussian margins and correlation matrix  $\Sigma_{|i}$  and (ii) transforming  $W_{|i}$  onto AGG margins via the PIT. Using limit (2.1), we obtain  $Y_{|i}$ , and thereby a full  $d$ -dimensional vector for  $Y \mid Y_i > u_{Y_i}$ . We generate 200 samples of  $Y \mid Y_i > u_{Y_i}$  and consider  $n \in \{250, 500\}$ . The true dependence and AGG parameters are independently sampled from a uniform distribution on  $(0.1, 0.5)$  for  $\alpha_j$ ,  $(0.1, 0.3)$  for  $\beta_j$ ,  $(-5, 5)$  for  $\nu_j$ ,  $(0.5, 2)$  for  $\kappa_{1,j}$ ,  $(1.5, 3)$  for  $\kappa_{2,j}$ , and  $(0.8, 2.5)$  for  $\delta_j$ , for each  $j \in V$ . Entries in  $\Sigma_{|i}$  correspond to weak positive associations; see Supplementary Material (Farrell et al., 2024) for examples with weak negative or strong positive associations.

From Algorithms 3.3 and 3.4, we observe that the estimates of  $\Theta_{|i}^d$  for the SCMEVM are the same across all two- and three-step procedures. Therefore, we restrict our comparison

---

**Algorithm 3.6** Simulation of equation (3.2)
 

---

- 1: Initialise  $u$ ;
  - 2: **for**  $l = 1, \dots, N$  such that  $N > n$  **do**
  - 3: Draw a conditioning random variable  $i$  from  $i \in V$  with uniform probability;
  - 4: Simulate  $E^l \sim \text{Exp}(1)$  and set  $y_i^l = u + E^l$ ;
  - 5: Simulate  $z_{j|i}^l$  from the distribution described in Section 2.2;
  - 6: Calculate  $y_{j|i}^l = \hat{\alpha}_{j|i} y_i^l + (y_i^l)^{\hat{\beta}_{j|i}} z_{j|i}^l$  for  $j \in V_{|i}$ ;
  - 7: Calculate an importance weight  $w^l = \left( \frac{1}{d} \sum_{m=1}^d \mathbb{1}\{y_m^l > u\} \right)^{-1}$ .
  - 8: **end for**
  - 9: Sub-sample  $n$  realisations from  $\{y^1, \dots, y^N\}$  with probabilities proportional to their importance weights;
  - 10: Transform the sub-sample  $\{y^1, \dots, y^n\}$  to  $\{x^1, \dots, x^n\}$  via a double application of the PIT;
  - 11: **return**  $\{x^1, \dots, x^n\}$
- 

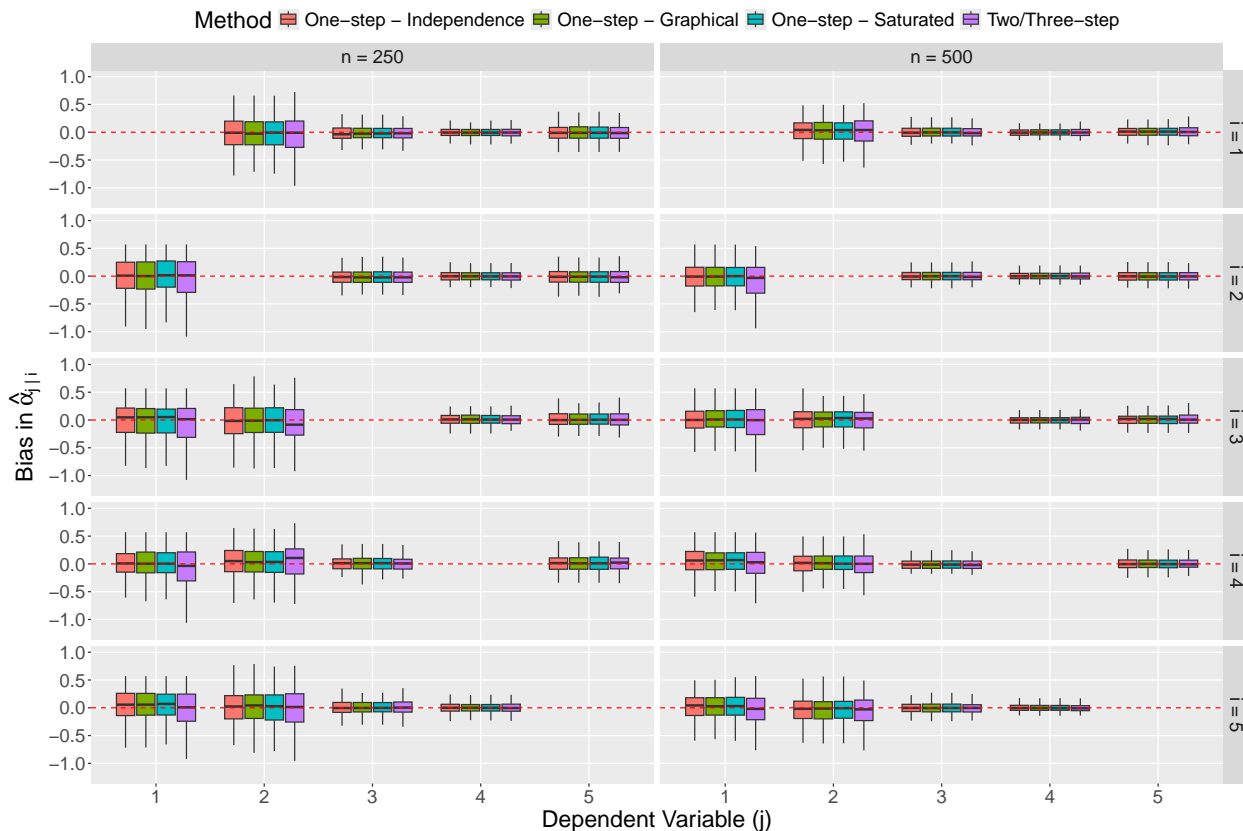


Figure 2: Boxplots detailing the bias of  $\hat{\alpha}_{j|i}$  for distinct  $i, j \in V$ . Each row corresponds to the conditioning variable  $i$ , and each column corresponds to the sample size. The fill of the boxplots denotes the different models. The red dashed line indicates the  $y = 0$  line.

to the one-step (all three structures) and two-step (independence model only) procedures. Figure 2 shows the bias in  $\hat{\alpha}_{j|i}$  while the Supplementary Material (Farrell et al., 2024) pro-

Table 1: Median (2.5% and 97.5% quantiles) bias in the fitted maximum log-likelihood values. Bold values denote the least biased stepwise inference procedure for each covariance structure type and conditioning variable.

Covariance Structure		Independent			Graphical			Saturated		
Number of Excesses	Conditioning Variable	One-step	Two-step	Three-step	One-step	Two-step	Three-step	One-step	Two-step	Three-step
250	1	<b>-4.8</b> (-18.3, 8.7)	-6.2 (-19.3, 8.2)	-6.2 (-19.3, 8.2)	14.0 (7.6, 22.5)	12.8 (6.3, 21.5)	<b>12.7</b> (6.7, 21.4)	14.8 (7.6, 25.1)	13.6 (6.4, 24.1)	<b>13.5</b> (7.0, 24.0)
	2	<b>-4.2</b> (-20.6, 11.7)	-4.9 (-18.9, 10.0)	-4.9 (-18.9, 10.0)	14.2 (7.2, 23.6)	<b>11.9</b> (5.4, 21.8)	<b>11.9</b> (5.4, 21.7)	15.3 (8.0, 25.1)	13.2 (6.4, 23.0)	<b>13.1</b> (6.2, 22.9)
	3	<b>0.1</b> (-11.9, 13.1)	-1.6 (-12.3, 10.7)	-1.6 (-12.3, 10.7)	13.2 (7.1, 22.7)	<b>11.1</b> (4.7, 21.3)	<b>11.1</b> (4.8, 21.2)	15.1 (7.8, 25.6)	<b>13.2</b> (5.4, 24.3)	13.4 (5.6, 24.2)
	4	<b>-3.7</b> (-18.2, 11.5)	-5.2 (-19.4, 9.9)	-5.2 (-19.4, 9.9)	13.6 (8.2, 21.5)	12.3 (5.9, 20.0)	<b>12.2</b> (5.9, 19.9)	14.5 (7.7, 23.1)	<b>13.3</b> (6.6, 21.6)	<b>13.3</b> (6.7, 21.6)
	5	<b>-13.3</b> (-34.1, 3.3)	-14.8 (-30.0, 2.3)	-14.8 (-30.0, 2.3)	13.5 (7.6, 22.2)	12.2 (4.7, 21.3)	<b>12.0</b> (5.3, 21.0)	14.4 (8.7, 24.1)	<b>12.9</b> (5.2, 22.5)	<b>12.9</b> (6.2, 22.4)
500	1	<b>-20.9</b> (-35.9, -4.9)	-22.4 (-39.0, -6.0)	-22.4 (-39.0, -6.0)	14.4 (9.0, 21.3)	<b>12.8</b> (7.1, 20.1)	<b>12.8</b> (7.1, 20.0)	15.2 (9.1, 22.7)	<b>13.6</b> (7.6, 21.0)	<b>13.6</b> (7.5, 20.9)
	2	<b>-20.1</b> (-36.5, -0.3)	-22.0 (-37.0, -2.1)	-22.0 (-37.0, -2.1)	13.8 (7.4, 22.0)	12.0 (4.8, 20.7)	<b>11.9</b> (5.4, 20.6)	14.9 (8.4, 23.4)	13.4 (5.9, 22.4)	<b>13.3</b> (6.0, 22.3)
	3	<b>-13.4</b> (-30.9, 2.6)	-16.2 (-31.5, 1.3)	-16.2 (-31.5, 1.3)	13.0 (7.1, 20.9)	<b>10.5</b> (3.4, 19.3)	10.6 (3.6, 19.3)	14.9 (8.9, 22.9)	12.9 (5.4, 20.8)	<b>12.8</b> (5.2, 20.7)
	4	<b>-17.9</b> (-33.9, -0.7)	-19.9 (-36.2, -3.8)	-19.9 (-36.2, -3.8)	14.2 (8.2, 24.3)	<b>12.1</b> (5.0, 21.3)	<b>12.1</b> (5.0, 21.3)	15.1 (8.5, 24.8)	<b>13.2</b> (5.4, 22.1)	<b>13.2</b> (5.4, 22.0)
	5	<b>-37.0</b> (-58.1, -18.8)	-39.0 (-60.3, -20.7)	-39.0 (-60.3, -20.7)	13.8 (7.5, 21.9)	<b>12.0</b> (5.1, 20.5)	<b>12.0</b> (5.1, 20.4)	14.7 (8.6, 24.1)	<b>12.9</b> (6.3, 21.7)	13.0 (6.4, 21.6)

vides comparisons for the remaining parameters, yielding similar findings. Despite using the stepwise procedure, the two-step method converges to the true parameter estimates. When comparing the one- and two-step methods, we find that the former has a slightly narrower range of bias, while the latter has fewer instances of unusually large bias. As expected, the variability in bias decreases as the sample size increases for both procedures.

Table 1 presents the biases of the fitted maximum log-likelihood values. Although the SCMEVMs with graphical or saturated covariance exhibit slightly higher bias than the independent residuals model, the bias is consistent across all three stepwise procedures. Furthermore, we observe that the bias increases with sample size for the independent residual models, while for the graphical and saturated residual models, it remains similar for both  $n = 250$  and  $n = 500$ . This suggests that the structured models are more robust to sample size changes.

Having assessed the accuracy of the stepwise procedures, we now evaluate their computational efficiency. We draw a single realisation from the model for  $n \in \{250, 500, 1000, 2000, 4000\}$  excesses above the dependence threshold, and for dimensions  $d \in \{5, 10, 15\}$ . To enable comparisons across dimensions, the proportion of edges in each graph is set to 60% of its maximum number of edges. Model fitting is performed on a Dell Latitude 7,420 machine with 16GB of RAM, and an 11th generation Intel Core i5 processor with 8 cores. Figure 6 (left panel) shows the time taken in seconds (on the log scale) to fit the one-, two-, and three-step SCMEVMs with graphical and saturated covariance structures. We observe that

Table 2: Average time in seconds (2dp) to complete various components of the three-step model fitting procedure for different dimensions.

Inference step	Dimension				
	100	200	300	400	500
Dependence parameters	1.34	2.07	2.84	3.65	4.42
AGG parameters	0.94	1.71	2.65	3.64	4.61
Graphical covariance structure	0.10	0.81	3.61	11.06	30.25
Saturated covariance structure	0.03	0.10	0.22	0.38	0.60

the one- and two-step methods are considerably slower to fit due to jointly maximising likelihood functions, with at least  $6(d-1)$  and  $4(d-1)$  parameters per conditioning variable, respectively. Additionally, the high-dimensional parameter space makes it challenging to find starting values for the numerical optimisation. The three-step method is computationally more efficient, showing considerable time savings when  $n$ ,  $d$ , or both, are large.

Since Figure 6 (left panel) shows that the three-step procedure with saturated covariance can be quicker to fit than its sparse graphical counterpart, we repeat the study for these two models with  $n = 4,000$  and  $d \in \{100, 200, 300, 400, 500\}$ . We set the proportion of edges in each graph to be 10% of its maximum number of edges. Table 2 shows the average time taken to complete each inference step. As expected, a significant amount of time is spent estimating the graphical structure due to the computational costs of the graphical lasso (Friedman et al., 2007). In contrast, the saturated covariance can be estimated empirically, i.e., no numerical maximisation is required, and the computational cost is primarily from inverting a  $(d-1)$ -dimensional correlation matrix.

## 4.2 Graphical selection

We now replicate the simulation study of Engelke and Hitz (2020, Section 5.5) to assess how well the SCMEVM identifies the structure  $\mathcal{G}$ , shown in Figure 3 (left panel). In this example,  $d = 16$  and the data generating mechanism is the Hüsler-Reiss distribution with parameter matrix consistent with  $\mathcal{G}$ . The parameters for each of the  $p = 18$  edges are sampled independently from a uniform distribution on  $(0.5, 1)$ , subject to the constraint that the parameter matrix must be conditionally negative definite on cliques with three nodes. We use 100 replicates of the dataset.

We apply Algorithm 3.5 to infer the optimal graphical structure using the 0.70-quantile of the standard Laplace distribution for the dependence threshold  $u_{Y_i}$ . The graphical lasso penalty parameter is set to 0.6. Figure 3 (right panel) shows a weighted graph with line width and

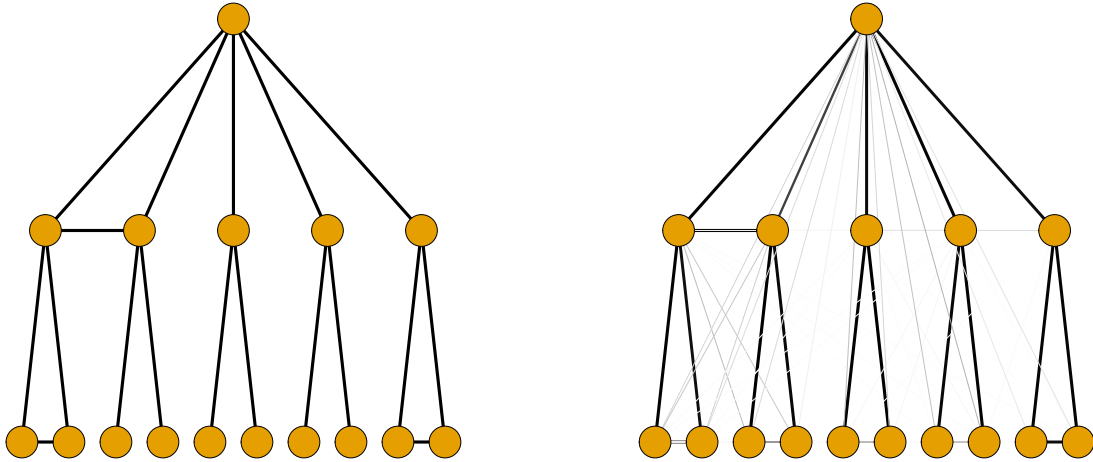


Figure 3: True underlying graphical structure (left) and the inferred graphical structure (right), with line width and darkness indicating the number of times each edge was selected across 100 samples.

darkness proportional to the number of times the edge is selected across the 100 datasets. The true graphical structure  $\mathcal{G}$  is identified. Moreover, using a majority rule to prune the edges of the weighted graph leaves only one surplus edge compared to the truth. The true graph is recovered by repeating for  $\rho \in \{0.60, 0.61, \dots, 0.70\}$  and taking a majority rule over the 11 inferred graphs. Therefore, averaging over multiple penalisation parameters may be beneficial where possible.

Despite being based on different underlying models and having different steps in the graphical selection process, both our graphical selection method and the Engelke and Hitz (2020) method accurately infer the underlying graphical structure, with the Engelke and Hitz (2020) method performing slightly better. This latter result is not unexpected since the data satisfy the assumption of AD required by the Engelke and Hitz (2020) method. In contrast, AD is an edge case of our model. A second simulation study, with data generated from the asymptotically independent multivariate Gaussian distribution, is provided in the Supplementary Material (Farrell et al., 2024) demonstrates that our method is more generally applicable than the Engelke and Hitz (2020) method.

### 4.3 Mixture data

To test the general applicability of our model, we use data with a mixture of extremal behaviour. For studies of data with full AI/AD see the Supplementary Material (Farrell et al., 2024). To simulate the mixed data, we sample from a 3-dimensional Pareto distribution consistent with a fully connected graph before marginally transforming the data onto standard Gaussian margins, denoted  $(X_1, X_2, X_3)$ , using a double application of the PIT. Next, we simulate  $(X_4, X_5) \mid X_3 = x_3$  from a conditional Gaussian distribution, such that the precision matrix of  $(X_3, X_4, X_5)$  is consistent with a fully connected graph. Then  $X$  follows some multivariate distribution with a dependence structure consistent with  $\mathcal{G}$  in Section 4.1. A total of 200 datasets are simulated.

Each of the one-, two- and three-step procedures (Algorithms 3.1 - 3.4) are used to fit the SCMEVM with graphical covariance. The SCMEVMs with independent and saturated covariances are fitted using only the three-step procedure. For comparison with existing methods we fit the CMEVM as described in Heffernan and Tawn (2004) and the graphical extremes model of Engelke and Hitz (2020) (EHM). For the SCMEVMs with graphical covariance structure and the EHM, we use the graph  $\mathcal{G}$  defined in Section 4.1. Models are compared using their model-based tail probability estimates; true probabilities are obtained from a sample of size  $10^6$  from the true distribution.

Selection of the threshold  $u_{Y_i}$  requires some consideration. For this data, subsets of the components could be either fully AD or fully AI or a mixture of the two. Consequently, the rate of convergence of the limiting dependence structures will vary across conditioning variables, so using different thresholds for each conditioning variable may be preferable. In practice, such information would not be readily available before fitting the model. Therefore, we proceed by taking the threshold for each component to be the 0.90-quantile of the standard Laplace distribution, giving an average of 500 exceedances per conditioning variable.

Figure 4 shows empirical and model-based estimates of the conditional precision matrix  $\Gamma_{\setminus i}$ . The empirical estimates are obtained by inverting the empirical correlation matrix of  $Y \mid Y_i > u_{Y_i}$  and then excluding the  $i$ th row and column. We first compare the precision matrix estimates across models; the estimates are almost identical for the graphical and saturated SCMEVMs, confirming there is negligible loss in using the former. The magnitudes of the non-zero entries in the residual precision matrices cannot be directly compared to their empirical equivalents due to the non-linearity of the transformation (2.1). We can compare the location of the zero entries and find that the graphical and saturated SCMEVM estimates are consistent with their empirical equivalents. This suggests that the graphical structure of the residual distribution is inherited from the underlying multivariate distribution, a result



Figure 4: Boxplots of empirical and model-based estimates of  $\Gamma_{|i}$ , for each  $i \in V$ , when the data is generated from a mixture distribution. Each row corresponds to the conditioning variable  $i$ , and each column corresponds to the correlation parameter. The colour of the boxplots distinguishes the different models. The black dashed line indicates the  $y = 0$  line.

that is consistent both with the theoretical findings of Casey and Papastathopoulos (2023) and similar simulation studies for cases with full AI or full AD (Supplementary Material, Farrell et al. (2024)).

Figure 5 shows the bias in the estimates for the tail probabilities  $p_1 = \mathbb{P}[X_1 > v_1, X_2 > v_2 \mid X_3 > u_3]$  and  $p_2 = \mathbb{P}[X_3 > v_3, X_4 > v_4 \mid X_5 > u_5]$ , where  $u_i$  and  $v_i$  are the 0.90-quantile and 0.95-quantile of  $X_i$ , respectively. Quantiles are obtained from a sample of size  $10^6$  from the true distribution. Estimates from the CMEVM and the SCMEVM with graphical or saturated covariances are unbiased for  $p_1$  and exhibit a small positive bias for  $p_2$ . Similarly, the EHM estimates of  $p_1$  are unbiased while the estimates of  $p_2$  have considerably larger positive bias than that seen from the (S)CMEVM models. These patterns are consistent across estimates of the remaining 73 conditional probabilities of the form  $\mathbb{P}[X_A > v \mid X_i > v]$  for  $A \subseteq V_{|i}$  and  $i \in V$ . When conditioning on sites 4 and 5, there is always some small positive bias in the estimates from the CMEVM and SCMEVM. Since the bias is consistent across the two models, we believe this is due to the difference in the rate at which the different

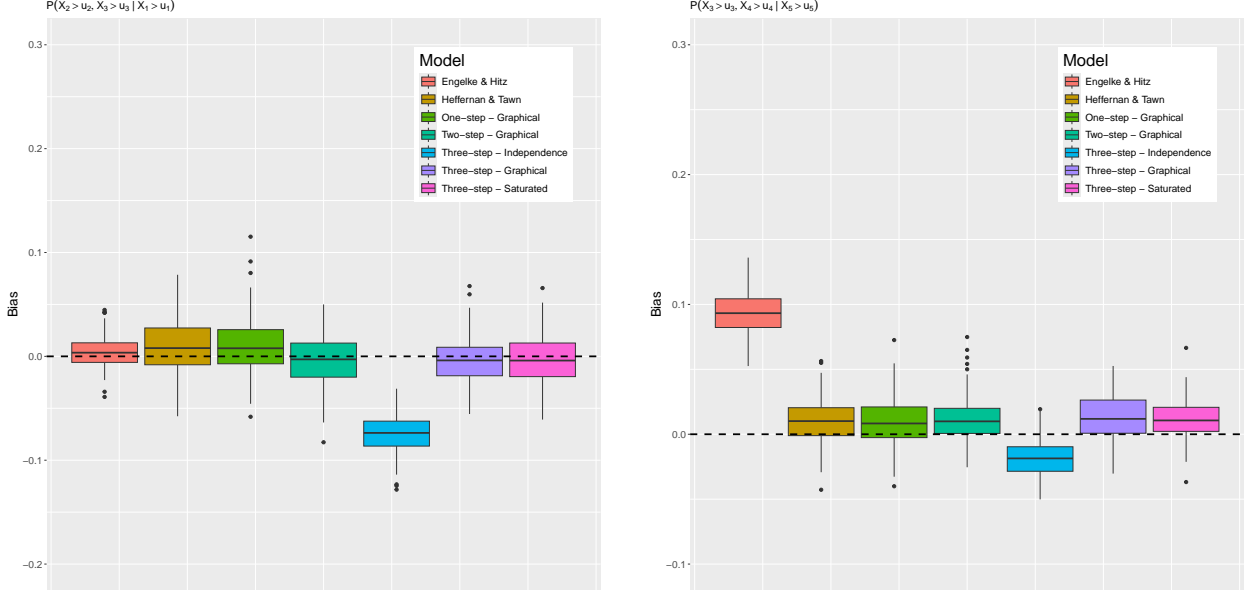


Figure 5: Boxplots of the bias in  $p_1 = \mathbb{P}[X_1 > v_1, X_2 > v_2 \mid X_3 > u_3]$  (left) and  $p_2 = \mathbb{P}[X_3 > v_3, X_4 > v_4 \mid X_5 > u_5]$  (right). The fill of the boxplots distinguishes the bias from the different models. The black dashed line indicates the  $y = 0$  line.

components of the generating distribution converge to the tail distribution. This bias may be reduced if lower dependence thresholds were used for these sites.

Finally, we consider the mean absolute error (MAE) and root mean square error (RMSE) of the estimates for all 75 conditional tail probabilities. The SCMEVM vastly outperforms both the EHM and CMEVM, minimising the MAE for 73% of the probabilities and the RMSE for 76% of them. In contrast, the CMEVM (EHM) minimises the MAE 15% (12%) and the RMSE 12% (12%) of the time. This suggests that even for moderate  $d$  the SCMEVM has greater predictive precision and accuracy than the nearest competitor methods.

## 5 Application

We apply our model to the upper Danube River discharge data described in Section 1. For the margins, we use the empirical-generalised Pareto distribution model from Section 3. The dependence threshold  $u_{Y_i}$  used is the 0.80-quantile of the standard Laplace distribution for all  $i \in V$ , resulting in around 85 excesses per station.

We use the three-step procedure to fit the SCMEVM with graphical covariance structure given by the undirected tree induced by the flow connections of the river (Figure 1, left panel); we also fit the EHM with the same structure. Since the flow connection tree may not be the optimal structure for describing the extremes, we also apply the three-step procedure

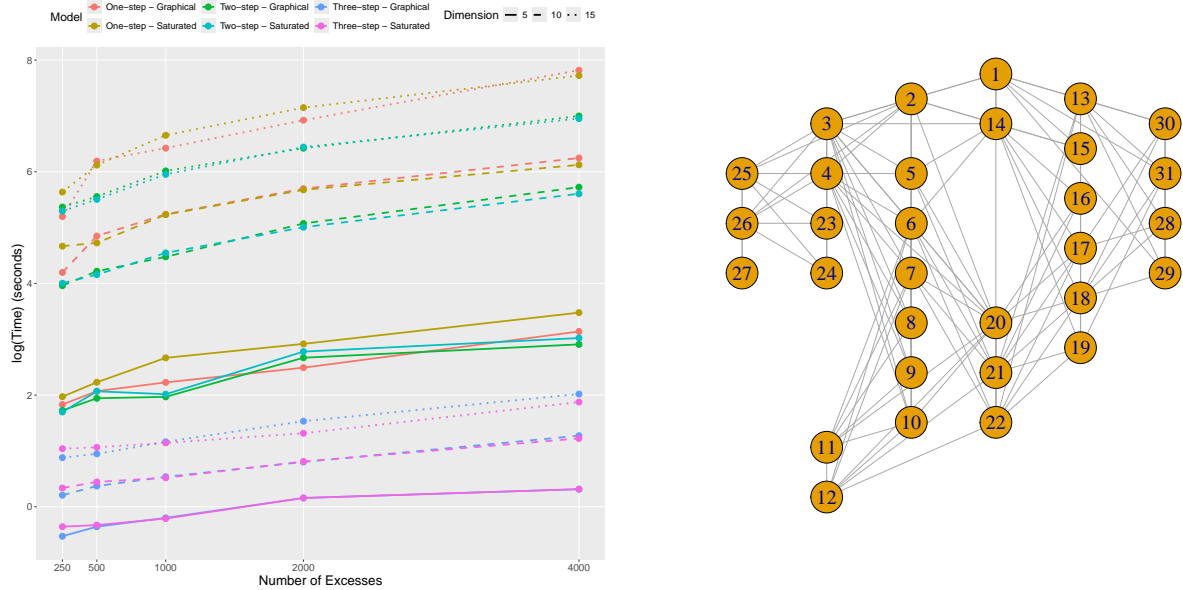


Figure 6: Timing comparison (log scale) of the SCMEVMs (left) for various sample sizes and dimensions, denoted by the line type, and models, denoted by the line colour. Inferred graphical structure of the upper Danube River basin using Algorithm 3.5 (right).

to fit both the SCMEVM with saturated covariance and the SCMEVM with an inferred graphical structure. The inferred graphical structure, obtained from Algorithm 3.5 with  $\rho \in \{0.45, \dots, 0.5\}$ , is shown in Figure 6 (right panel). This graph has 145 edges compared to the maximum possible 465 edges. Lastly, we simulate datasets from the fitted models using Algorithm 3.6 with  $N = 20n$  and  $u = u_{Y_i}$ .

Bootstrapped estimates of the coefficient of tail dependence  $\eta_{i,j}(u)$  for  $i, j \in V$ ,  $i > j$  and  $u \in \{0.8, 0.85, 0.9\}$  are obtained using 200 bootstrapped samples of the data. For each bootstrapped data set, both empirical and model-based estimates of  $\eta_{i,j}(u)$  are obtained. The point estimates in Figure 7 are obtained by taking the medians of the two sets of estimates. The SCMEVMs describe the empirical dependence better than the EHM for both flow-connected (triangles) and flow-unconnected (circles) stations, and across all values of  $u$ . This highlights the value of a model that captures a range of extremal dependence classes. Figure 7 shows that all pairs of stations appear to exhibit AI with positive association,  $\eta(u) \in (0.5, 1)$ , while analogous plots of  $\chi(u)$  (Supplementary Material, Farrell et al. (2024)) imply all pairs have AD. However, for stations with weaker (stronger) extremal dependence, the two measures decrease (stay close to 1) as  $u$  increases. This supports the plausible conclusion that some pairs of stations, particularly those that are flow-unconnected, exhibit AI while others, particularly those that are flow-connected, exhibit AD.

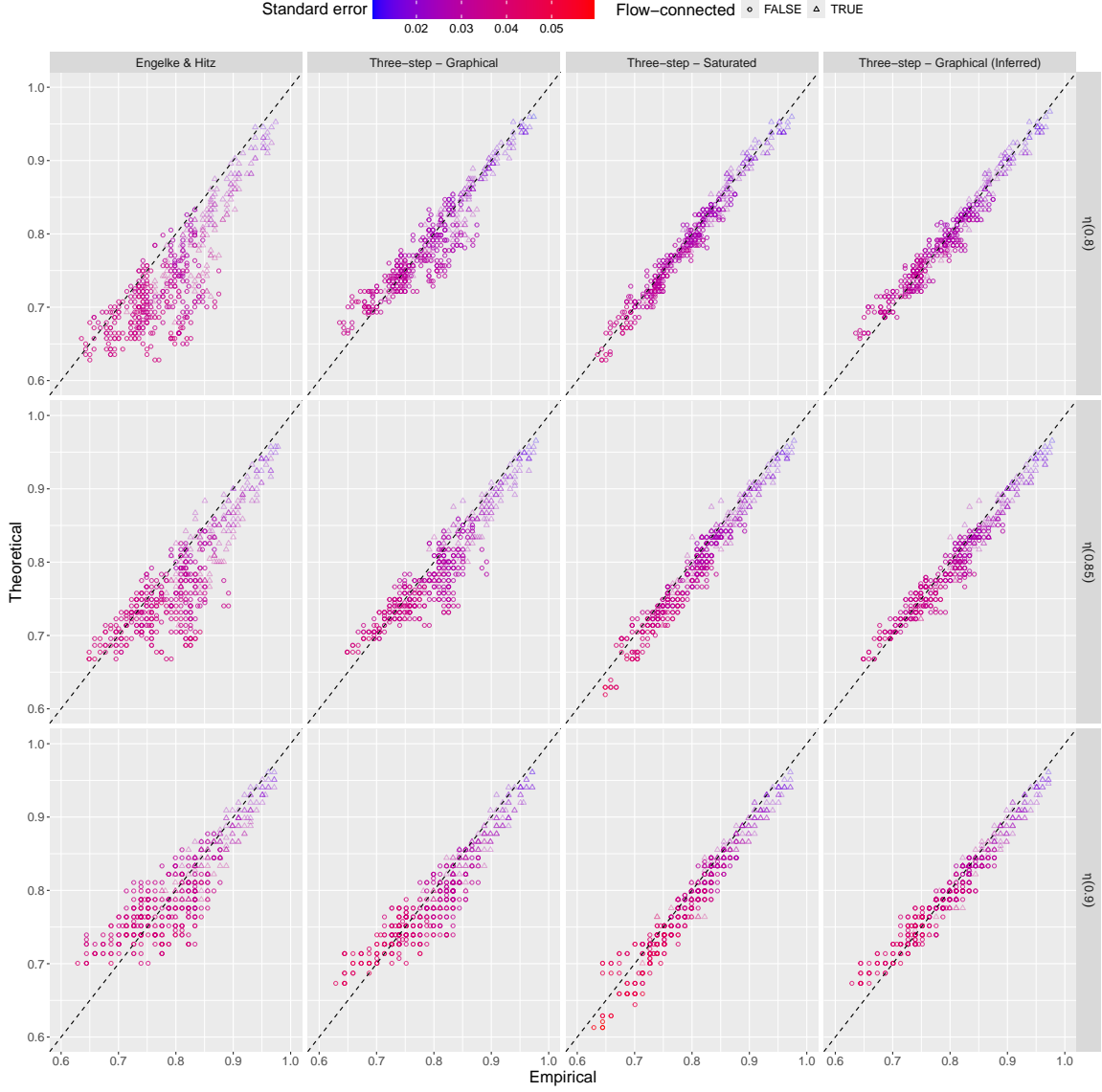


Figure 7: Empirical and model-based estimates of  $\eta_{i,j}(u)$  for  $u \in \{0.8, 0.85, 0.9\}$  (top to bottom), and  $i, j \in V$  but  $i > j$ . Model-based estimates use the EHM (an AD based model) (left) and the three-step SCMEVM (an AI based model) with graphical covariance (centre left), with structure given in Figure 1 (left panel), the three-step SCMEVM with saturated covariance (centre right) and graphical covariance (right) with structure given in Figure 6 (right panel). Black dashed lines show  $y = x$ . Circles (triangles) show flow-connected (flow-unconnected). The colour shows the standard error of the model-based estimates.

For  $u = 0.8$ , the SCMEVM with saturated covariance performs noticeably better than the graphical SCMEVM with structure given by the undirected tree induced by the flow connections. This suggests that the extremal dependence is influenced by factors beyond the river structure (see also Asadi et al. (2015)). To support this hypothesis, Figure 8 shows the difference in the empirical and model-based estimates of  $\eta_{i,j}(0.8)$  for each pair  $i, j \in V$  where the

model-based estimates are from the SCMEVM with graphical covariance using the induced undirected tree. We observe that underestimation predominantly occurs for flow-unconnected stations. For example, the dependence between stations 11-12 and 16-22 is considerably underestimated. While these two sets of stations are flow-unconnected, the sources of their tributaries are geographically close and at similar altitudes; hence, stronger dependence than suggested by the lack of flow connection is not unexpected. Similar observations are made when comparing the Isar (stations 14 - 19) and Salzach (stations 28 - 31) tributaries, as well as stations 23 - 24 and 25 - 27. Furthermore, the inferred graphical structure in Figure 6 (right panel) shows many connections between sites on geographically neighbouring tributaries. Indeed, using the inferred graphical structure in the SCMEVM drastically improves the model fit (Figure 7, right panel), and resolves the systematic underestimation caused by using a saturated covariance structure.

Returning to Figure 7, we observe that the SCMEVMs do underestimate dependence at higher thresholds, particularly for flow-unconnected stations with weaker associations. In contrast, the EHM becomes less biased as the threshold increases, although its bias at lower thresholds is greater than the bias in the SCMEVMs at higher thresholds. Moreover, particularly for stations with weaker associations, the cross-site variability in the model-based estimates is much higher for the EHM than the SCMEVMs, regardless of level. In conclusion, the SCMEVMs represent the extremal dependence in the data more accurately and consistently than the EHM.

## 6 Discussion

In this paper, we have extended the conditional multivariate extreme value model (Heffernan and Tawn, 2004) by replacing the non-parametric residual distribution with a flexible and fully parametric model, overcoming the curse of dimensionality that arises when extrapolating from a non-parametric estimate of a high-dimensional distribution. Our proposed parametric model is the MVAGG distribution. The copula-based construction of the MVAGG, which combines asymmetric generalised Gaussian margins with a multivariate Gaussian dependence structure, facilitates efficient statistical inference, as the margins and dependence structures can be inferred separately in a stepwise manner. Furthermore, graphical structures can be incorporated into the covariance matrix of the multivariate Gaussian distribution in a mathematically tractable way. This provides a simple method to infer the structure if it is not already known, as well as a mechanism to induce sparsity into the dependence structure. Consequently, the model is more flexible than the spatial model of Richards et al. (2022); Wadsworth and Tawn (2022), who take a similar copula-based approach but with symmetric

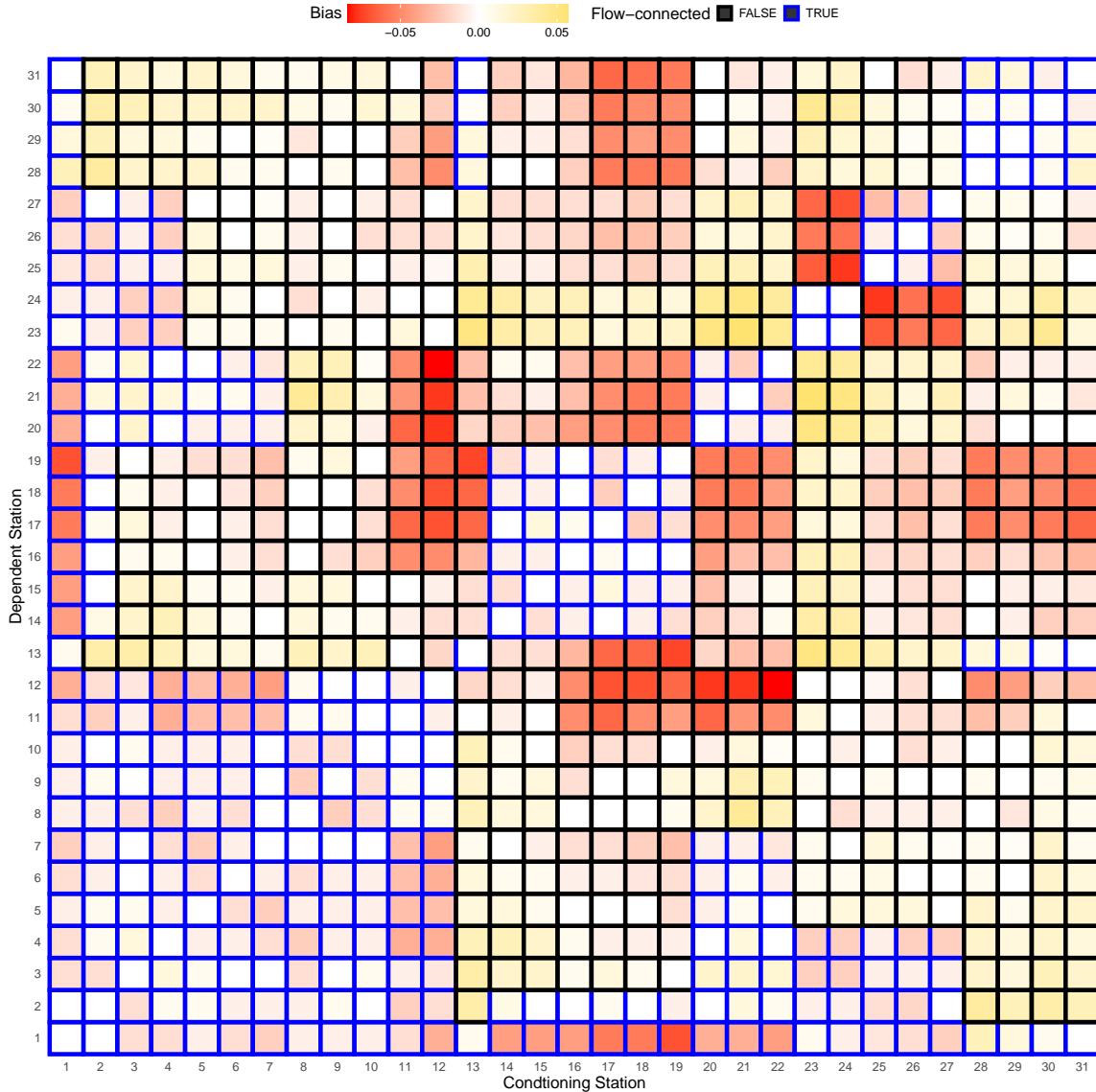


Figure 8: Difference between empirical and median of model-based estimates of  $\eta_{i,j}(0.8)$  for each  $i, j \in V$  for the SCMEVM with a graphical covariance, where the graphical structure is assumed to be the undirected tree induced by the flow connections in Figure 1 (left panel). Under- and over-estimation by the model are represented by red and gold squares, respectively. Flow-connected and flow-unconnected stations are represented by blue and black borders, respectively.

generalised Gaussian margins and a distance-based kernel.

A repercussion of the flexibility of the proposed model is that it has a large parameter space. Separate estimation of the marginal and dependence parameters for the residual distribution is found to be computationally more efficient than joint estimation of all parameters and results in no loss of information.

Nevertheless, despite the sparsity induced by using a graphical structure to model the covariance matrix, fitting this model is more computationally expensive than fitting a model with a saturated covariance structure, since the likelihood for the former must be optimised numerically. Therefore, while graphical structures can be learned and implemented by our model, the model in its current form may not be suitable for very large dimensions. Future work should investigate ways in which the model can be adapted to address this computational hurdle. One approach could be to incorporate factorisation of the residual density using the pairwise Markov structure implied by the graph (Casey and Papastathopoulos, 2023; Engelke and Hitz, 2020). However, this limits the permissible graphical structures to decomposable graphs (Engelke and Hitz, 2020) or chordal graphs where the separator sets are singletons (Casey and Papastathopoulos, 2023).

Our analysis of the upper Danube River basin raises some interesting questions. Firstly, our model captures the dependence between stations more effectively than the multivariate graphical extremes model of Engelke and Hitz (2020), highlighting the need for a flexible model that can capture both AD and AI. However, the implementation of the model using the undirected tree induced by the flow connections of the river network fails to fully capture the extremal dependence in the river discharges. Improved predictions can be obtained either by using the inferred graphical structure or by assuming a saturated covariance matrix. One possible solution to this might be to add a second covariance matrix incorporating geographical spatial structure (Asadi et al., 2015), into the residual distribution of the SCMEVM.

Finally, as with the graphical extremes model of Engelke and Hitz (2020), our model only allows predictions at measured locations. Parameterising the Gaussian copula kernel with a Matérn or Whittle-Matérn correlation function, where distance is defined as the distance along the graph (Bolin et al., 2024), would allow extrapolation to unobserved locations. The generally strong correspondence between the empirical and model-based estimates of  $\eta$  for the flow-connected sites from the SCMEVM gives us confidence that such a model would extrapolate accurately.

## Declarations

### Funding

Aiden Farrell was supported by the Engineering and Physical Sciences Research Council (EPSRC) grant EP/W523811/1.

## Code

Code that supports our findings can be found in the AidenFarrell/Graphical\_Conditional\_Extremes repository on GitHub.

## References

- Asadi, P., Davison, A. C., and Engelke, S. (2015). Extremes on river networks. *The Annals of Applied Statistics*, 9(4):2023 – 2050.
- Blanchet, J. and Davison, A. C. (2011). Spatial modeling of extreme snow depth. *The Annals of Applied Statistics*, 5(3):1699–1725.
- Bolin, D., Simas, A. B., and Wallin, J. (2024). Gaussian Whittle–Matérn fields on metric graphs. *Bernoulli*, 30(2):1611 – 1639.
- Casey, A. and Papastathopoulos, I. (2023). Decomposable Tail Graphical Models. *arXiv preprint arXiv:2302.05182*.
- Davis, R. A., Klüppelberg, C., and Steinkohl, C. (2013). Max-stable processes for modeling extremes observed in space and time. *Journal of the Korean Statistical Society*, 42(3):399–414.
- de Fondeville, R. and Davison, A. C. (2018). High-dimensional peaks-over-threshold inference. *Biometrika*, 105(3):575–592.
- Debushe, L. K. and Diriba, T. A. (2021). Conditional modelling approach to multivariate extreme value distributions: application to extreme rainfall events in south africa. *Environmental and Ecological Statistics*, 28(3):469–501.
- Engelke, S., Hentschel, M., Lalancette, M., and Röttger, F. (2024a). Graphical models for multivariate extremes. *arXiv preprint arXiv:2402.02187*.
- Engelke, S. and Hitz, A. S. (2020). Graphical models for extremes. *Journal of the Royal Statistical Society: Series B (Statistical Methodology)*, 82(4):871–932.
- Engelke, S., Hitz, A. S., Gnecco, N., and Hentschel, M. (2024b). *graphicalExtremes: Statistical Methodology for Graphical Extreme Value Models*. R package version 0.3.2.
- Engelke, S., Malinowski, A., Kabluchko, Z., and Schlather, M. (2015). Estimation of Hüsler–Reiss distributions and Brown–Resnick processes. *Journal of the Royal Statistical Society Series B: Statistical Methodology*, 77(1):239–265.

- Farrell, A., Eastoe, E. F., and Lee, C. (2024). Supplement to “Conditional Extremes with Graphical Models”.
- Ferreira, A. and de Haan, L. (2014). The generalized Pareto process; with a view towards application and simulation. *Bernoulli*, 20(4):1717 – 1737.
- Friedman, J., Hastie, T., and Tibshirani, R. (2007). Sparse inverse covariance estimation with the graphical lasso. *Biostatistics*, 9(3):432–441.
- Friedman, J., Hastie, T., and Tibshirani, R. (2019). *glasso: Graphical Lasso: Estimation of Gaussian Graphical Models*. R package version 1.11.
- Gouldby, B., Méndez, F., Guanche, Y., Rueda, A., and Mínguez, R. (2014). A methodology for deriving extreme nearshore sea conditions for structural design and flood risk analysis. *Coastal Engineering*, 88:15–26.
- Gouldby, B., Wyncoll, D., Panzeri, M., Franklin, M., Hunt, T., Hames, D., Tozer, N., Hawkes, P., Dornbusch, U., and Pullen, T. (2017). Multivariate extreme value modelling of sea conditions around the coast of england. *Proceedings of the Institution of Civil Engineers - Maritime Engineering*, 170(1):3–20.
- Heffernan, J. E. and Resnick, S. I. (2007). Limit laws for random vectors with an extreme component. *The Annals of Applied Probability*, 17(2):537 – 571.
- Heffernan, J. E. and Tawn, J. A. (2004). A conditional approach for multivariate extreme values (with discussion). *Journal of the Royal Statistical Society: Series B (Statistical Methodology)*, 66(3):497–546. 6
- Huser, R. and Davison, A. C. (2014). Space—time modelling of extreme events. *Journal of the Royal Statistical Society. Series B (Statistical Methodology)*, 76(2):439–461.
- Keef, C., Papastathopoulos, I., and Tawn, J. A. (2013). Estimation of the conditional distribution of a multivariate variable given that one of its components is large: Additional constraints for the Heffernan and Tawn model. *Journal of Multivariate Analysis*, 115:396–404.
- Ledford, A. W. and Tawn, J. A. (1996). Statistics for near independence in multivariate extreme values. *Biometrika*, 83(1):169–187.
- Ledford, A. W. and Tawn, J. A. (1997). Modelling dependence within joint tail regions. *Journal of the Royal Statistical Society: Series B (Statistical Methodology)*, 59(2):475–499.

- Murphy, C., Tawn, J. A., and Varty, Z. (2024). Automated threshold selection and associated inference uncertainty for univariate extremes. *Technometrics*, 0(ja):1–17.
- Nacereddine, N. and Goumeidane, A. B. (2019). Asymmetric Generalized Gaussian Distribution Parameters Estimation based on Maximum Likelihood, Moments and Entropy. In *2019 IEEE 15th International Conference on Intelligent Computer Communication and Processing (ICCP)*, pages 343–350.
- Nagler, T. and Czado, C. (2016). Evading the curse of dimensionality in nonparametric density estimation with simplified vine copulas. *Journal of Multivariate Analysis*, 151:69–89.
- Neal, J., Keef, C., Bates, P., Beven, K., and Leedal, D. (2013). Probabilistic flood risk mapping including spatial dependence. *Hydrological Processes*, 27(9):1349–1363.
- Oesting, M. and Stein, A. (2018). Spatial modeling of drought events using max-stable processes. *Stochastic environmental research and risk assessment*, 32:63–81.
- Opitz, T., Huser, R., Bakka, H., and Rue, H. (2018). INLA goes extreme: Bayesian tail regression for the estimation of high spatio-temporal quantiles. *Extremes*, 21(3):441–462.
- R Core Team (2024). *R: A Language and Environment for Statistical Computing*. R Foundation for Statistical Computing, Vienna, Austria.
- Ramos, A. and Ledford, A. (2011). An alternative point process framework for modeling multivariate extreme values. *Communications in Statistics-Theory and Methods*, 40(12):2205–2224.
- Reich, B. J. and Shaby, B. A. (2012). A hierarchical max-stable spatial model for extreme precipitation. *The Annals of Applied Statistics*, 6(4):1430 – 1451.
- Ribatet, M. (2013). Spatial extremes: Max-stable processes at work. *Journal de la Société Française de Statistique*, 154(2):156–177.
- Richards, J., Tawn, J. A., and Brown, S. (2022). Modelling extremes of spatial aggregates of precipitation using conditional methods. *The Annals of Applied Statistics*, 16(4):2693 – 2713.
- Rootzén, H. and Tajvidi, N. (2006). Multivariate generalized Pareto distributions. *Bernoulli*, 12(5):917–930.
- Rootzén, H., Segers, J., and Wadsworth, J. L. (2018). Multivariate generalized Pareto dis-

- tributions: Parametrizations, representations, and properties. *Journal of Multivariate Analysis*, 165:117–131.
- Ross, E., Astrup, O. C., Bitner-Gregersen, E., Bunn, N., Feld, G., Gouldby, B., Huseby, A., Liu, Y., Randell, D., Vanem, E., and Jonathan, P. (2020). On environmental contours for marine and coastal design. *Ocean Engineering*, 195:106194.
- Schlather, M. (2002). Models for stationary max-stable random fields. *Extremes*, 5:33–44.
- Shooter, R., Ross, E., Ribal, A., Young, I. R., and Jonathan, P. (2021). Spatial dependence of extreme seas in the North East Atlantic from satellite altimeter measurements. *Environmetrics*, 32(4):e2674.
- Shooter, R., Ross, E., Tawn, J., and Jonathan, P. (2019). On spatial conditional extremes for ocean storm severity. *Environmetrics*, 30(6):e2562.
- Simpson, E. S. and Wadsworth, J. L. (2021). Conditional modelling of spatio-temporal extremes for Red Sea surface temperatures. *Spatial Statistics*, 41:100482.
- Simpson, E. S., Wadsworth, J. L., and Tawn, J. A. (2020). Determining the dependence structure of multivariate extremes. *Biometrika*, 107(3):513–532.
- Sklar, M. (1959). Fonctions de répartition à  $n$  dimensions et leurs marges. In *Annales de l'ISUP*, volume 8, pages 229–231.
- Smith, R. L. (1990). Max-stable processes and spatial extremes. *Unpublished manuscript*, 205:1–32.
- Smith, R. L., Tawn, J. A., and Coles, S. G. (1997). Markov chain models for threshold exceedances. *Biometrika*, 84(2):249–268.
- Southworth, H., Heffernan, J. E., and Metcalfe, P. D. (2024). *texmex: Statistical modelling of extreme values*. R package version 2.4.9.
- Speed, T. P. and Kiiveri, H. T. (1986). Gaussian Markov Distributions over Finite Graphs. *The Annals of Statistics*, 14(1):138 – 150.
- Stephenson, A. G., Shaby, B. A., Reich, B. J., and Sullivan, A. L. (2015). Estimating spatially varying severity thresholds of a forest fire danger rating system using max-stable extreme-event modeling. *Journal of Applied Meteorology and Climatology*, 54(2):395–407.
- Towe, R., Tawn, J., Lamb, R., and Sherlock, C. (2019). Model-based inference of conditional extreme value distributions with hydrological applications. *Environmetrics*, 30(8):e2575.

- Wadsworth, J. and Tawn, J. (2013). A new representation for multivariate tail probabilities. *Bernoulli*, 19(5B):2689 – 2714.
- Wadsworth, J. and Tawn, J. (2022). Higher-dimensional spatial extremes via single-site conditioning. *Spatial Statistics*, 51:100677. 9
- Westra, S. and Sisson, S. A. (2011). Detection of non-stationarity in precipitation extremes using a max-stable process model. *Journal of Hydrology*, 406(1-2):119–128.
- Winter, H. C. and Tawn, J. A. (2016). Modelling heatwaves in central france: a case-study in extremal dependence. *Journal of the Royal Statistical Society Series C: Applied Statistics*, 65(3):345–365.
- Winter, H. C. and Tawn, J. A. (2017).  $k$ th-order Markov extremal models for assessing heatwave risks. *Extremes*, 20:393–415.

# Supplementary Material to “Conditional Extremes with Graphical Models”

## S.1 Prediction from the conditional multivariate extreme value model

The original conditional multivariate extreme value model (CMEVM) uses a semi-parametric algorithm for prediction to avoid over-reliance on the working distributional assumptions used for parameter estimation (see Section 2.1 of the main text). Specifically, prediction is performed by non-parametrically sampling with replacement from the empirical distribution of the fitted residuals. Such sampling suffers from the curse of the dimensionality (Nagler and Czado, 2016), meaning the predictive performance of the CMEVM decreases as the dimension increase. To demonstrate this, we perform a simple simulation study and compare the predictive performance of the CMEVM to the structured CMEVM (SCMEVM) proposed in Section 2 of the main text.

Consider a simple undirected graph  $\mathcal{G} = (V, E)$  with vertex set  $V = \{1, \dots, d\}$  and edge set  $E \subseteq \{\{j, k\} \mid j, k \in V, j \neq k\}$  with  $\{j, k\} \in E$  if and only if  $\{k, j\} \in E$ . We set  $d = 20$  and randomly select the edges in the graph such that the number of edges is approximately 20% of the number of edges in the full graph. We simulate 200 datasets of size 250 for  $Y \mid Y_i > u_{Y_i}$  as per Section 4.1 of the main text i.e., we simulate  $Y_i \mid Y_i > u_{Y_i}$  from a standard exponential distribution and obtain  $Y_i \mid Y_i > u_{Y_i}$  using equation (2.3) of the main text with  $Z_i$  simulated from a multivariate asymmetric generalised Gaussian (MVAGG) distribution (Section 2.2 of the main text). We set the dependence threshold  $u_{Y_i}$  to the 0.8-quantile of the standard Laplace distribution. True dependence and asymmetric generalised Gaussian (AGG) parameters are independently sampled from uniform distributions on  $(0.1, 0.3)$  for  $\alpha_j$ ,  $(0.1, 0.2)$  for  $\beta_j$ ,  $(-1, 1)$  for  $\nu_j$ ,  $(0.5, 1)$  for  $\kappa_{1j}$ ,  $(1.5, 2)$  for  $\kappa_{2j}$ , and  $(0.8, 2.5)$  for  $\delta_j$ , for each  $j \in V$ .

For computational purposes, we consider a single conditioning component  $i$  selected at random from  $V$ ; similar results can be obtained when conditioning on different components. Predictive performance is assessed on Laplace margins only since the probability integral transform (PIT) used to back-transform to the original margins does not alter the dependence structure. For each data set, we fit the (i) CMEVM, (ii) three-step SCMEVM with graphical covariance structure, and (iii) three-step SCMEVM with saturated covariance. For (ii), the graph is assumed to be known and correctly specified above. For prediction, we used datasets of size  $5 \times 10^6$  for  $Y \mid Y_i > u_{Y_i}$  simulated from the fitted models using the methods

described in Section 4.4 of Heffernan and Tawn (2004) for (i) and Algorithm 1 in Section 5.1 of Wadsworth and Tawn (2022) for (ii) and (iii).

Figure S1 shows  $\mathbb{P}[Y_A > v \mid Y_i > v]$ , on the exponential scale, for 500 different sets  $A \subseteq V_i = V \setminus \{i\}$  such that  $|A| = 3$ ; the sets were chosen at random. We set  $v$  to be the 0.999-quantile of the standard Laplace distribution which would approximately correspond to a 1 in 10 year event if we had daily data. The truth is obtained empirically using a single sample of size  $10^7$  from the true distribution, while the model-based estimates are the median of the model-based point estimates from each of the 200 samples. The CMEVM consistently underestimates the probabilities, whereas the SCMEVMs perform much better, particularly for those probabilities that are very close to 0. The standard error of the model-based estimates (on the original scale), appear to be lower for the SCMEVMs compared to the CMEVM. The SCMEVMs do slightly underestimate the probabilities, however, we anticipate this could be resolved by increasing the size of the prediction datasets.

The CMEVM underestimates the probabilities because it allows neither interpolation nor extrapolation of the fitted residuals, resulting in “rays” in data simulated from the fitted model. This can be seen in Figure S2 which shows 2,000 randomly selected points from data simulated from the fitted models for (i) and (ii). Data used to fit the models is also shown. The CMEVM does not accurately capture dependence between components 2 and 13, but the SCMEVM does much better. This pattern will only be exacerbated as the dimension increases. Therefore, the predictive power of the CMEVM will diminish as (1)  $v$  approaches the upper end-point of the distribution, (2) the size of set  $A$  increases, and (3) the dimension of the problem increases. The SCMEVM overcomes such limitations by using a flexible, fully parametric distribution for the residuals.

## S.2 Marginal distributions for the residuals

In Section 2.2 of the main text we propose an adaptation of the generalised Gaussian model used by Wadsworth and Tawn (2022). Here we show that the proposed alternative, the asymmetric generalised Gaussian, improves the overall model fit, particularly for random variables with asymptotic independence. For  $d = 20$  and a graph  $\mathcal{G} = (V, E)$  with edges randomly selected such that the number of edges is approximately 20% of the number of edges in the full graph, we simulate 200 datasets of size 5000 from a multivariate Gaussian (MVG) distribution with mean vector  $\boldsymbol{\mu}$  and correlation matrix  $\Sigma$ . The components  $\mu_j$  are independently sampled from a uniform distribution on  $(-5, 5)$ , and the correlation matrix is associated with  $\mathcal{G}$ . For each replicate  $X$ , we transform the margins onto standard Laplace

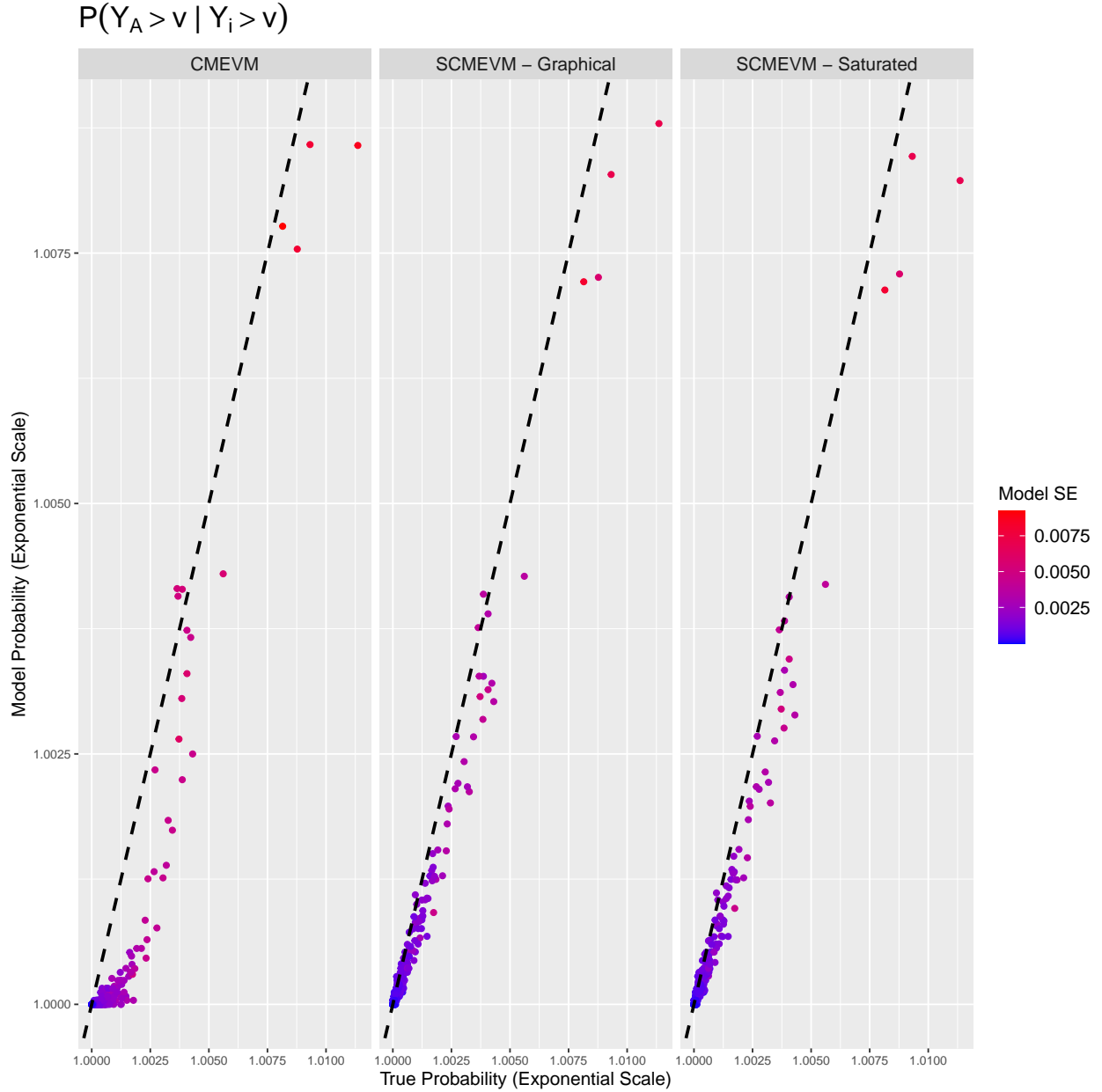


Figure S1: Empirical and model-based estimates of  $\mathbb{P}[Y_A > v \mid Y_i > v]$  for a randomly selected component  $i \in V$ , 500 randomly selected sets  $A \subseteq V_i$  such that  $|A| = 3$ , and  $v$  is the 0.999-quantile of the standard Laplace distribution. Model-based estimates use the CMEVM (left), the three-step SCMEVM with graphical covariance (centre) with structure described in Section S.1, and the three-step SCMEVM with saturated covariance (right). The colour shows the standard error of the model-based estimates. Black dashed lines show the  $y = x$ .

margins  $Y$ , as per Section 3.1 of the main text, before fitting the SCMEVM. We set the dependence thresholds  $u_{Y_i}$  to the 0.90-quantile of the standard Laplace distribution.

To fit the SCMEVM we use the three-step model (Algorithm 3.4 of the main text) and assume

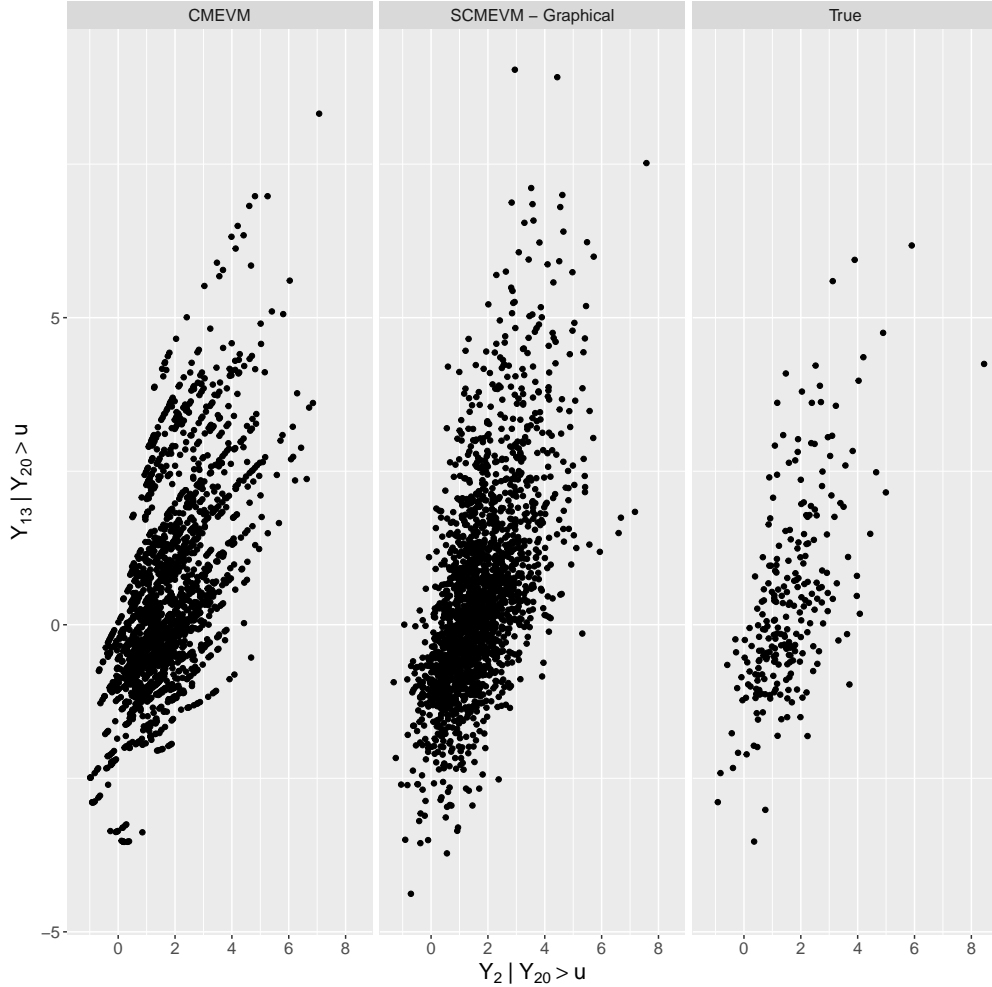


Figure S2: Scatter plots for  $Y_2$  and  $Y_{13}$  given  $Y_{20} > u_{Y_{20}}$ . The points correspond to 2,000 randomly selected data points from a sample of size  $5 \times 10^6$  simulated from the fitted model for the CMEVM (left), and the three-step SCMEVM with graphical covariance (centre) with structure described in Section S.1. Also shown are the 250 points used to fit the models (right).

a saturated covariance structure. For comparison, we fit the same model but with generalised Gaussian margins for the residual distribution. We then simulate samples of size  $N = 20n$  from each of the conditional models (see Section 3.3 of the main text for the simulation algorithm). Figure S3 compares the median of the empirical and model-based estimates of  $\eta_{i,j}(u)$  for  $i, j \in V, i > j$  and  $u \in \{0.95, 0.99\}$  over the 200 datasets. The only difference between the left and right panels is the margins used in the residual distribution, which are AGG and generalised Gaussian, respectively. The generalised Gaussian under-estimates the true value of  $\eta$ , particularly for the pairs with weaker dependence. In contrast, the AGG tends to capture  $\eta$  reasonably well with no increase in the standard error despite the additional model parameter. Therefore, the AGG is necessary to obtain accurate predictions from the

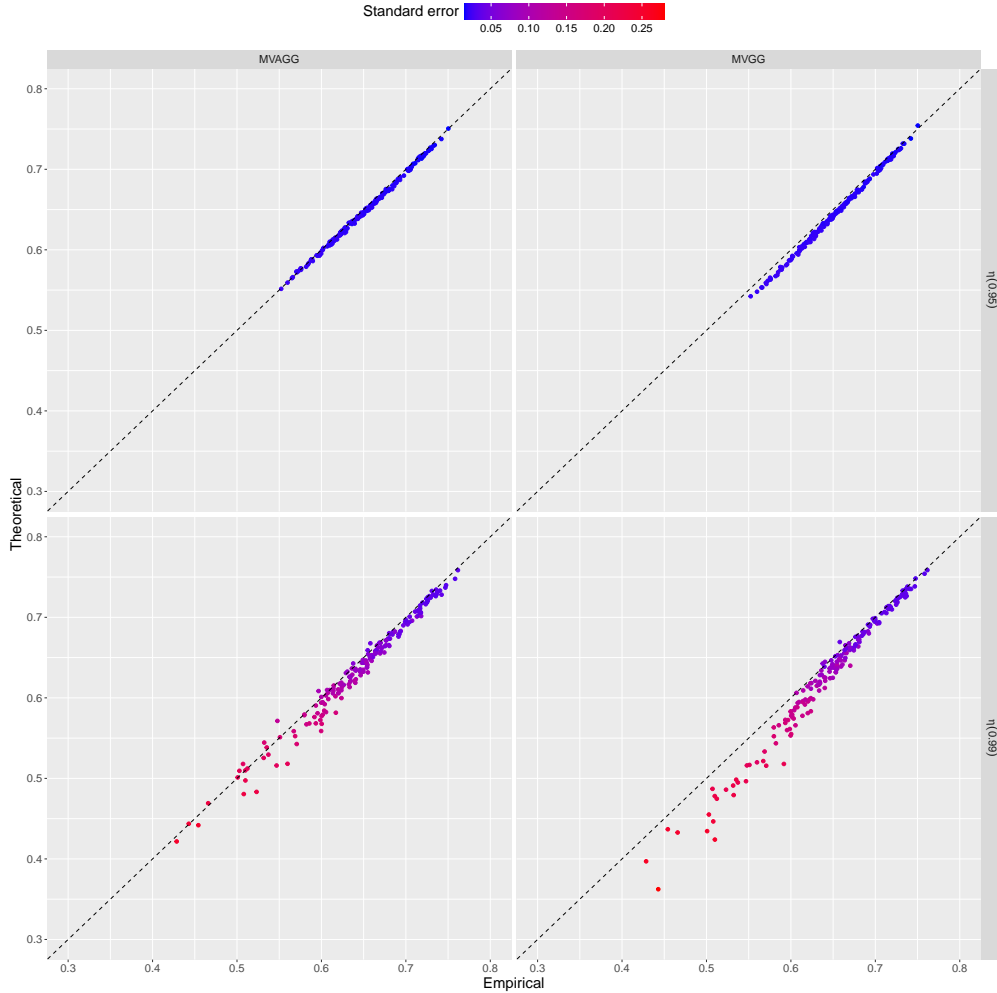


Figure S3: Empirical and model-based estimates of  $\eta_{i,j}(u)$  for  $u \in \{0.95, 0.99\}$  (top to bottom), and  $i > j \in V$ . Model-based estimates use the three-step SCMEVM with residuals having a saturated covariance and either asymmetric generalised Gaussian (left) and generalised Gaussian (right) margins. Black dashed lines show  $y = x$ . The colour shows the standard error of the model-based estimates.

model.

### S.3 Additional figures and simulation studies for Section 4.1

Section S.3.1 contains additional figures for the simulation study of Section 4.1 in the main text. Also shown are two additional simulation studies to assess the model performance in the presence of either strong positive (Section S.3.2) or weak negative (Section S.3.3) associations. Throughout this section, data are simulated from the SCMEVM

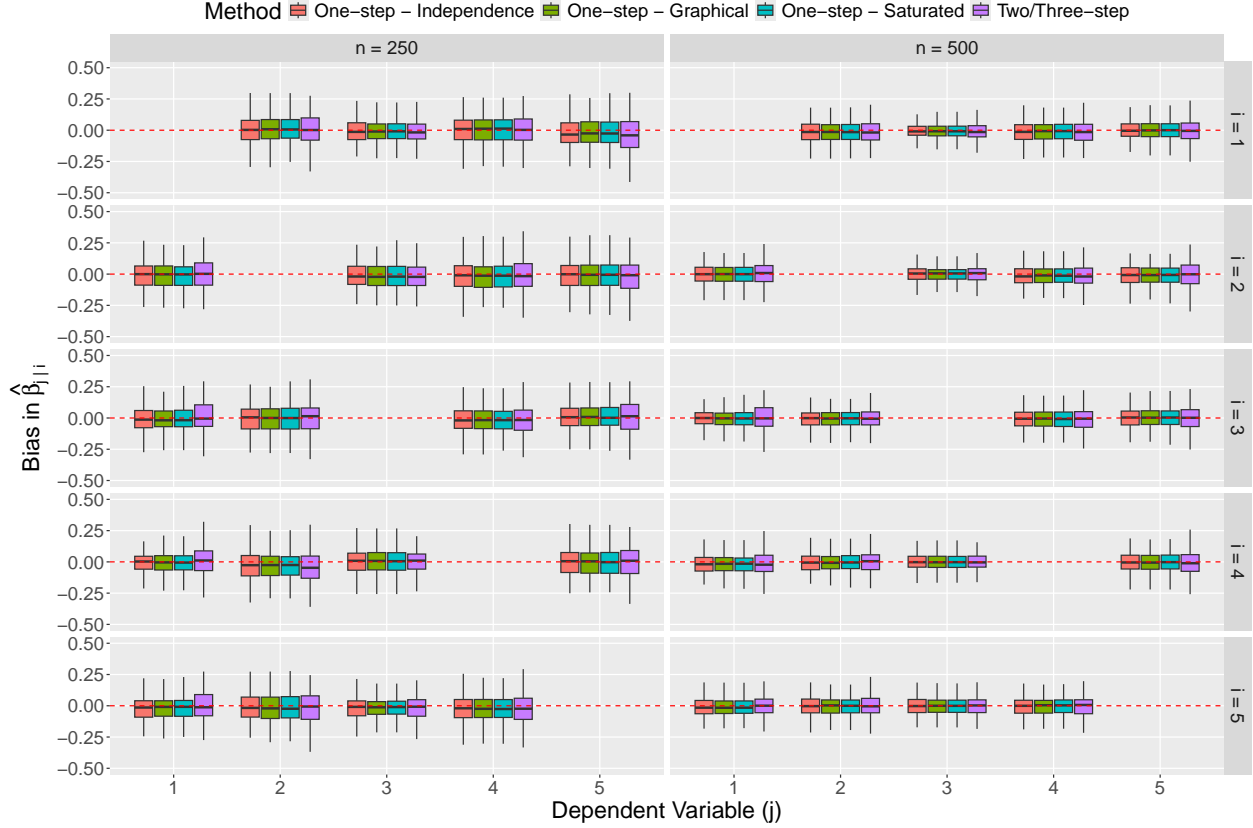


Figure S4: Boxplots detailing the bias of  $\hat{\beta}_{j|i}$  for distinct  $i, j \in V$ . Each row corresponds to the conditioning variable  $i$ , and each column corresponds to the sample size. The different models are denoted by the fill of the boxplots. Red dashed lines show  $y = 0$ .

with a graphical covariance structure given by  $\mathcal{G} = (V, E)$ ,  $V = \{1, \dots, 5\}$ , and  $E = \{\{1, 2\}, \{1, 3\}, \{2, 3\}, \{3, 4\}, \{3, 5\}, \{4, 5\}\}$ .

### S.3.1 Weak positive dependence

For this study, recall that the true dependence and AGG parameters were selected at random by sampling from a uniform distribution on  $(0.1, 0.5)$  for  $\alpha_j$ ,  $(0.1, 0.3)$  for  $\beta_j$ ,  $(-5, 5)$  for  $\nu_j$ ,  $(0.5, 2)$  for  $\kappa_{1j}$ ,  $(1.5, 3)$  for  $\kappa_{2j}$ , and  $(0.8, 2.5)$  for  $\delta_j$ , for each  $j \in V$ . Figures S4, S5 and S6 show the bias in  $\hat{\beta}_{j|i}$ , the AGG parameters, and  $\hat{\Gamma}_{j|i}$  respectively. Similar to the plot for  $\hat{\alpha}_{j|i}$  in the main text, we omit the maximum likelihood estimates (MLEs) from the stepwise methods in cases where they are, by construction, identical to estimates that are already presented. For  $\hat{\Gamma}_{j|i}$  we exclude those models that assume independent residuals since these are consistently biased. The findings are very similar to the main text: all models are unbiased across all parameters; the two- and three-step methods show slightly more cross-sample variability in their bias; variability in bias decreases as sample size increases.

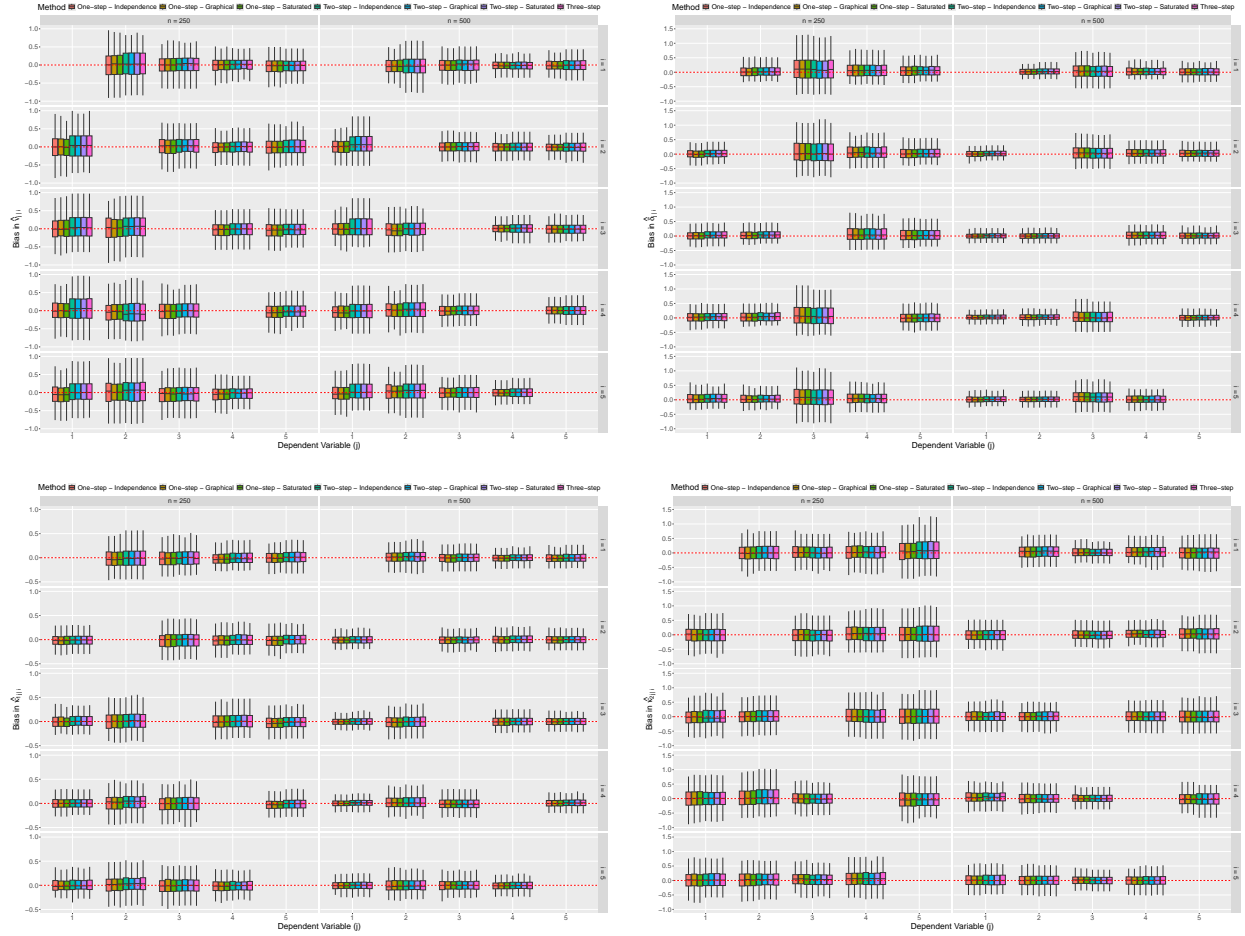


Figure S5: Boxplots detailing the bias of  $\hat{\nu}_{j|i}$  (top left),  $\hat{\delta}_{j|i}$  (top right),  $\hat{\kappa}_{1j|i}$  (bottom left), and  $\hat{\kappa}_{2j|i}$  (bottom right) for distinct  $i, j \in V$ . Each row corresponds to the conditioning variable  $i$ , and each column corresponds to the sample size. The different models are denoted by the fill of the boxplots. Red dashed lines show  $y = 0$ .

### S.3.2 Strong positive dependence

We repeat the simulation study from Section 4.1 of the main text but with strong, positive correlations ( $> 0.48$ ). The other parameters remain unchanged from Section S.3.1. Boxplots of the parameter estimates (not included) are almost identical to what was seen with weak positive associations. To compare the three stepwise procedures, we compare the bias in the maximum log-likelihood values, see Table S3. The models with independent residuals are biased; this is expected because the dependence structure is clearly misspecified. The bias is lower in the case when we condition on component 3 because this results in exact independence between  $(W_1, W_2)$  and  $(W_4, W_5)$ . This result was not seen in the study from the main text due to the lower correlations used there. However, similarly to results shown in the main text, while models with a graphical or saturated dependence do exhibit a small

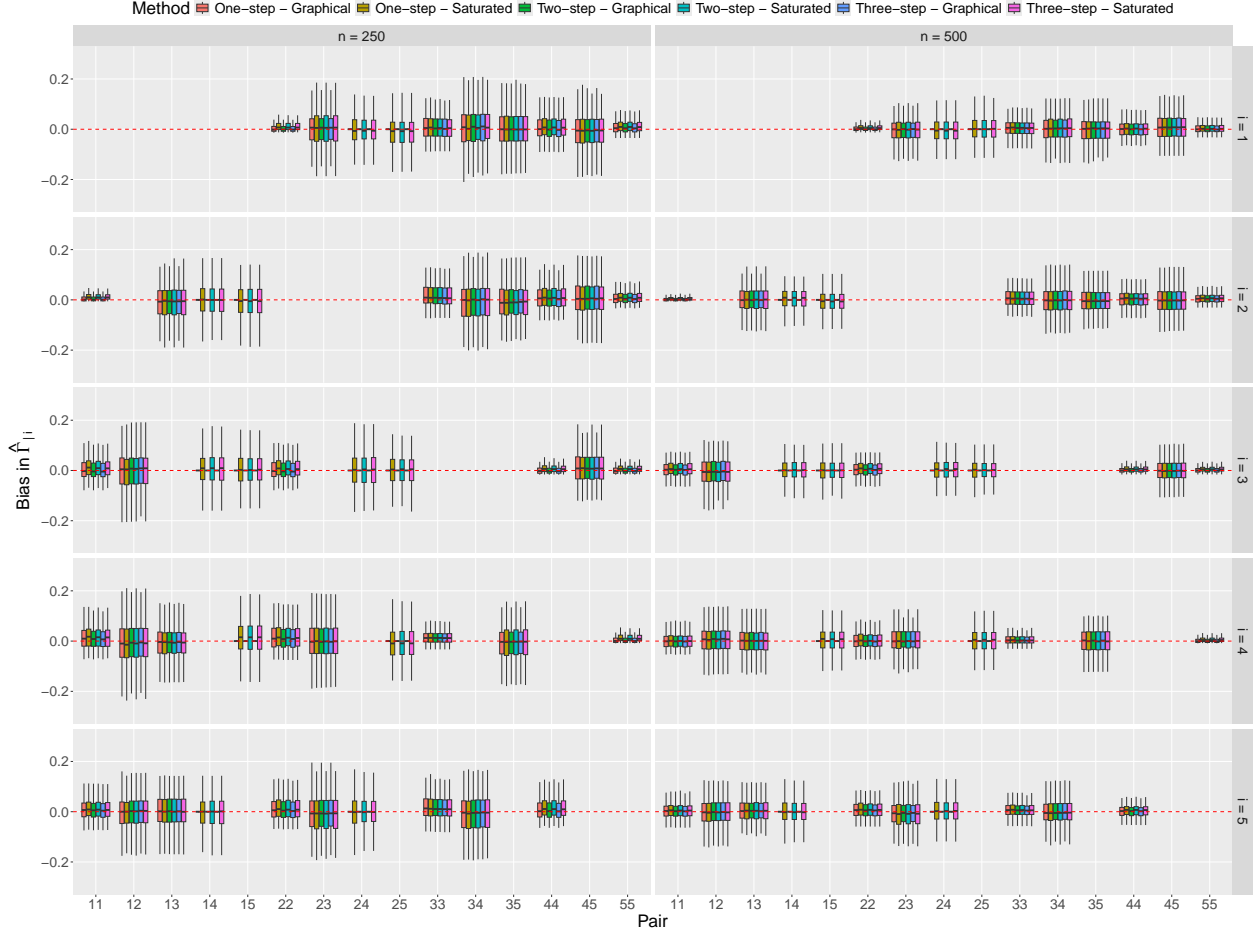


Figure S6: Boxplots for the bias of  $\hat{\Gamma}_i$  for each  $i \in V$ . Each row corresponds to the conditioning variable  $i$ , and each column corresponds to the sample size. The various models are denoted by the fill of the boxplots. Red dashed lines show  $y = 0$ .

positive bias, the magnitude of this similar across all stepwise procedures. This supports our claim that the stepwise inference procedures result in no loss of information. Further, when assuming that the residuals have a graphical or saturated dependence structure, the three-step model is least biased. Finally, the bias for the models with independent residuals increases with the sample size, whereas, the bias from the models with graphical and saturated covariance structures have a similar magnitude of bias for the larger sample size suggesting the latter models are more robust to changes in the sample size.

### S.3.3 Negative dependence

Similar to Section S.3.2, we repeat the simulation from Section 4.1 of the main text but with negative associations between some components. Equation (S.1) shows the true correlation

Table S3: Median (2.5% and 97.5% quantiles) bias in the fitted maximum log-likelihood values for data from the SCMEVM with strong positive associations. Bold values denote the least biased stepwise inference procedure for each covariance structure type and conditioning variable.

Covariance Structure		Independent			Graphical			Saturated		
Number of Excesses	Conditioning Variable	One-step	Two-step	Three-step	One-step	Two-step	Three-step	One-step	Two-step	Three-step
250	1	<b>-135.7 (-170.2, -98.9)</b>	-137.3 (-171.1, -99.6)	-137.3 (-171.1, -99.6)	14.7 (8.0, 22.5)	12.7 (6.1, 20.8)	<b>11.9 (5.2, 20.6)</b>	15.6 (8.4, 24.0)	13.5 (6.6, 22.1)	<b>12.8 (5.9, 21.4)</b>
	2	<b>-138.5 (-176.4, -100.0)</b>	-139.7 (-172.4, -101.3)	-139.7 (-172.4, -101.3)	14.5 (8.0, 23.0)	11.8 (4.7, 21.6)	<b>11.3 (4.1, 21.0)</b>	15.4 (9.1, 24.8)	12.8 (5.8, 23.2)	<b>12.1 (4.9, 22.3)</b>
	3	<b>-39.8 (-86.1, -18.7)</b>	-41.4 (-59.2, -20.4)	-41.4 (-59.2, -20.4)	13.3 (6.7, 22.8)	11.1 (4.3, 20.6)	<b>11.0 (4.1, 20.3)</b>	15.1 (7.8, 25.7)	13.2 (4.8, 23.6)	<b>13.1 (5.2, 23.2)</b>
	4	<b>-140.0 (-174.1, -94.0)</b>	-140.8 (-175.2, -96.7)	-140.8 (-175.3, -96.7)	14.1 (6.9, 22.9)	11.9 (4.7, 19.3)	<b>11.3 (4.2, 18.7)</b>	15.2 (8.3, 24.1)	12.9 (5.5, 20.6)	<b>12.2 (4.4, 20.2)</b>
	5	<b>-137.5 (-178.1, -105.5)</b>	-137.8 (-174.8, -106.5)	-137.8 (-174.8, -106.5)	14.0 (8.0, 22.6)	11.5 (3.2, 20.8)	<b>10.7 (2.8, 20.5)</b>	15.1 (8.9, 24.3)	12.5 (4.8, 22.1)	<b>11.8 (4.4, 21.7)</b>
500	1	<b>-280.2 (-326.7, -226.3)</b>	-281.9 (-327.7, -228.3)	-281.9 (-327.7, -228.3)	13.7 (7.6, 21.1)	11.9 (5.3, 19.2)	<b>11.2 (4.7, 18.3)</b>	14.7 (8.7, 22.2)	13.0 (6.2, 20.7)	<b>12.1 (5.6, 19.9)</b>
	2	<b>-286.9 (-332.7, -240.5)</b>	-289.0 (-333.7, -242.0)	-289.0 (-333.7, -242.0)	13.7 (7.7, 22.8)	11.0 (3.3, 19.5)	<b>10.5 (2.6, 18.7)</b>	14.7 (7.6, 24.1)	11.7 (3.8, 21.3)	<b>11.3 (3.1, 20.3)</b>
	3	<b>-95.3 (-126.8, -67.7)</b>	-97.1 (-123.7, -71.9)	-97.1 (-123.7, -71.9)	12.9 (7.1, 21.3)	10.3 (3.7, 18.7)	<b>10.1 (3.5, 18.3)</b>	14.8 (8.0, 23.4)	12.3 (4.5, 20.6)	<b>12.1 (4.9, 20.1)</b>
	4	<b>-282.0 (-332.8, -229.4)</b>	-283.7 (-333.4, -231.2)	-283.7 (-333.4, -231.2)	14.0 (8.5, 21.1)	11.4 (1.9, 19.2)	<b>10.9 (1.0, 18.7)</b>	14.9 (9.3, 23.6)	12.3 (4.0, 20.6)	<b>11.8 (1.2, 19.8)</b>
	5	<b>-286.3 (-342.2, -234.9)</b>	-286.9 (-338.3, -236.3)	-286.9 (-338.3, -236.3)	14.1 (7.4, 20.7)	11.3 (2.1, 18.4)	<b>10.7 (1.4, 17.6)</b>	14.9 (8.1, 22.3)	12.4 (4.2, 20.4)	<b>11.7 (2.8, 19.2)</b>

Table S4: Median (2.5% and 97.5% quantiles) bias in the fitted maximum log-likelihood values for data from the SCMEVM with weak negative associations. Bold values denote the least biased stepwise inference procedure for each covariance structure type and conditioning variable.

Covariance Structure		Independent			Graphical			Saturated		
Number of Excesses	Conditioning Variable	One-step	Two-step	Three-step	One-step	Two-step	Three-step	One-step	Two-step	Three-step
250	1	<b>-13.3 (-26.7, 1.0)</b>	-14.2 (-27.6, -0.4)	-14.2 (-27.6, -0.4)	13.9 (8.0, 22.7)	12.5 (6.1, 21.7)	<b>12.4 (6.0, 21.6)</b>	14.9 (8.1, 27.0)	13.2 (6.8, 24.8)	<b>13.1 (7.0, 24.8)</b>
	2	<b>-11.6 (-28.4, 3.8)</b>	-13.3 (-27.6, 1.3)	-13.3 (-27.6, 1.3)	14.6 (7.5, 23.4)	<b>12.6 (3.3, 20.6)</b>	12.7 (4.8, 21.4)	15.9 (7.6, 25.1)	<b>13.6 (4.6, 23.5)</b>	<b>13.6 (5.5, 23.1)</b>
	3	<b>-13.3 (-46.8, 2.3)</b>	-14.6 (-28.7, 2.5)	-14.6 (-28.7, 2.5)	13.6 (6.9, 23.4)	11.3 (4.6, 21.0)	<b>11.2 (4.6, 20.8)</b>	15.6 (8.1, 26.3)	13.1 (5.2, 23.9)	<b>13.0 (5.7, 23.7)</b>
	4	<b>-12.9 (-48.7, 1.6)</b>	-14.3 (-26.4, -0.2)	-14.3 (-26.4, -0.2)	13.8 (7.3, 21.9)	12.3 (5.4, 20.5)	<b>12.2 (5.9, 20.3)</b>	14.6 (5.1, 23.2)	13.0 (6.7, 21.6)	<b>12.9 (6.8, 21.6)</b>
	5	<b>-19.7 (-35.6, -4.7)</b>	-21.0 (-35.7, -5.7)	-21.0 (-35.7, -5.7)	13.6 (7.3, 21.9)	<b>12.0 (4.7, 20.2)</b>	<b>12.0 (4.9, 20.0)</b>	14.7 (8.1, 23.6)	13.1 (5.7, 22.3)	<b>13.0 (5.6, 22.1)</b>
500	1	<b>-37.6 (-59.8, -20.8)</b>	-38.8 (-61.0, -22.2)	-38.8 (-61.0, -22.2)	14.4 (8.9, 22.7)	12.9 (6.1, 20.8)	<b>12.8 (6.0, 20.7)</b>	15.1 (9.4, 23.2)	13.8 (6.9, 21.5)	<b>13.7 (6.8, 21.4)</b>
	2	<b>-34.9 (-57.8, -12.8)</b>	-36.9 (-59.3, -13.1)	-36.9 (-59.3, -13.1)	14.3 (7.7, 23.1)	12.3 (4.4, 21.7)	<b>12.2 (4.3, 21.5)</b>	15.1 (8.5, 24.0)	13.2 (5.4, 22.8)	<b>13.1 (5.3, 22.5)</b>
	3	<b>-33.8 (-51.9, -15.4)</b>	-35.4 (-54.2, -17.1)	-35.4 (-54.2, -17.1)	13.1 (6.9, 20.3)	10.7 (2.1, 18.6)	<b>10.6 (2.5, 18.5)</b>	14.8 (8.2, 23.0)	<b>12.3 (3.1, 20.3)</b>	<b>12.3 (3.0, 20.2)</b>
	4	<b>-40.5 (-57.8, -19.5)</b>	-41.7 (-59.7, -20.9)	-41.7 (-59.7, -20.9)	13.9 (8.2, 22.9)	11.9 (5.1, 20.6)	<b>11.7 (5.0, 20.5)</b>	14.7 (9.1, 24.1)	12.8 (5.4, 21.9)	<b>12.7 (5.4, 21.7)</b>
	5	<b>-51.2 (-70.9, -31.4)</b>	-52.8 (-70.6, -33.2)	-52.8 (-70.6, -33.2)	13.8 (8.5, 22.6)	12.0 (5.3, 21.3)	<b>11.9 (5.1, 20.9)</b>	14.5 (9.3, 23.9)	12.9 (6.4, 22.3)	<b>12.7 (6.2, 22.0)</b>

matrix. All other parameters remain unchanged from Section S.3.1.

$$\Sigma = \begin{bmatrix} 1.000 & -0.308 & -0.134 & 0.034 & 0.019 \\ -0.308 & 1.000 & -0.160 & 0.041 & 0.023 \\ -0.134 & -0.160 & 1.000 & -0.254 & -0.141 \\ 0.034 & 0.041 & -0.254 & 1.000 & -0.209 \\ 0.019 & 0.023 & -0.141 & -0.209 & 1.000 \end{bmatrix} \quad (\text{S.1})$$

Parameter estimates have been omitted as they were similar to those presented for the weak positive association example in the main text. To compare the stepwise inference procedures, Table S4 gives the biases of the fitted maximum log-likelihood values. As in the strong positive association study (Section S.3.2), models with independent residuals have negative bias that increases with the sample size, while those with graphical or saturated dependence have small positive bias that is impervious to the sample size. Again, the magnitude of the bias is similar across all stepwise procedures, confirming no loss of information in using these.

## S.4 Additional graph selection example

In Section 4.2 of the main text we replicate the simulation study of Engelke and Hitz (2020, Section 5.5) to assess how well the SCMEVM identifies the graphical structure when data are generated from the Hüsler-Reiss distribution. Here we perform a similar simulation study but simulating data from the multivariate Gaussian distribution. Again taking  $d = 16$  and using the same graph  $\mathcal{G}$  as in Figure 3 (left panel) of the main text. We simulate 1000 points from a multivariate Gaussian distribution with the components of the mean vector  $\boldsymbol{\mu}$  independently sampled from a uniform distribution on  $(-5, 5)$  and correlation matrix consistent with  $\mathcal{G}$ . The data is transformed onto standard Laplace margins  $Y$  as per Section 3.1 of the main text. We use 100 replicates for this study.

To infer the optimal graphical structure using our model, we use Algorithm 3.5 of the main text. In the algorithm, we set the dependence threshold  $u_{Y_i}$  to the 0.90-quantile of the standard Laplace distribution. The final graph is obtained using a majority rule over the 11 inferred graphs when the graphical lasso penalty is  $\{0.2, 0.21, \dots, 0.30\}$ . Figure S7 (left panel) shows a weighted graph when  $\rho = 0.2$ , with line width and darkness proportional to the number of times the edge is selected across the 100 datasets. Some additional edges are suggested when  $\rho = 0.2$ , however, these are removed when we use a majority rule over the set described.

For comparison, we also use the graphical selection method proposed by Engelke and Hitz (2020, Section 5.3) to infer the graph. The only tuning parameter here is the threshold above which the data are assumed to follow a multivariate Pareto distribution. We set this to be the 0.90-quantile of the standard Pareto distribution. The weighted graph over the 100 datasets using this method is in Figure S7 (right panel). We see that the true graphical structure is identified. However, the algorithm never infers more than 17 edges in any of the 100 subgraphs, resulting in one of the edges not being identified when we prune the weighted graph using a majority rule. Results are somewhat threshold sensitive - using a lower threshold resulted in no change in the inferred structure but increasing the threshold resulted in more missing edges - suggesting that the Engelke and Hitz (2020) method can struggle to correctly identify the underlying structure of the data when the data-generating mechanism does not have complete AD, while the method proposed in the main text does not have this limitation.

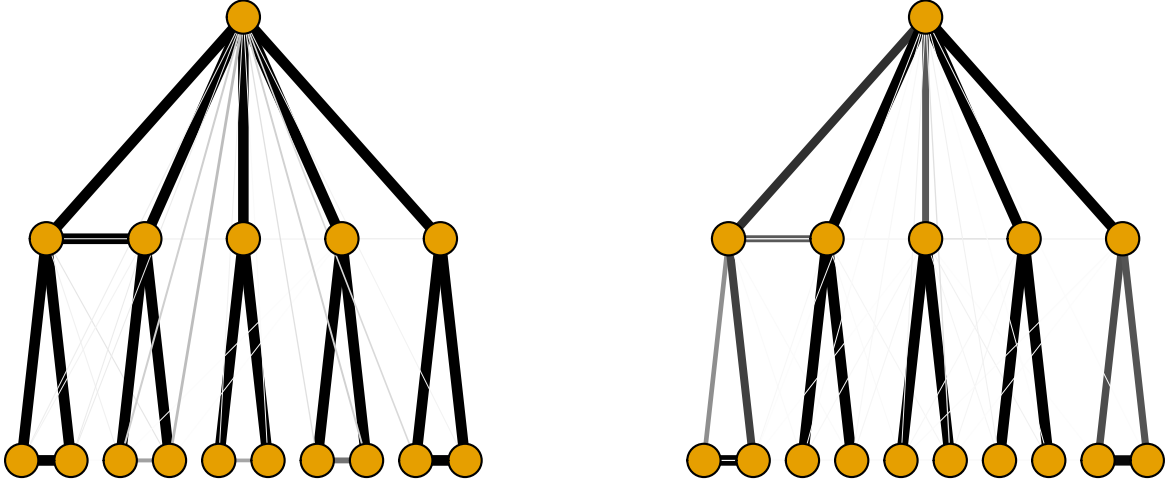


Figure S7: Inferred graphical structure using the method proposed in Section 3.2 of the main text (left) and using the method proposed by Engelke and Hitz (right). Line width and darkness indicate the number of times each edge was selected across 100 samples.

## S.5 Additional figures and simulation studies for Section 4.3

In the main text, we considered data with a mixture of extremal dependence structures. We now repeat the simulation study in Section 4.3 of the main text for data that exhibits either full asymptotic independence (AI) or full asymptotic dependence (AD). For AI, we simulate from each of the (a) multivariate Gaussian (MVG), (b) symmetric multivariate Laplace (MVL), and (c) multivariate  $t$ - (MVT) distributions. In all cases, both positive and negative associations are investigated. For AD, we simulate from a multivariate Pareto (MVP) distribution. All simulation studies follow a similar pattern. For each true distribution, 200 datasets are sampled using a dependence structure consistent with  $\mathcal{G}$  in Section S.3. Data are transformed from their canonical margins (e.g., Gaussian for the MVG distribution) to standard Laplace margins as per Section 3.1 of the main text. For all data sets, each of the one-, two- and three-step procedures is used to fit the SCMEVM with graphical covariance, where the graph is assumed to be known and correctly specified. The three-step procedure is also used to fit the SCMEVM with independent and saturated covariances. For comparison, we also fit the original CMEVM (Heffernan and Tawn, 2004) and the graphical extremes model (Engelke and Hitz, 2020) (EHM). The mean absolute error (MAE) and root mean squared error (RMSE) of the model-based estimates form the basis of model comparison. For simulations that have positive associations, we use tail probabilities  $\mathbb{P}[X_A > u_{X_A} \mid X_i > u_{X_i}]$  (for all

sets  $A \subseteq V_i$  and  $i \in V$ ) for model comparison, while for those that have negative associations we use probabilities of the form  $\mathbb{P}[X_A < u_{X_A} \mid X_i > u_{X_i}]$  for model comparison.

### S.5.1 Multivariate Gaussian distribution

In this section, we assume  $X$  follows a MVG distribution with mean vector  $\boldsymbol{\mu}$ , where each  $\mu_j$  is independently sampled from a uniform distribution on  $(-5, 5)$ , and correlation matrix  $\Sigma$ . Various strengths of correlation are considered however  $\Gamma = \Sigma^{-1}$  is always consistent with  $\mathcal{G}$  in Section S.3. We set dependence thresholds  $u_{Y_i}$  to the 0.90-quantile of the standard Laplace distribution. For prediction, we set  $u_{X_i}$  to the 0.95-quantile for the true distribution of  $X_i$  for each  $i \in V$ .

#### S.5.1.1 Weak positive dependence

In the first study, correlations between all components lie in  $(0, 0.47)$ . Figure S8 shows MLEs of the dependence and AGG parameters. Here, and in the other studies in this section, estimates from the three-step SCMEVM with graphical and saturated covariance structures are omitted as they are identical to results for the three-step SCMEVM with independent residuals. Also note that the MLEs for CMEVM dependence parameters are the same for the two- and three-step methods. The MLEs of  $\boldsymbol{\alpha}_{|i}$  ( $\boldsymbol{\nu}_{|i}$ ) from the one-step procedure are consistently lower (higher) than the MLEs from the stepwise approaches, confirming that the one-step method does not guarantee that the first-order extremal dependence structure will be captured by the dependence parameters. At best, by attributing some extremal dependence structure to the residual distribution, the interpretability of the SCMEVMs fitted with the one-step procedure is reduced. Potentially, it also makes the models less reliable. In contrast, the MLEs of  $\boldsymbol{\beta}_{|i}$ ,  $\boldsymbol{\kappa}_{1|i}$ ,  $\boldsymbol{\kappa}_{2|i}$ , and  $\boldsymbol{\delta}_{|i}$  are similar across all the models and fitting procedures. Finally, the right-scale parameter  $\kappa_{2|j_i}$  is almost always estimated to be larger than the left-scale parameter  $\kappa_{1|j_i}$ , supporting the choice of an asymmetric marginal distribution for  $Z_{|i}$ .

Figure S9 shows empirical and model-based estimates of the conditional precision matrix  $\Gamma_{|i}$ . Empirical estimates are the inverse of the conditional correlation matrix for  $Y \mid Y_i = y_i$ , such that  $y_i > u_{Y_i}$ , equivalently the inverse correlation matrix of  $Y \mid Y_i > u_{Y_i}$  excluding the  $i$ th row and column. Similar to the study in the main text, the estimated matrices are the same for the graphical and saturated SCMEVMs confirming there is negligible loss in using the former. Further the estimated structure of the conditional precision matrices for the graphical and saturated SCMEVMs is consistent with the empirical version. While it is plausible that the results here are specific to the MVG generating mechanism, similar patterns are observed for

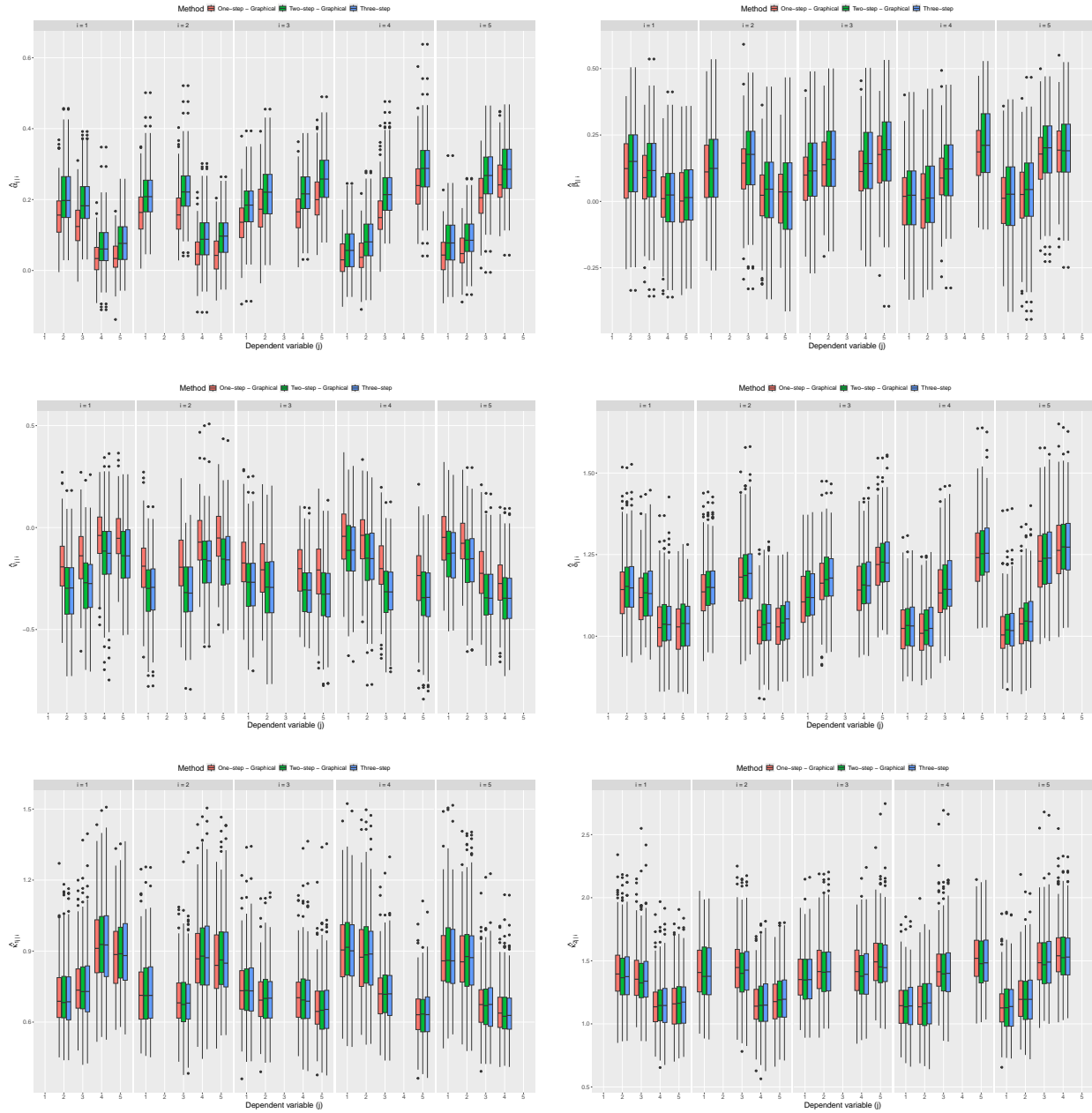


Figure S8: Boxplots of MLEs for  $\alpha_{j|i}$  (top left),  $\beta_{j|i}$  (top right),  $\nu_{j|i}$  (centre left),  $\delta_{j|i}$  (centre right),  $\kappa_{1_j|i}$  (bottom left), and  $\kappa_{2_j|i}$  (bottom right) for distinct  $i, j \in V$ . Each row corresponds to the conditioning variable  $i$ . The different models are denoted by the fill of the boxplots.

the other multivariate distributions.

We now compare predictions from the EHM and three-step SCMEVM with graphical covariance. Figure S10 (left panel) shows the bias in the conditional survival curves of  $X_j | X_1 > u_{X_1}$  for each  $j \in V_1$ . The SCMEVM is unbiased for all curves whereas the EHM has positive bias for lower values of  $u_{X_j}$ ; this decreases as  $u_{X_j}$  increases. The positive bias of



Figure S9: Boxplots of empirical and model-based estimates of  $\Gamma_{i|}$ , for each  $i \in V$ , when the data is generated from a MVG distribution with weak positive associations. Each row corresponds to the conditioning variable  $i$  and each column corresponds to the correlation parameter. The different models are denoted by the colour of the boxplots. Black dashed lines show  $y = 0$ .

the EHM persists in bivariate conditional survival probabilities. Figure S10 (right panel) shows the bias in  $\mathbb{P}[X_2 > u_{X_2}, X_3 > u_{X_3} \mid X_1 > u_{X_1}]$ . The three-step SCMEVM with independent residuals exhibits negative bias because  $X_2$  is not conditionally independent of  $X_3$  given  $X_1$ . In contrast, the SCMEVMs with graphical and saturated covariances are unbiased. The CMEVM predictions are also unbiased, probably due to the low dimension  $d$ . Lastly, the SCMEVMs with graphical covariance exhibit the least amount of bias and variability, minimising the MAE and RMSE for 87% and 77% of the 75 conditional probabilities, respectively. This confirms that there is no loss in performance when using a graphical structure over the more flexible saturated one and that the fully parametric SCMEVM outperforms the semi-parametric CMEVM. The EHM performs badly in this case because the true data have AI.

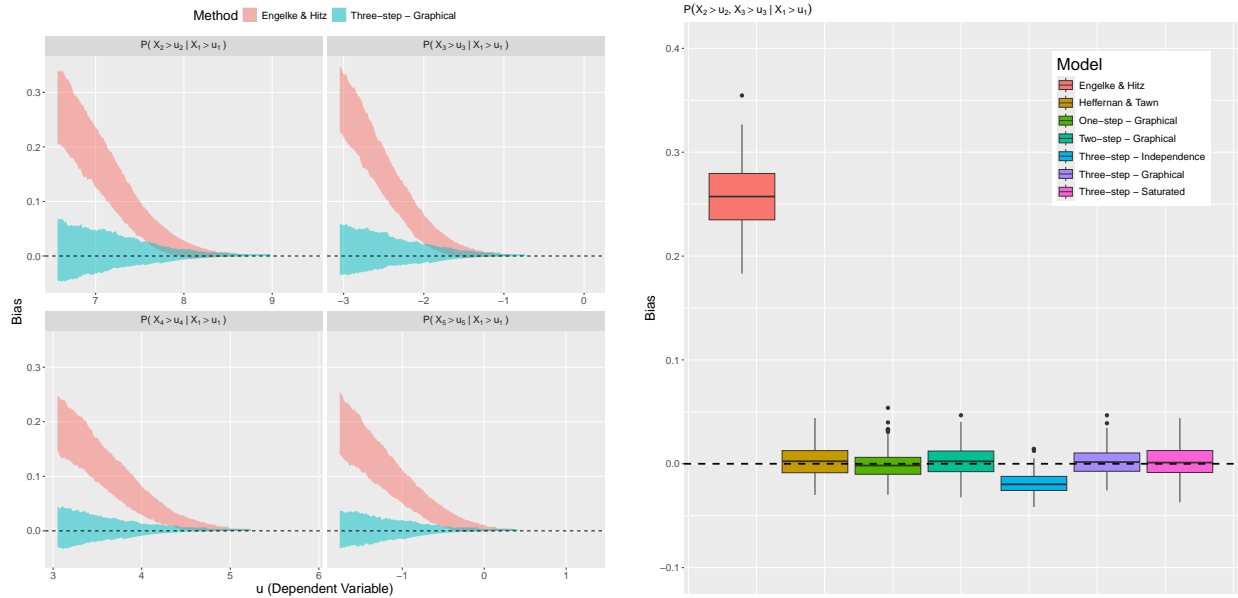


Figure S10: Polygon plots detailing 95% confidence intervals, over 200 samples, of the bias in  $\mathbb{P}[X_j > u_{X_j} | X_1 > u_{X_1}]$ , for each  $j \in V_{|1}$ , where  $X$  follows a MVG distribution with weak positive associations (left). The bias from the EHM and the three-step SCMEVM assuming a graphical covariance structure for the residuals are in pink and blue, respectively. Boxplots of the bias in  $\mathbb{P}[X_2 > u_{X_2}, X_3 > u_{X_3} | X_1 > u_{X_1}]$  (right). The bias from the various models is denoted by the fill of the boxplots. Black dashed lines show  $y = 0$ .

### S.5.1.2 Strong positive dependence

We repeat the simulation study in Section S.5.1.1 but the associations between the components of  $X$  are strong and positive ( $> 0.52$ ). We present only the predictive performances, as the parameter estimates show similar patterns to those seen in Section S.5.1.1. Figure S11 (left panel) shows bias in the conditional survivor curves for  $X_j | X_5 > u_{X_5}$  for both the EHM and the three-step SCMEVM with a graphical covariance structure, for  $j \in V_{|5}$ . Again, the EHM is biased for low values of  $u_{X_j}$  but this diminishes as  $u_{X_j}$  increases; the three-step SCMEVM with graphical structure is unbiased for all  $u_{X_j}$ . Figure S11 (right panel) shows the bias in  $\mathbb{P}[X_{|5} > u_{X_{|5}} | X_5 > u_{X_5}]$ . The EHM has positive bias whereas both the CMEVM and the SCMEVMs with graphical or saturated covariance structures are unbiased. The three-step SCMEVM with independent residuals has negative bias; this is expected since the components of  $X_{|5}$  are not independent given  $X_5$  is large. Assessing overall predictive performance, the SCMEVMs with graphical covariance structure are again the least biased and variable, minimising the MAE and RMSE metrics 81% and 84% of the time, respectively.

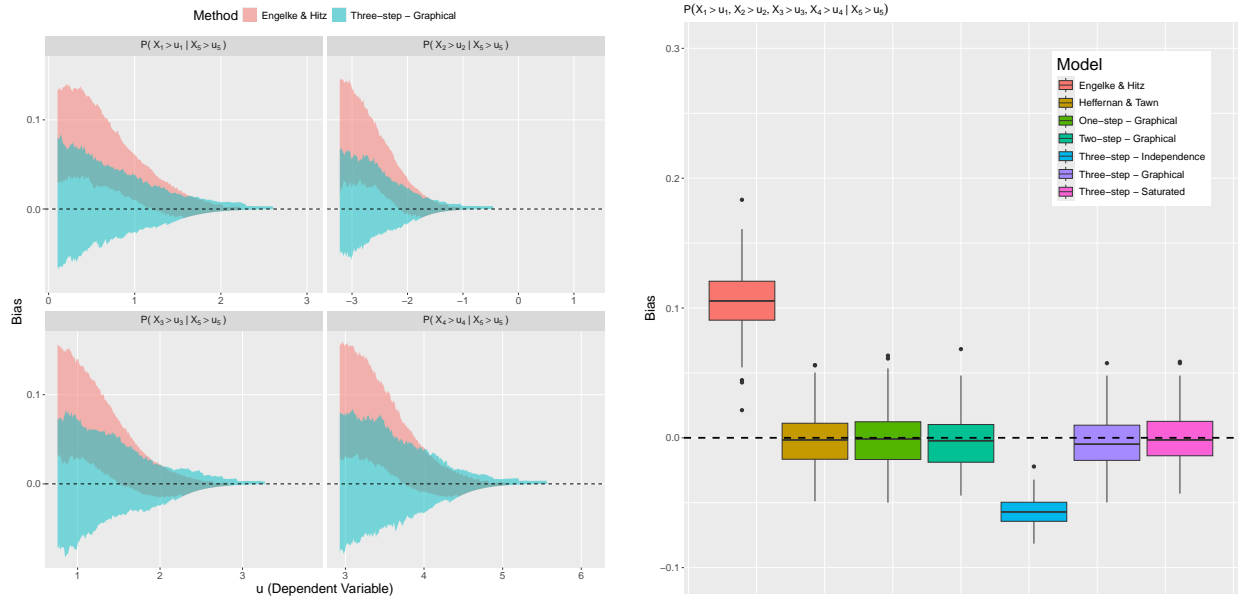


Figure S11: Polygon plots detailing 95% confidence intervals, over 200 samples, of the bias in  $\mathbb{P}[X_j > u_{X_j} \mid X_5 > u_{X_5}]$ , for  $j \in V_{|5}$  where  $X$  follows a MVG distribution with strong positive associations (left). The bias from the EHM and the three-step SCMEVM with a graphical covariance structure are in pink and blue, respectively. Boxplots of the bias in  $\mathbb{P}[X_{|5} > u_{X_{|5}} \mid X_5 > u_{X_5}]$  (right). The bias from the various models is denoted by the fill of the boxplots. Black dashed lines show  $y = 0$ .

### S.5.1.3 Negative dependence

We repeat the simulation study in Section S.5.1.1 but the association between the components of  $X$  are now allowed to be negative. The correlation matrix  $\Sigma$  is given in equation (S.1).

$$\Sigma = \begin{bmatrix} 1.000 & -0.468 & -0.370 & -0.136 & 0.134 \\ -0.468 & 1.000 & 0.390 & 0.144 & -0.141 \\ -0.370 & 0.390 & 1.000 & 0.369 & -0.362 \\ -0.136 & 0.144 & 0.369 & 1.000 & -0.346 \\ 0.134 & -0.141 & -0.362 & -0.346 & 1.000 \end{bmatrix} \quad (\text{S.1})$$

Figure S12 compares the MLEs of  $\kappa_{1_{j|i}}$  and  $\kappa_{2_{j|i}}$  from the three-step SCMEVM with a graphical covariance structure, for distinct  $i, j \in V$ . In the other MVG examples, the right-scale parameter is generally larger than the left-scale parameter whereas here a range of behaviour is observed. This further justifies the need for a flexible, asymmetric residual distribution.

Figure S13 (left panel) shows the bias in the conditional cumulative distribution curves for  $X_j \mid X_5 > u_{X_5}$  for the EHM and the three-step SCMEVM with graphical covariance

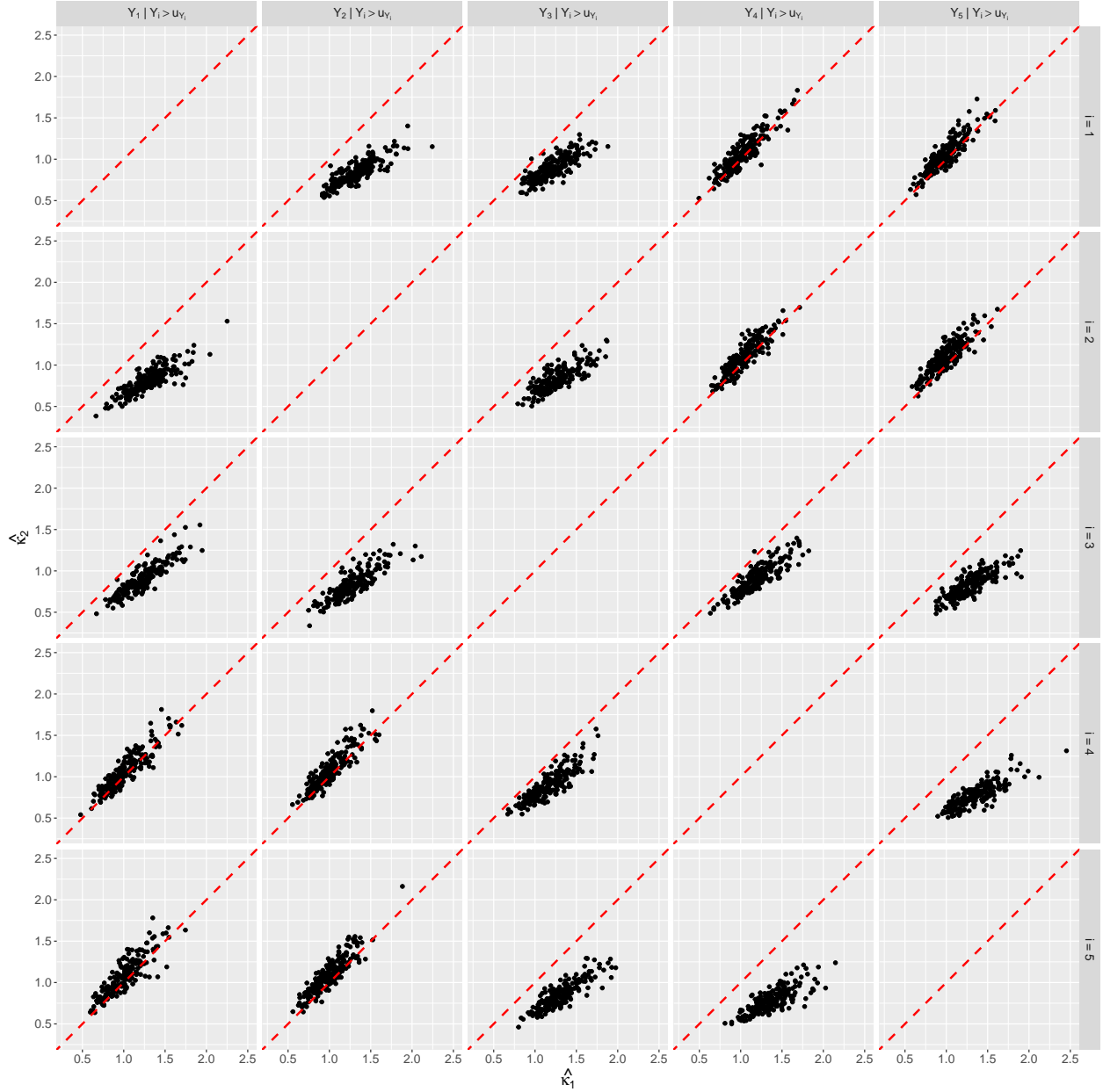


Figure S12: Scatter plots comparing  $\hat{\kappa}_{1|j|i}$  and  $\hat{\kappa}_{2|j|i}$  from the three-step SCMEVM with graphical covariance structure for distinct  $i, j \in V$ . Red dashed lines show  $y = x$ .

structure. The three-step SCMEVM shows no bias but the EHM underestimates the curve over the entire range. Again, this is not surprising, as the assumption of AD is not satisfied by the data. Figure S13 (right panel) considers the bias in  $\mathbb{P}[X_{|5} < u_{X_{|5}} | X_5 > u_{X_5}]$ . The EHM exhibits negative bias, while the CMEVM and SCMEVMs are unbiased. Finally, as in the previous studies, the SCMEVMs with graphical covariance structures are the least biased and variable, minimising the MAE and RMSE 76% and 87% of the time, respectively.

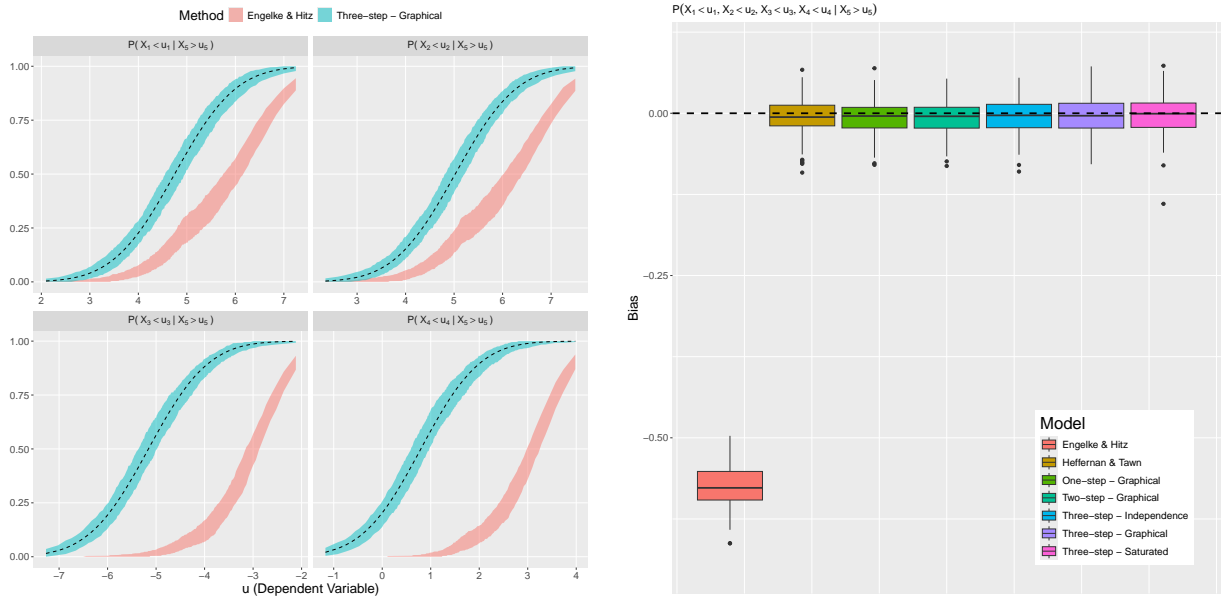


Figure S13: Polygon plots detailing 95% confidence intervals, over 200 samples, of  $\mathbb{P}[X_j < u_{X_j} \mid X_5 > u_{X_5}]$  for  $j \in V_{|5}$ , when  $X$  follows a MVG distribution with negative associations (left). The estimated curves from the EHM and the three-step SCMEVM with a graphical covariance structure are in pink and blue, respectively. The true conditional cumulative distribution curves are indicated by the black dashed lines. Boxplots of the bias in  $\mathbb{P}[X_{|5} < u_{X_{|5}} \mid X_5 > u_{X_5}]$  (right). The bias from the various models is denoted by the fill of the boxplots. The  $y = 0$  line is indicated by the black dashed line.

## S.5.2 Multivariate Laplace distribution

In this study,  $X$  follows a MVL distribution with mean vector  $\boldsymbol{\mu}$ , where  $\mu_j$  are independently sampled from a uniform distribution on  $(-5, 5)$ , and precision matrix consistent with  $\mathcal{G}$  in Section S.3.

### S.5.2.1 Weak positive dependence

In this simulation, associations between components are weakly positive i.e., the elements of the true correlation matrix are strictly positive but less than 0.37. We set the dependence threshold  $u_{Y_i}$  to be the 0.95-quantile of the standard Laplace distribution, resulting in approximately 250 excesses per conditioning variable. For prediction,  $u_{X_i}$  is set to the 0.95-quantile from a single sample of  $10^6$  from the true distribution. Figure S14 shows empirical and model-based estimates of the conditional precision matrix  $\Gamma_{|i}$ . The estimated structure of the conditional precision matrix from both the graphical and the saturated SCMEVM is consistent with the empirical version. Analysis of other parameter estimates have been omitted, but they are very similar across all three stepwise procedures. The only point to



Figure S14: Boxplots of empirical and model-based estimates of  $\Gamma_{|i}$ , for each  $i \in V$ , when the data is generated from a MVL distribution with weak positive associations. Each row corresponds to the conditioning variable  $i$  and each column corresponds to the correlation parameter. The different models are distinguished by the colour of the boxplots. Black dashed lines show  $y = 0$ .

note is that estimates for the left- and right-scale parameters in the MVAGG are very similar, raising the question of whether the generalised Gaussian would be a better choice of marginal residual distribution. However, other examples do have very different scale parameters (see Figures S8 and S12) and the more flexible asymmetric generalised Gaussian distribution is therefore recommended.

To compare predictive performance, Figure S15 (left panel) shows the bias in the conditional survival curves of  $X_j \mid X_3 > u_{X_3}$  for  $j \in V_3$ . Similar to the MVG examples, the SCMEVM with graphical covariance structure is unbiased for all curves, whereas the EHM has positive bias for low values of  $u_{X_j}$  which decreases as  $u_{X_j}$  increases. Figure S15 (right panel) shows the bias in  $\mathbb{P}[X_{|3} > u_{|3} \mid X_3 > u_{X_3}]$ . The CMEVM and the SCMEVMs with graphical or saturated covariance structures are unbiased, whereas, the EHM has positive bias. Again, the three-step SCMEVM with independent residuals has negative bias because not all components of  $X_{|3}$  are independent given  $X_3$ . Similar findings are made when assessing other

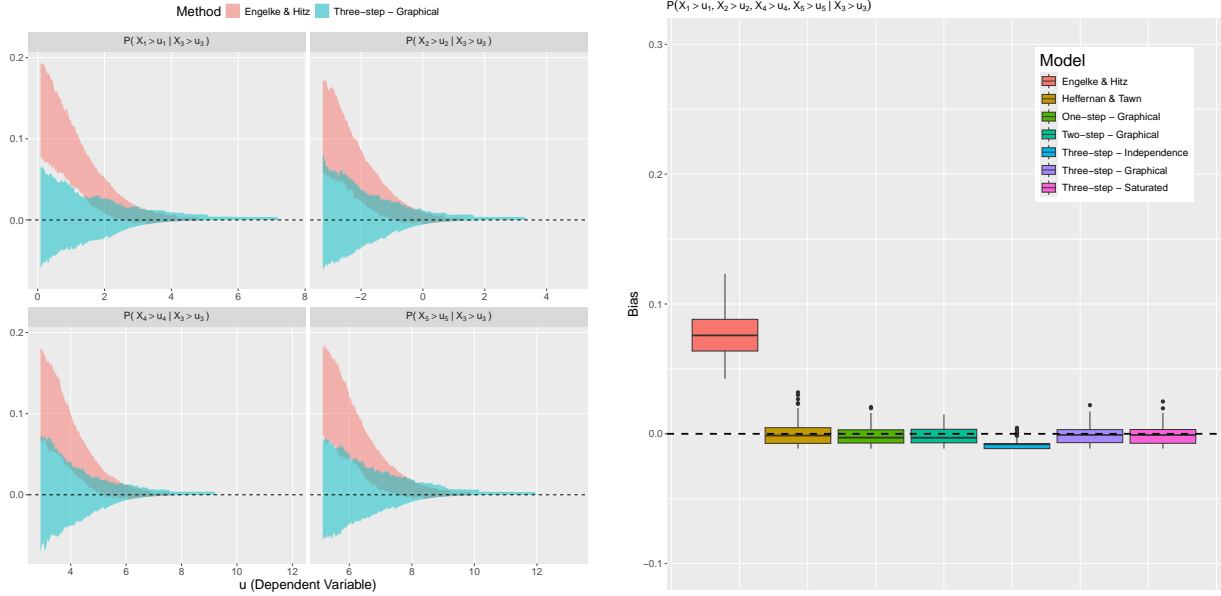


Figure S15: Polygon plots detailing 95% confidence intervals, over 200 samples, of the bias in  $\mathbb{P}[X_j > u_{X_j} \mid X_3 > u_{X_3}]$  for  $j \in V_{|1}$ , where  $X$  follows a MVL distribution with weak positive associations (left). The bias from the EHM and the three-step SCMEVM assuming a graphical covariance structure for the residuals are in pink and blue, respectively. Boxplots of the bias in  $\mathbb{P}[X_{|3} > u_{X_{|3}} \mid X_3 > u_{X_3}]$  (right). The bias from the various models is denoted by the fill of the boxplots. Black dashed lines show  $y = 0$ .

conditional probabilities of the form  $\mathbb{P}[X_A > u_A \mid X_i > u_i]$  for all  $A \subseteq V_i$  and  $i \in V$ . Lastly, the SCMEVMs with graphical covariance have the least amount of bias and variability, minimising the MAE and RMSE for 86% and 77% of the 75 conditional probabilities, respectively.

### S.5.2.2 Strong positive dependence

We repeat the simulation study in Section S.5.2.1 with strong positive association between the components i.e., the entries of the true correlation matrix are all greater than 0.69. The dependence threshold  $u_{Y_i}$  is set to the 0.9-quantile for the standard Laplace distribution, for each  $i \in V$ . For prediction, we set  $u_{X_i}$  to the 0.95-quantile from a dataset of size  $10^6$  simulated from the true distribution. We omit parameter estimates since the only point to note is that a comparison of the estimates from the one-, two-, and three-step SCMEVMs shows that the dependence parameters are slightly larger for the one-step method, while the location and scale parameters are slightly lower.

Figure S16 shows the bias in two tail probabilities,  $p_1 = \mathbb{P}[X_2 > u_{X_2}, X_3 > u_{X_3} \mid X_1 > u_{X_1}]$  and  $p_2 = \mathbb{P}[X_{|1} > u_{X_{|1}} \mid X_1 > u_{X_1}]$ . In this case the EHM performs more similarly to

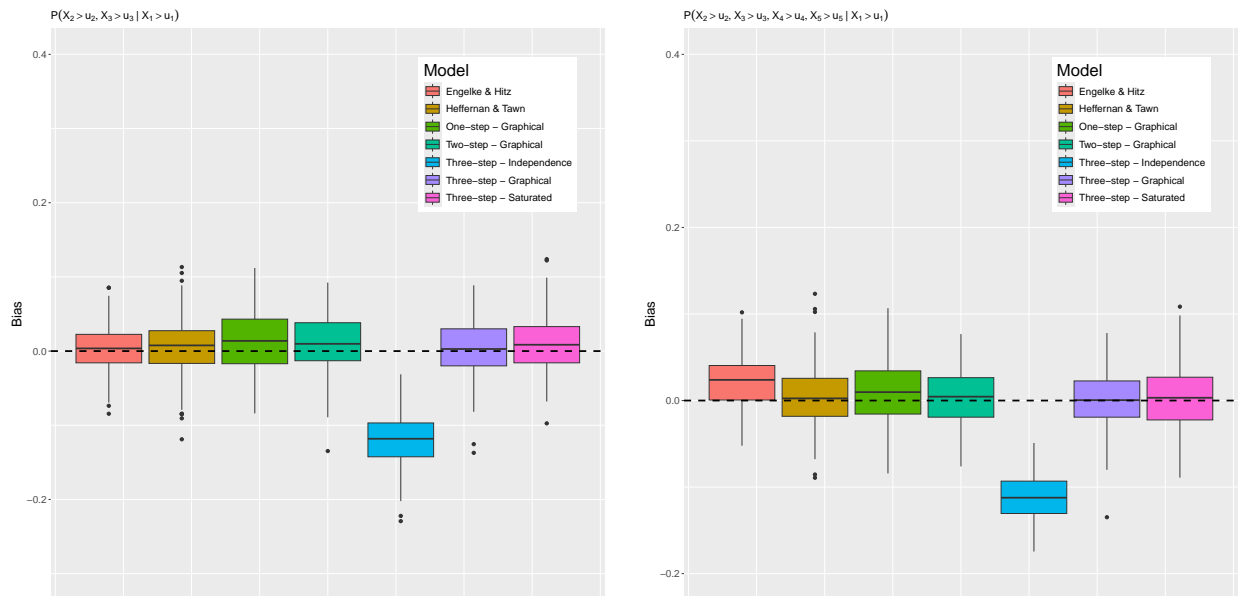


Figure S16: Boxplots of the bias in  $p_1 = \mathbb{P}[X_2 > u_{X_2}, X_3 > u_{X_3} \mid X_1 > u_{X_1}]$  (left) and  $p_2 = \mathbb{P}[X_{|1} > u_{X_{|1}} \mid X_1 > u_{X_1}]$  (right) when  $X$  follows a MVL distribution with strong positive associations. The bias from the various models is denoted by the fill of the boxplots. Black dashed lines show  $y = 0$ .

the CMEVM and SCMEVMs. However, while it is unbiased for  $p_1$ , it does have small positive bias for  $p_2$ . Further, the EHM minimises the MAE and RMSE for 37 and 42, respectively, of the 75 conditional probabilities, while the three-step SCMEVM with graphical covariance structure minimises the MAE and RMSE 31 and 25 times, respectively. The CMEVM and SCMEVMs with graphical or saturated covariance structures are unbiased for both probabilities in Figure S16 though suggesting these models scale better with dimension compared to the EHM.

### S.5.2.3 Negative dependence

Finally, we consider negative associations between components. The true correlation matrix is provided in equation (S.2). The dependence threshold  $u_{Y_i}$  is set to the 0.8-quantile for the standard Laplace distribution. For prediction, we set  $u_{X_i}$  to the 0.9-quantile from a dataset

of size  $10^6$  simulated from the true distribution.

$$\Sigma = \begin{bmatrix} 1.000 & -0.200 & -0.139 & 0.026 & 0.022 \\ -0.200 & 1.000 & -0.243 & 0.045 & 0.038 \\ -0.139 & -0.243 & 1.000 & -0.185 & -0.158 \\ 0.026 & 0.045 & -0.185 & 1.000 & -0.276 \\ 0.022 & 0.038 & -0.158 & -0.276 & 1.000 \end{bmatrix} \quad (\text{S.2})$$

The only point to note on the parameter estimates is that  $\beta_{j|i}$  tends to always be slightly higher for the one-step SCMEVM than for the two- and three-step SCMEVMs. Figure S17 (left panel) shows 95% confidence intervals for the conditional cumulative distribution curves of  $X_j \mid X_4 > u_{X_4}$  for  $j \in V_4$  and for the EHM and the three-step SCMEVM with graphical covariance structure. As with the MVG distribution with negative association, the SCMEVM captures the curves perfectly while the EHM underestimates all curves. The SCMEVMs with graphical covariance structure minimise the MAE and RMSE 63% and 59% of the time, respectively. The three-step SCMEVM with saturated covariance structure also performs very well minimising the metrics 23% and 28% of the time, respectively. However, the numerical values of the metrics are almost indistinguishable for the two models as shown in Figure S17 (right panel) where we plot the bias in  $\mathbb{P}[X_{j_4} < u_{X_{j_4}} \mid X_4 > u_{X_4}]$ . The EHM and SCMEVM with independent residuals are both biased, while the SCMEVMs with graphical or saturated covariance structure are unbiased. The CMEVM predictions exhibit a small positive bias, although the reason for this is unclear.

### S.5.3 Multivariate $t$ -distribution

For this study,  $X$  has a MVT distribution with mean  $\boldsymbol{\mu} = \mathbf{0}$ ,  $k = 5$  degrees of freedom, and a dispersion matrix with inverse consistent with  $\mathcal{G}$  in Section S.3.1. We consider weak positive, strong positive, and negative associations in  $X$  in Sections S.5.3.1, S.5.3.2, and S.5.1.3, respectively. For all simulations, the dependence threshold  $u_{Y_i}$  is set to the 0.8-quantile from the standard Laplace distribution, resulting in approximately 1,000 excesses per conditioning variable. As with the previous examples, parameter estimates are omitted unless of specific interest.

#### S.5.3.1 Weak positive dependence

In this simulation, we ensure the associations between components are weakly positive i.e., entries in the dispersion matrix are strictly positive but less than 0.17. For prediction, we set  $u_{X_i} = 0.75$  for each  $i \in V$ .

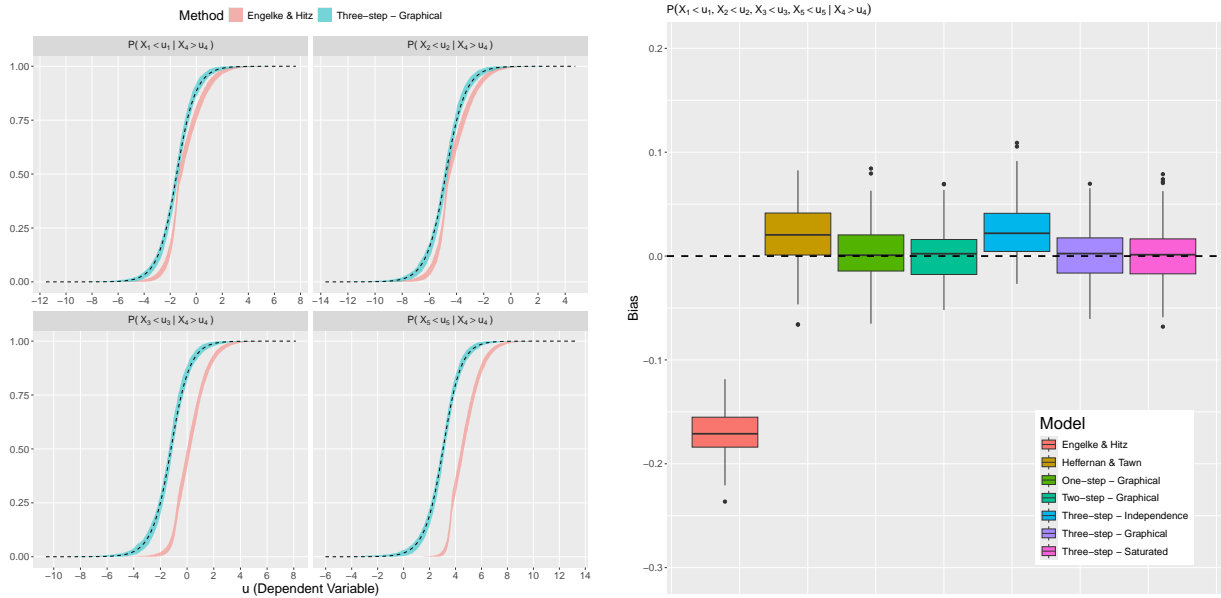


Figure S17: Polygon plots detailing 95% confidence intervals, over 200 samples, of the bias in  $\mathbb{P}[X_j < u_{X_j} | X_4 > u_{X_4}]$  for  $j \in V_4$ , where  $X$  follows a MVL distribution with negative associations (left). The bias from the EHM and the three-step SCMEVM assuming a graphical covariance structure for the residuals are in pink and blue, respectively. The true conditional cumulative distribution curves are given by the black dashed lines. Boxplots of the bias in  $\mathbb{P}[X_{|4} < u_{X_{|4}} | X_4 > u_{X_4}]$  (right). The bias from the various models is denoted by the fill of the boxplots. The  $y = 0$  line is given by the black dashed line.

Figure S18 shows empirical and model-based estimates of the conditional precision matrix  $\Gamma_{|i}$ . The estimated structure of the conditional precision matrix from both the graphical and saturated SCMEVMs is again consistent with the empirical version. Analysis of other parameter estimates has been omitted, other than noting that estimates of  $\beta_{j|i}$  from the one-step SCMVEM are generally larger than corresponding estimates from the two- and three-step SCMEVMs.

Figure S19 (left panel) shows the bias in the conditional survival curves of  $X_j | X_3 > u_{X_3}$  for  $j \in V_3$ . Similar to the MVG and MVL examples, the SCMVEM with graphical covariance structure is unbiased for all curves, whereas, the EHM exhibits positive bias for low values of  $u_{X_j}$  which decreases as  $u_{X_j}$  increases. We have also included the estimated curve from the CMEVM to show there is little difference between the estimates from the CMEVM and the SCMEVM with graphical covariance structure.

Figure S19 (right panel) shows the bias in  $\mathbb{P}[X_{|3} > u_{|3} | X_3 > u_{X_3}]$ . As expected, the CMEVM estimates are unbiased, the EHM exhibits positive bias, and the three-step SCMEVM with independent residuals exhibits negative bias because not all the components of  $X_{|3}$  are in-



Figure S18: Boxplots of empirical and model-based estimates of  $\Gamma_{|i}$ , for each  $i \in V$ , when the data is generated from a MVT distribution with weak positive associations. Each row corresponds to the conditioning variable  $i$  and each column corresponds to the correlation parameter. The colour of the boxplots distinguishes the different models. Black dashed lines show  $y = 0$ .

dependent given  $X_3$ . Interestingly, the fully parametric SCMEVMs with graphical or saturated covariance structures exhibit a very small negative bias. Despite this, the three-step SCMEVM with graphical structure is the least biased and variable model as it minimises the MAE and RMSE for 38 and 46, respectively, of the 75 conditional tail probabilities across all models. In comparison, the CMEVM only minimises the metrics 21 and 13 times, respectively. This suggests there is little difference between the CMEVM and the SCMEVM in this scenario.

Assessing diagnostic plots from the SCMEVM creates no concern with the model fit. Therefore, to fix the slight underestimation from the SCMEVMs in Figure S19 (right panel), we may need to increase  $N'$  used in Algorithm 3.5 of the main text (we let  $N' = 250,000$  in this simulation). Alternatively, we may wish to simulate data from the fitted model for  $X \mid X_i > u_{X_i}$  for each  $i \in V$ , rather than for the more general simulation from Section 3.3 in the main text which simulates data for the entire domain with the extreme region

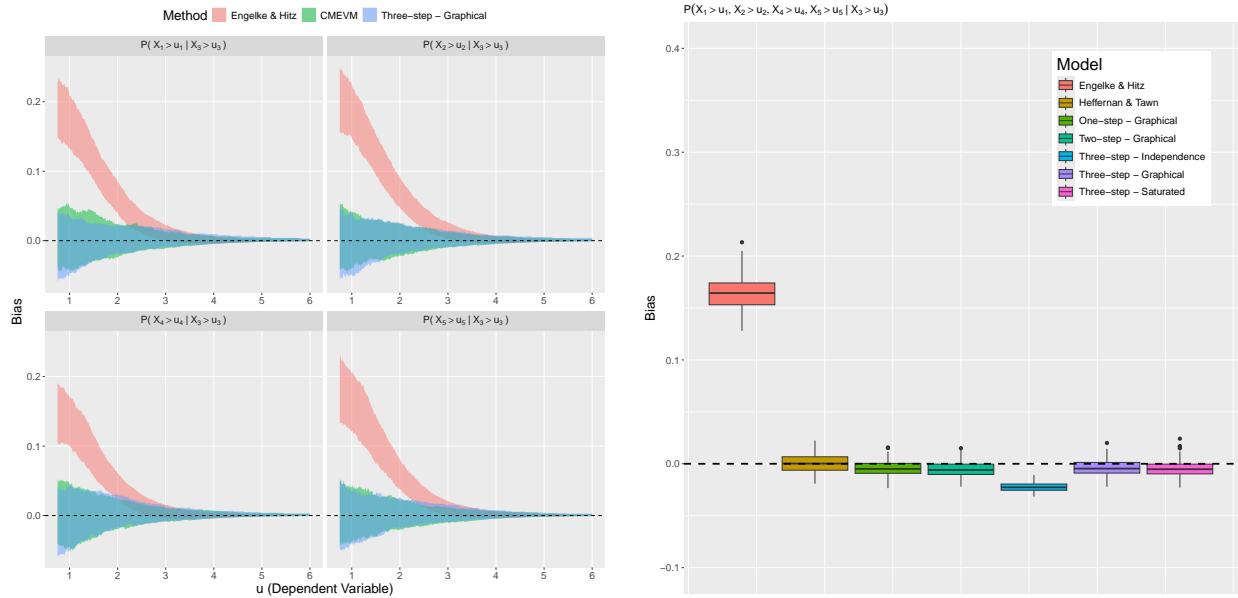


Figure S19: Polygon plots detailing 95% confidence intervals, over 200 samples, of the bias in  $\mathbb{P}[X_j > u_{X_j} | X_3 > u_{X_3}]$ , for each  $j \in V_{|1}$ , where  $X$  follows a MVT distribution with weak positive associations (left). The bias from the EHM, the CMEVM, and the three-step SCMEVM assuming a graphical covariance structure for the residuals are in pink, green, and blue, respectively. Boxplots of the bias in  $\mathbb{P}[X_{|3} > u_{X_{|3}} | X_3 > u_{X_3}]$  (right). The fill of the boxplots distinguishes the different models. Black dashed lines show  $y = 0$ .

corresponding to at least one component is extreme.

### S.5.3.2 Strong positive dependence

We now allow strong positive associations between the components. The only note on the parameter estimates is that the CMEVM dependence parameters, tend to be higher for the one-step SCMEVM compared to the two- and three-stepwise SCMEVMs, while the marginal AGG parameters (excluding the shape) tend to be lower for the one-step SCMEVM. Setting  $u_{X_i} = 1.25$  for each  $i \in V$ , Figure S20 (left panel) shows the bias in the conditional survivor curves of  $X_j | X_2 > u_{X_2}$  for  $j \in V_{|2}$ , and for the EHM and the three-step SCMEVM with graphical covariance structure. The EHM is biased for low values of  $u_{X_j}$  but this diminishes as  $u_{X_j}$  increases. In contrast, the three-step SCMEVM with a graphical covariance structure is unbiased across all curves. Figure S20 (right panel) shows the bias in  $\mathbb{P}[X_{|3} > u_{X_{|3}} | X_3 > u_{X_3}]$ . The EHM has positive bias, while the CMEVM and the stepwise SCMEVMs with graphical or saturated covariance structures are unbiased. Once again, the SCMEVMs with graphical covariance structure are the least biased and the least variable, minimising both the MAE and RMSE for 48 of the 75 conditional tail probabilities.

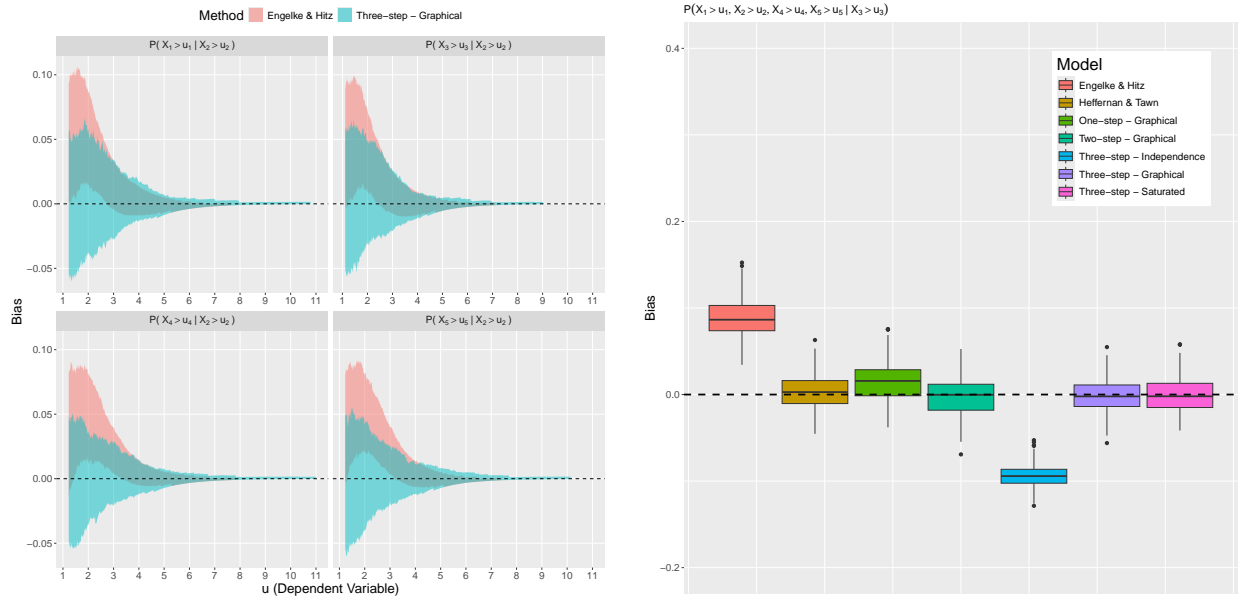


Figure S20: Polygon plots detailing 95% confidence intervals, over 200 samples, of the bias in  $\mathbb{P}[X_j > u_{X_j} \mid X_2 > u_{X_2}]$  for  $j \in V_2$ , where  $X$  follows a MVT distribution with strong positive associations (left). The bias from the EHM and the three-step SCMEVM assuming a graphical covariance structure for the residuals are in pink and blue, respectively. Boxplots of the bias in  $\mathbb{P}[X_3 > u_{X_3} \mid X_3 > u_{X_3}]$  (right). The bias from the various models is denoted by the fill of the boxplots. Black dashed lines show  $y = 0$ .

### S.5.3.3 Negative dependence

Finally, we allow for weak negative associations between the components. For prediction, we set  $u_{X_i}$  to the 0.9-quantile from a dataset of size  $10^6$  simulated from the true distribution. Figure S21 (left panel) shows 95% confidence intervals for the conditional cumulative distribution curves of  $X_j \mid X_3 > u_{X_3}$  for  $j \in V_3$  and for the EHM and the three-step SCMEVM with graphical covariance structure. As with the MVG and MVL distributions with negative associations, the three-step SCMEVM captures all curves perfectly, whereas the EHM always underestimates. Figure S21 (right panel) shows the bias in  $\mathbb{P}[X_{|5} < u_{X_{|5}} \mid X_5 > u_{X_5}]$ . The EHM performs poorly due to its inability to capture the negative dependence, while predictions from the CMEVM and the SCMEVMs with graphical or saturated covariance structures are unbiased. The SCMEVMs with a graphical covariance structure minimise the MAE and RMSE metrics for 79% and 72%, respectively, of conditional tail probabilities.

### S.5.4 Multivariate Pareto distribution

To test the SCMEVM under AD, we repeat the simulation study for  $X$  with a MVP distribution such that the parameter matrix is consistent with  $\mathcal{G}$  in Section S.3. For the CMEVM,

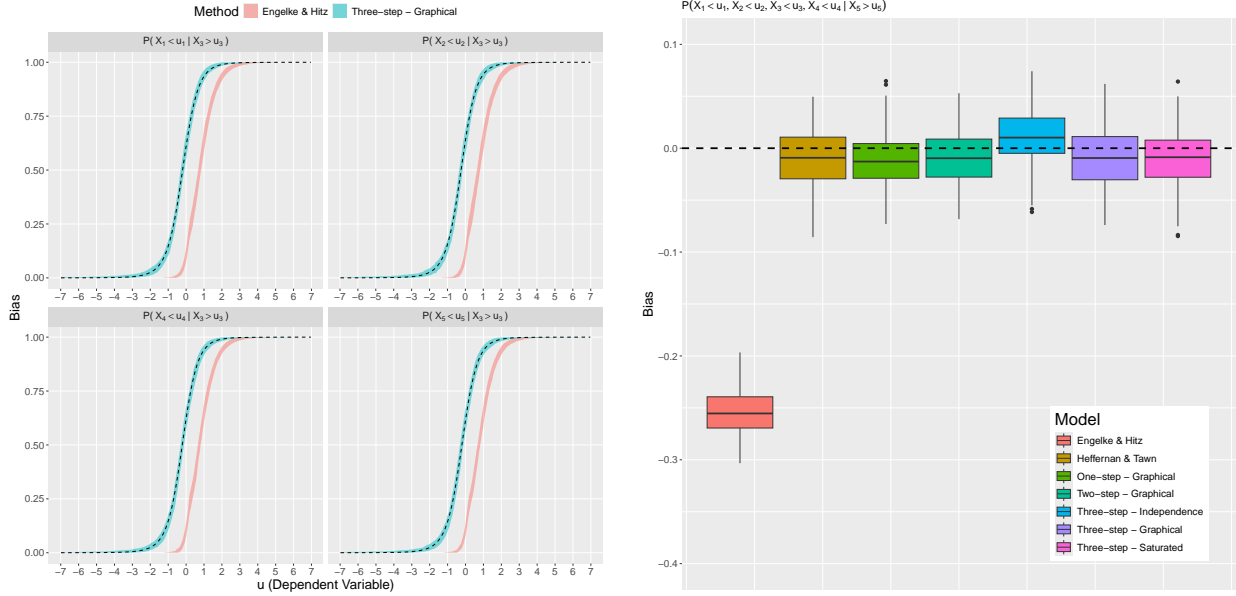


Figure S21: Polygon plots detailing 95% confidence intervals, over 200 samples, of the bias in  $\mathbb{P}[X_j < u_{X_j} \mid X_3 > u_{X_3}]$  for  $j \in V_3$ , where  $X$  follows a MVT distribution with negative associations (left). The bias from the EHM and the three-step SCMEVM assuming a graphical covariance structure for the residuals are in pink and blue, respectively. The true conditional cumulative distribution curves are given by the black dashed lines. Boxplots of the bias in  $\mathbb{P}[X_{|5} < u_{X_{|5}} \mid X_5 > u_{X_5}]$  (right). The bias from the various models is denoted by the fill of the boxplots. The  $y = 0$  line is given by the black dashed line.

we use only data above the dependence threshold  $u_{Y_i}$  set at the 0.90-quantile of the standard Laplace distribution. The EHM uses all data since, by construction, the data is on standard Pareto margins. For prediction,  $u_{X_i} = 11$  for each  $i \in V$ .

Figure S22 shows empirical and SCMEVM model-based estimates of  $\Gamma_{|i}$  and transformed model-based estimates from the EHM. Again, the empirical structure is retained in all models. The EHM and SCMEVMs have a very close correspondence, although the former has less variability due to the larger sample size. Figure S23 (left panel) shows the bias in the conditional survivor curves for  $X_j \mid X_5 > u_{X_5}$ ,  $j \in V_{|5}$ . Both the EHM and the three-step SCMEVM with graphical covariance are unbiased, but estimates from the former are slightly less variable due to the larger sample size. Figure S23 (right panel) shows the bias in  $\mathbb{P}[X_{|5} > u_{X_{|5}} \mid X_5 > u_{X_5}]$ . As expected, the EHM is unbiased while the SCMEVMs exhibit a slight negative bias perhaps due to the  $\alpha$  parameter not converging to the true value,  $\alpha = 1$ , that lies on the edge of the parameter space. However, the bias in the SCMEVMs with graphical and saturated covariances is small. Considering all 75 conditional tail probabilities, the EHM minimises both the MAE and RMSE metrics the majority of the time. Excluding the EHM, which is the only model specifically designed for AD data, the SCMEVMs with



Figure S22: Boxplots of empirical and model-based estimates of  $\Gamma_{|i}$ , for each  $i \in V$ , when the data is generated from a MVP distribution. Each row corresponds to the conditioning variable  $i$  and each column corresponds to the correlation parameter. The various models are denoted by the colour of the boxplots. Black dashed lines show  $y = 0$ .

graphical covariance minimise the metrics 83% and 89% of the time, respectively, suggesting that the SCMEVM is an acceptable alternative to the EHM when the extremal dependence class cannot be pre-determined.

## S.6 Additional figures for Section 5

We obtain 200 non-parametric bootstrap samples of the declustered river discharge data from the upper Daube River basin. For each bootstrapped dataset, we fit (i) the EHM, (ii) the three-step SCMEVM with graphical covariance structure, (iii) the three-step SCMEVM with saturated covariance structure, and (iv) the three-step SCMEVM with graphical covariance structure. The graph for (i) and (ii) is given by the undirected tree induced by the flow connections of the upper Danube River basin (Figure 1 (left panel) of the main text) while the graph for (iv) is inferred (Figure 6 (right panel) of the main text).

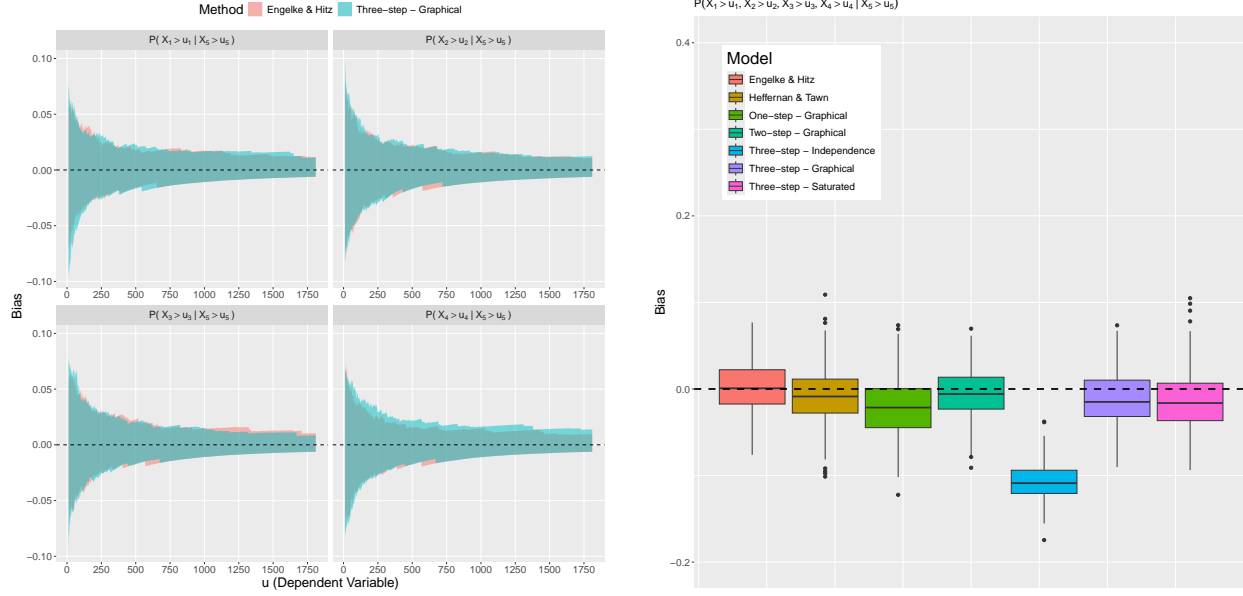


Figure S23: Polygon plots detailing 95% confidence intervals, over 200 samples, of the bias in  $\mathbb{P}[X_j > u_{X_j} | X_1 > u_{X_1}]$  for  $j \in V_{|1}$ , where  $X$  follows a MVP distribution (left). The bias from the EHM and the three-step SCMEVM assuming a graphical covariance structure for the residuals are in pink and blue, respectively. Boxplots of the bias in  $\mathbb{P}[X_{|5} > u_{X_{|5}} | X_5 > u_{X_5}]$  (right). The bias from the various models are denoted by the fill of the boxplots. Black dashed lines show  $y = 0$ .

For each of the fitted models and for each bootstrapped dataset, we obtain a single simulation which is used for prediction. Empirical and model-based estimated for  $\chi_{i,j}(u)$  are obtained for  $i, j \in V$ ,  $i > j$ , and  $u \in \{0.8, 0.85, 0.9\}$ , where  $V = \{1, \dots, 31\}$ . The point estimates in Figure S24 are the median estimates over the two sets of estimates for  $\chi_{i,j}(u)$ . As in Figure 7 of the main text, the SCMEVMs better capture the extremal dependence structure than the EHM. Figure S25 shows a similar comparison but for  $\chi_A(u)$  where  $A \subset V$  are 500 randomly sampled triplets, and  $u \in \{0.8, 0.85, 0.9\}$ . Again, the SCMEVMs better capture the extremal dependence in the upper Danube River basin. Although for higher thresholds the EHM is less biased for moderately dependent triplets, the bias for low dependent triplets increases as the threshold increases. Similar conclusions can be made for (iv), however, the magnitude of the bias is much smaller. Model (iv) appears to perform better than (ii) and rectifies the systemic underestimation in (iii). Thus, (iv) appears to have best predictive performance across multiple components.

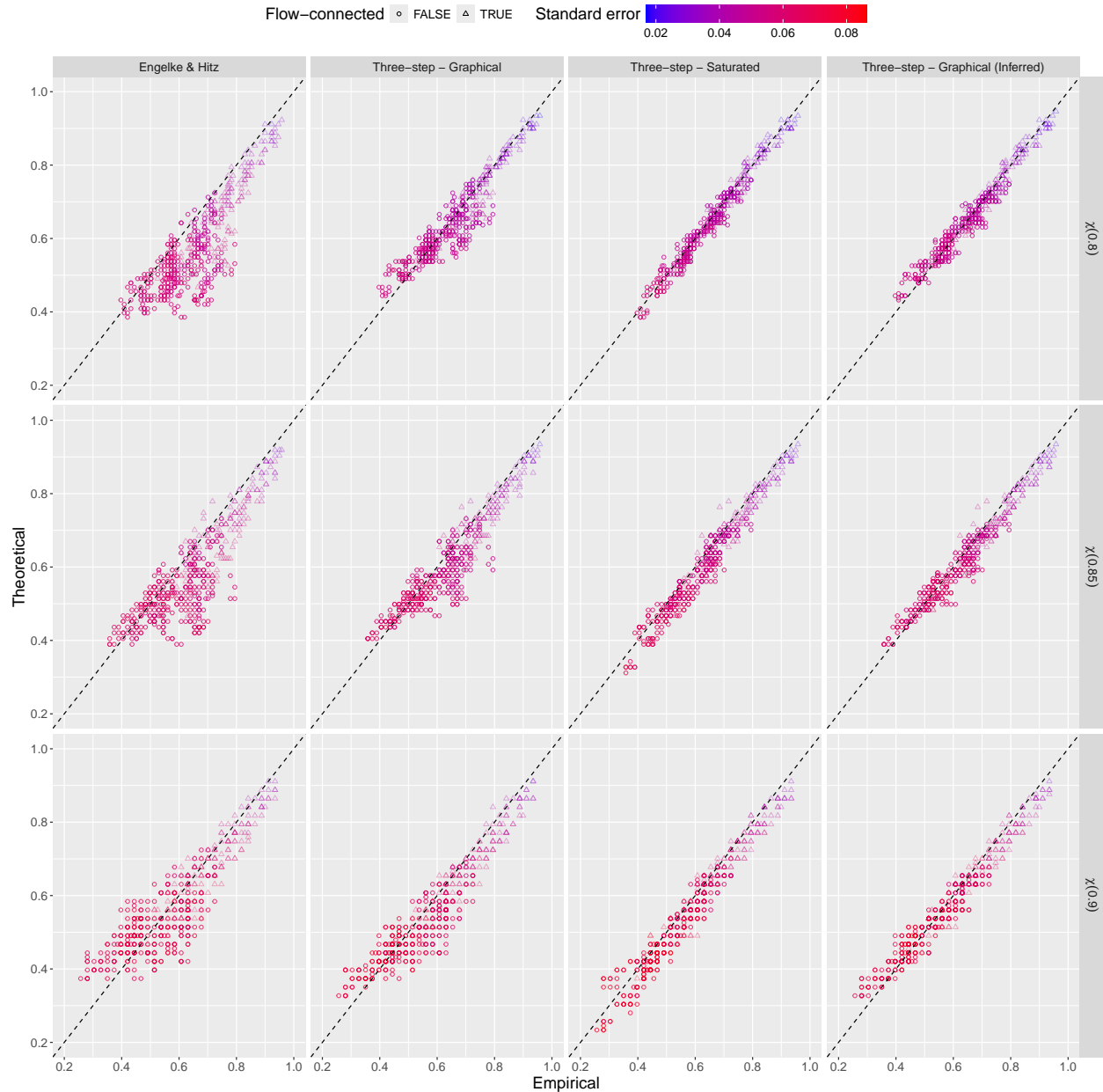


Figure S24: Empirical and model-based estimates of  $\chi_{i,j}(u)$  for  $u \in \{0.8, 0.85, 0.9\}$  (top to bottom), and  $i, j \in V$  but  $i > j$ . Model-based estimates use the EHM (left) and the three-step SCMEVM with graphical covariance (centre left), with structure given in Figure 1 (left panel) of the main text, the three-step SCMEVM with saturated covariance (centre right) and graphical covariance (right) with structure given in Figure 6 (right panel) of the main text. Black dashed lines show  $y = x$ . Circles (triangles) show flow-connected (flow-unconnected). The colour shows the standard error of the model-based estimates.

## Supplementary References

Engelke, S. and Hitz, A. S. (2020). Graphical models for extremes. *Journal of the Royal Statistical Society: Series B (Statistical Methodology)*, 82(4):871–932.

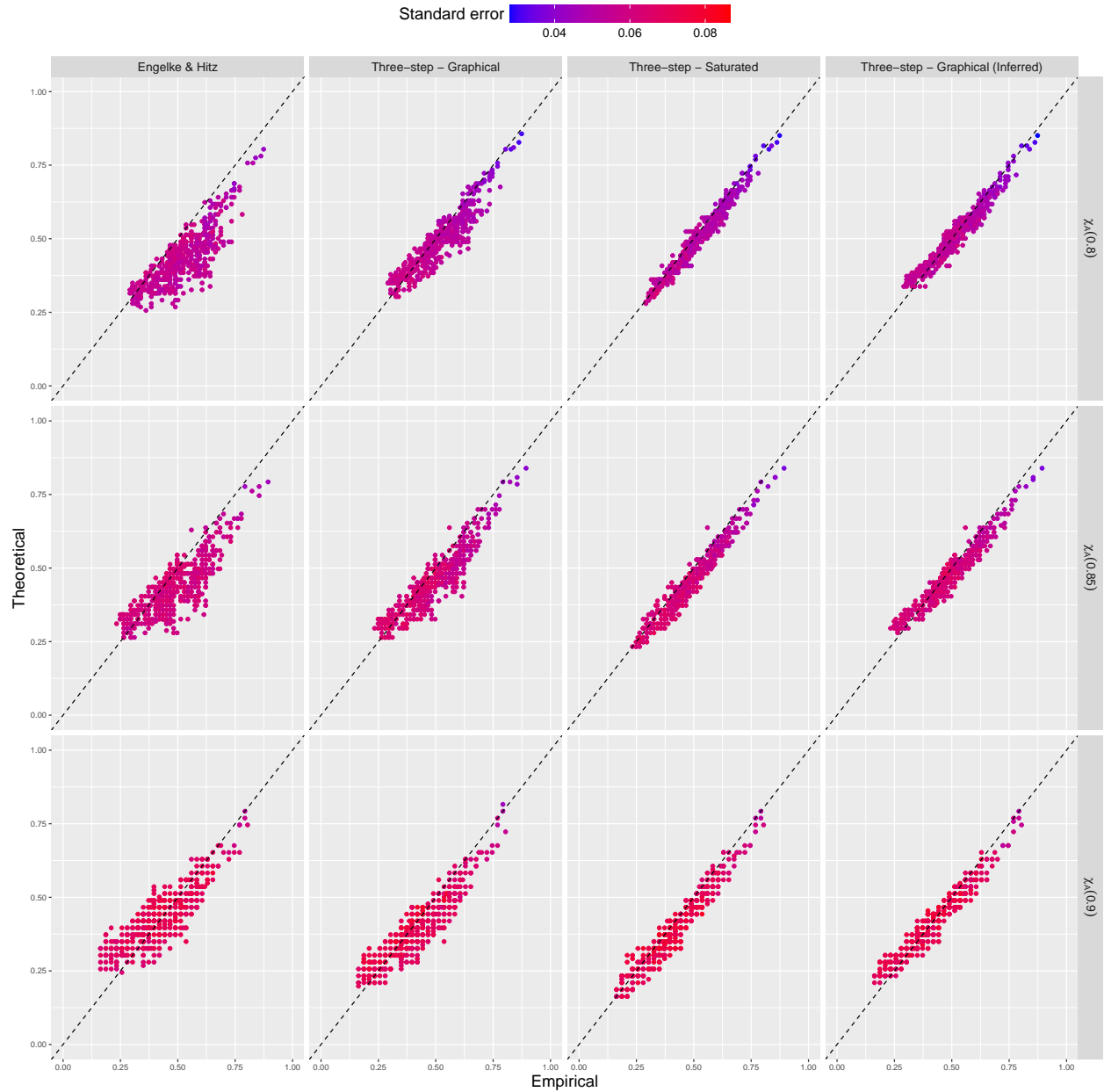


Figure S25: Empirical and model-based estimates of  $\chi_A(u)$  for  $u \in \{0.8, 0.85, 0.9\}$  (top to bottom) for 500 randomly selected triplets of  $A \subset V$ . Model-based estimates use the EHM (left) and the three-step SCMEVM with graphical covariance (centre left), with structure given in Figure 1 (left panel) of the main text, the three-step SCMEVM with saturated covariance (centre right) and graphical covariance (right) with structure given in Figure 6 (right panel) of the main text. Black dashed lines show  $y = x$ . The colour shows the standard error of the model-based estimates.

Heffernan, J. E. and Tawn, J. A. (2004). A conditional approach for multivariate extreme values (with discussion). *Journal of the Royal Statistical Society: Series B (Statistical Methodology)*, 66(3):497–546.

- Nagler, T. and Czado, C. (2016). Evading the curse of dimensionality in nonparametric density estimation with simplified vine copulas. *Journal of Multivariate Analysis*, 151:69–89.
- Wadsworth, J. and Tawn, J. (2022). Higher-dimensional spatial extremes via single-site conditioning. *Spatial Statistics*, 51:100677.